Universität der Bundeswehr München

Fakultät für Luft- und Raumfahrttechnik

Institut für Werkstoffkunde

Metallic metamaterials with tunable coefficient of thermal expansion fabricated via bi-material laser-based powder bed fusion

Isabel Beatriz Prestes

Vollständiger Abdruck der von der Fakultät für Luft- und Raumfahrttechnik der Universität der Bundeswehr München zur Erlangung des akademischen Grades eines

Doktors der Naturwissenschaften (Dr. rer. nat.)

angenommenen Dissertation.

Gutachter:

1. Univ.- Prof. Dr. rer. nat. Eric A. Jägle

2. Prof. Dr. Iain Todd

Diese Dissertation wurde am 16.12.2025 bei der Universität der Bundeswehr München eingereicht und durch die Fakultät für Luft- und Raumfahrttechnik am 09.06.2026 angenommen. Tag der mündlichen Prüfung war der 24.06.2026.

Acknowledgements

I would like to express my deepest gratitude to my supervisor, Prof. Eric Aimé Jägle, for his unwavering support, trust, guidance, and experience. Thank you for always being available to discuss the scientific outcomes of the experiments, for contributing your insights, and for puzzling through the debugging of the temperamental equipment I had to work with. Thank you for continuously advocating for me and helping me reach where I stand today – from the turbulent move to Germany during the pandemic, to creating responses to paper reviewers. A PhD is not only about science, and you were also there to listen and advise me during difficult moments. Thank you.

I would like to thank Prof. Iain Todd, for his willingness to act as a reviewer and enthusiasm for the topic of this thesis. I extend my thanks to the head of the examination committee, Prof. Roger Förstner.

This work was carried out at the Institute of Materials Science, where I was fortunate to receive both scientific and emotional support from my colleagues. My sincere thanks go to all members of the group – current and former – who worked alongside me throughout this period. Thank you for the scientific input, the insightful ideas that helped me better understand my results, and for helping me understand, assemble, disassemble, observe, and debug the machines and equipment that were used in this work. I am also grateful for the lighter moments, for your understanding during stressful times, and for the occasional *Feierabendbier*.

A special thank-you goes to Lucy Farquhar, my friend and Aerosint-colleague, for reading and improving this thesis, and helping me trust myself. Even though you joined the group during the final stages of my PhD, life in both laboratory and the office became much lighter and more enjoyable with you around.

I would like to thank the technical staff separately for their invaluable assistance with sample preparation, for finding solutions for part construction, for the countless pieces that needed to be cut from build platforms, and for the many other services provided during this PhD – along with the fun conversations.

My gratitude extends to the SeRANIS project, funded by dtec.bw, for funding my PhD, the equipment, and the consumables. I also thank the partners of the satellite experiment, for the scientific discussions.

I thank the FLAB project, also funded by dtec.bw, for funding essential equipment for this research, as well as its members – professors and PhD students – who contributed ideas, offered help, and provided equipment for specific analyses.

A special thank-you goes to Institute of Mechanics, for making equipment available, for offering a room for our measurement devices while the laboratory was closed, for facilitating liquid nitrogen supply for cryogenic dilatometry, and for the enjoyable moments shared along the way.

I would also like to thank the co-authors of the papers included in this thesis. A special thank you to Johannes Rottler for encouraging me to improve my knowledge in FEM simulations and for dedicating valuable time to help interpret the results. Thank you as well for the great partnership – both at work-related events and outside of work.

My thanks go to Schaeffler Aerosint and Linseis for consistently providing fast and high-quality support for the multi-material recoater and the dilatometer, respectively. A special acknowledgment to Ulrich Hinterreiter, who always assisted with understanding recoater circuit maps and promptly provided excellent electrical services.

I am grateful to the students I supervised during this period; through their work, they contributed to the understanding of phenomena essential to this thesis. I also thank them for helping me grow as a mentor.

From the bottom of my heart, I thank my husband, Victor – my partner through everything – for his affection, his emotional support during difficult times, for listening to countless presentation rehearsals, for embracing this adventure with me, for growing alongside me, and for never letting me give up.

To my loving parents and sister: thank you for your unconditional love and support, for always believing in me, and for being present despite the physical distance. Facing this period far from you was truly challenging. Your visits here, and my trips back to Brazil, always gave me renewed strength to continue.

Finally, to my friends, scattered across this wide world: thank you for filling my life with joy and laughter.

“Quit, don’t quit…

Noodles, don’t noodles…”

Master Oogway

Abstract

Additive Manufacturing (AM) enables the fabrication of complex geometries that are difficult or impossible to accomplish using conventional manufacturing techniques. The emergence of Multi-material AM (MMAM) further extends these capabilities by integrating different materials within the same part. This opens up the opportunities for the design of mechanical metamaterials with tunable thermal expansion, which is of critical importance in high-precision applications, such as space systems and optical benches.

The coefficient of thermal expansion (CTE) of these metamaterials can be tuned by combining two different materials within a specific lattice structure. In this thesis, the design, simulation, fabrication, and characterization of tunable CTE metamaterials, composed of Invar and Inconel 718, produced via bi-metallic laser-based powder bed fusion (PBF-LB) were investigated. The work was carried out within the framework of the SeRANIS project, which seeks to enable adaptive thermally stable structures for next-generation satellite systems.

Firstly, a study was conducted to determine an optimal laser scanning strategy to be applied on vertical interfaces between the two materials. The quality of the interfaces was analyzed for the presence of defects and material intermixing, characterized by energy dispersive X-ray spectroscopy (EDS). Using optimized scanning strategies, metamaterials with tunable CTE based on triangular-shaped unit cells were printed. The samples included unit cells with different geometric parameters, matrices of combined unit cells and an actuator intended for a satellite experiment. The samples' CTE were measured either by dilatometry or digital image correlation (DIC) and these values were compared with the finite element method (FEM) simulations used to predict the metamaterials' CTE. Lastly, the structural integrity of the printed metamaterials was analyzed through tensile testing and thermal cycling to evaluate suitability for space applications.

This thesis demonstrated the successful fabrication of Invar-Inconel 718 metamaterials with predictable and adjustable CTE. The optimized single scan strategy led to defect-free, metallurgically sound interfaces, showing that, in MMAM, process optimization must consider not only suitable parameters for each individual material, but also ideal scanning strategies at their interfaces. The triangular negative CTE metamaterials exhibited an experimentally measured CTE in close agreement with FEM simulations. The results indicated that metamaterial CTE can be tuned through geometric design, with the hinge stiffness identified as a key parameter, and material assignment within the lattice structure. By mitigating bulging effects, larger unit cell arrays provided a more representative metamaterial behavior than isolated unit cells. The integration of additional geometries for the satellite actuator did not significantly alter the thermal response. By combining positive and negative CTE unit cells, an overall CTE could be varied over a large range of values. Tensile tests confirmed that fracture occurred consistently in the weaker material (Invar), validating the interface strength. Thermally cycled samples did not fail or exhibit plastic deformation.

Overall, this thesis establishes a design and manufacturing framework for tunable CTE metamaterials, reliable for space applications, with predictable thermal expansion behavior. Future possible directions for material selection, distribution, and geometric optimization were identified to further enhance the performance of these metamaterials.

Kurzfassung

Additive Fertigung (Additive Manufacturing, AM) ermöglicht die Herstellung komplexer Geometrien, die mit konventionellen Fertigungsmethoden schwer oder gar nicht realisierbar sind. Multi-Material-Additiven Fertigung (MMAM) erweitert das Einsatzspektrum, indem unterschiedliche Werkstoffe innerhalb eines einzigen Bauteils simultan verwendet werden können. Dies eröffnet neue Möglichkeiten für die Entwicklung mechanischer Metamaterialien mit einstellbarer thermischer Ausdehnung, die für hochpräzise Anwendungen wie Raumfahrtsysteme und optische Bänke von entscheidender Bedeutung ist.

Der Wärmeausdehnungskoeffizient (Coefficient of Thermal Expansion, CTE) dieser Metamaterialien kann durch die Kombination zweier verschiedener Materialien innerhalb einer spezifischen Gitterstruktur eingestellt werden. In dieser Arbeit wurden das Design, die Simulation, die Fertigung und die Charakterisierung von Metamaterialien mit einstellbarem CTE untersucht. Die zu untersuchenden Proben wurden aus Invar und Inconel 718 mittels bi-metallischem laserbasiertem Pulverbettverfahren (PBF-LB) hergestellt. Die Arbeiten wurden im Rahmen des SeRANIS-Projekts durchgeführt, das adaptive, thermisch stabile Strukturen für Satellitensysteme der nächsten Generation ermöglichen soll.

Zu Beginn der Arbeit wurde eine Parameteroptimierung durchgefürht, um eine hinreichend Adhesion der Materialien an den vertikalen Grenzflächen zu erreichen. Die Qualität der Grenzflächen wurde hinsichtlich des Vorhandenseins von Defekten und der Materialvermischung analysiert. Die Charakterisierung erfolgte mittels energiedispersiver Röntegenspektroskopie (EDS). Mit Hilfe des optimierten Parameters konnten dann Probekörper, bestehend aus trigonalen Elementarzellen, mit einstellbarem CTE hergestellt werden. Die Proben umfassten Elementarzellen mit unterschiedlichem geometrischem Parameter, Matrizen aus kombinierten Elementarzellen sowie einen Aktuator, der für ein Satellitenexperiment vorgesehen ist. Die CTE-Werte der Proben wurden entweder mittels Dilatometrie oder Digitaler Bildkorrelation (DIC) gemessen. Die ermittelten Werte wurden mit Werten aus Finite-Element Simulationen (FEM) zur Vorhersage des CTE von Metamaterialien verglichen. Abschließend wurde die strukturelle Integrität der gedruckten Metamaterialien mithilfe von Zugversuchen und thermischen Zyklen untersucht, um ihre Eignung für Raumfahrtanwendungen zu bewerten.

Diese Arbeit zeigt die erfolgreiche Herstellung von Invar–Inconel-718-Metamaterialien mit vorhersagbarem und einstellbarem CTE. Die optimierte Belichtungsstrategie führte zu fehlerfreien, metallurgisch hochwertigen Grenzflächen und verdeutlicht, dass bei MMAM die Prozessoptimierung nicht nur geeignete Parameter für jedes einzelne Material, sondern auch ideale Belichtungsstrategien an ihren Grenzflächen berücksichtigen muss. Die dreieckigen Metamaterialien mit negativem CTE zeigten experimentell gemessene CTE-Werte, die gut mit den FEM-Simulationen übereinstimmen. Die Ergebnisse zeigen, dass der CTE des Metamaterials durch geometrisches Design und die Materialverteilung innerhalb der Gitterstruktur einstellbar ist, wobei die Steifigkeit der Gelenke als Schlüsselparameter identifiziert wurde. Durch die Verringerung von Ausbeulungs-effekten lieferten größere Verbünde von Elementarzellen ein repräsentativeres Metamaterialverhalten als isolierte Zellen. Die Integration zusätzlicher Geometrien für den Satellitenaktuator veränderte die thermische Reaktion nicht signifikant. Durch die Kombination positiver und negativer CTE-Elementarzellen kann ein Gesamt-CTE über einen großen Wertebereich variiert werden. Mechanische Tests bestätigten, dass die Brüche im

schwächeren Material (Invar) auftraten, was die Festigkeit der Grenzflächen validiert. Thermisch zyklierte Proben versagten nicht und zeigten keine plastische Deformation.

Insgesamt etabliert diese Arbeit ein Design- und Fertigungsframework für Metamaterialien mit einstellbarem CTE, das für Raumfahrtanwendungen zuverlässig ist und ein vorhersagbares thermisches Ausdehnungsverhalten aufweist. Zukünftige Forschungsrichtungen hinsichtlich Materialauswahl und -verteilung sowie geometrischer Optimierung wurden identifiziert, um die Leistungsfähigkeit dieser Metamaterialien weiter zu verbessern.

Table of contents

List of acronyms ix
1. Introduction 1
2. Multi-material Additive Manufacturing 4
2.1. Additive Manufacturing 4
2.2. Metal Additive Manufacturing 5
2.2.1. Laser-based powder bed fusion 6
2.3. Metal Multi-material Additive Manufacturing 7
2.3.1. Current MMAM systems available for metal PBF-LB 8
2.3.2. Multi-material challenges 11
2.3.3. Known material combinations 13
3. Metamaterials with negative coefficient of thermal expansion 14
3.1. Manufacturing of metamaterials 18
3.2. Chronological development of tunable CTE metamaterials 19
3.3. Potential applications 23
3.4. Summary and present work 24
4. Materials and methods 26
4.1. CAD modelling of the metamaterials 26
4.2. Finite element method simulations 27
4.3. Sample manufacturing 28
4.3.1. Feedstock materials 29
4.4. Microscopy analyses 30
4.5. CTE measurements 30
4.6. Structural integrity tests 31
5. Results and publications 33
5.1. Publication {1}: The bi-material PBF-LB process 35
5.2. Publication {2}: The principle behind NTE metamaterials 36
5.3. Publication {3}: The application in a satellite experiment 37
6. Conclusions and future work 38
References 41
Publication {1} 50
Publication {2} 63
Publication {3} 76

List of acronyms

Acronym	Description
1D	One dimensional
2D	Two dimensional
3D	Three dimensional
AM	Additive Manufacturing
BJT	Binder Jetting
CAD	Computer-aided Design
CTE	Coefficient of thermal expansion
DED	Directed Energy Deposition
DIC	Digital Image Correlation
EDS	Energy Dispersive X-ray Spectroscopy
FDM	Fused Deposition Modelling
FEM	Finite Element Method
FGM	Functionally Graded Materials
IN718	Inconel 718
MEX	Material Extrusion
MJT	Material Jetting
MMAM	Multi-Material Additive Manufacturing
NTE	Negative thermal expansion
PBC	Periodic boundary conditions
PBF	Powder Bed Fusion
PBF-LB	Laser-based Powder Bed Fusion
PTE	Positive thermal expansion
SEM	Scanning Electron Microscope
SHL	Sheet Lamination
SL	Stereolithography
SPD	Selective Powder Deposition
TRL	Technology Readiness Level
VED	Volumetric energy density
VPP	Vat Photopolymerization
ZTE	Zero thermal expansion

1. Introduction

The emergence of the Additive Manufacturing (AM) technology has enabled the fabrication of complex geometries that are difficult or impossible to accomplish using conventional manufacturing techniques. This is primarily due to the geometric freedom that AM offers [1]. Numerous case studies have demonstrated the potential of AM to reduce weight and enhance performance through topology optimization and by minimizing assembly steps, through integrating multiple components into a single part [2–5]. Multi-material AM (MMAM) further expands the potential of this technology by enabling the integration of different materials within the same part. Initially, MMAM systems were limited to polymers, but, more recently, metal MMAM techniques have been developed allowing multiple metals to be printed together [6–8].

In many engineering applications, the combination of distinct material properties is required to achieve a target performance. For instance, some components may require high corrosion resistance, thermal or electrical conductivity in localized regions, while maintaining low density, biocompatibility, or high mechanical strength in others. Such differences in properties can often not be satisfied by use of the same material throughout. Examples of these ideal property combinations are demanded in the aerospace, energy, biomedical, automotive, construction, and tooling industries, where MMAM has great potential for the fabrication of heat exchangers, electrical devices, implants, combustion chambers, wear-resistant components, and cutting tools, for example. MMAM opens up the possibility of fabricating multi-functional components in a single process step, bypassing the constraints of conventional techniques that rely on post-processing assembly [6,7,9,10].

A promising application for MMAM is the fabrication of metamaterials, i.e., engineered structures with unconventional properties, such as negative Poisson's ratio or tunable coefficients of thermal expansion (CTE) [11,12]. While the former may benefit from but does not depend on the use of different materials [13,14], the latter requires that at least two materials are combined within their lattice structure [15,16].

Most natural materials exhibit a positive CTE, expanding when heated. However, by strategically combining materials with different CTEs within a specific lattice structure, it is possible to create structures with a highly positive, near-zero, or even negative CTE. One of the mechanisms behind tunable CTE metamaterials is schematically represented by the triangle in Figure 1. The base of the triangle is made of a material with a higher CTE than the sides of the triangle. As the temperature increases, the base of the triangle expands more than its sides, reducing the height of the triangle, thus leading to a negative CTE in the Y-direction. By reversing the material assignment in the triangle structure, a highly positive CTE is produced. Therefore, this structure allows a range of CTEs to be tuned in order to achieve a target CTE for a specific engineering application [15,17,18]. Near-zero CTEs are ideal for precision instruments that require high dimensional accuracy under temperature fluctuations. Negative CTE structures can be used to compensate for thermal expansion in surrounding materials with positive CTE, resulting in an overall zero-CTE system. Conversely, highly positive CTE designs can function as thermally activated actuators [19–21].

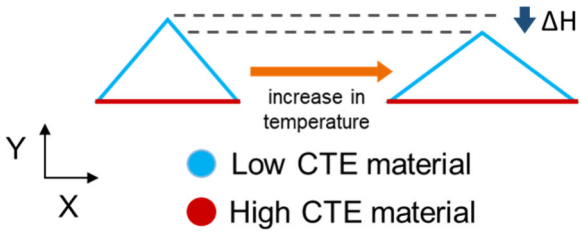


Figure 1 – Principle of metamaterials with negative CTE: two different materials are combined in a triangular lattice structure. The base of the triangle is made of a material with a higher CTE than the material that composes the sides of the triangle. When the temperature is increased, the base of the triangle expands more than its sides, reducing the height of the triangle, thus leading to a negative CTE in the Y-direction. By inverting the material assignment, highly positive CTEs are achieved, allowing a range of CTEs to be tuned for specific engineering applications.

This thesis primarily investigates tunable CTE metamaterials following the triangle mechanism illustrated in Figure 1. However, other design strategies proposed in the literature will also be addressed in Chapter 3. The metamaterials can be designed to have tunable CTEs in different directions, including isotropic properties, by combining these mechanisms into more complex shapes [22–24]. Regardless of the approach, achieving such behavior invariably requires at least two materials [15,16].

Early works on tunable CTE metamaterials were mostly focused on their simulation and mathematical modelling due to the limitations of conventional manufacturing [20,25–27]. Some structures were built as proof-of-concept using techniques like gluing, bolting, or laser spot welding [28–30]. However, MMAM truly unlocked the potential of fabricating these metamaterials, eliminating the need for assembly steps between the different materials, and enabling even micrometer-scale structures to be printed [23,24,31,32]. Initially, polymer MMAM was applied, but recent advances in metal MMAM, especially in laser-based powder bed fusion (PBF-LB) process, have enabled metamaterials with tunable CTE to be manufactured with metallic materials [33–35]. Since metallic systems offer higher thermal stability and stiffness compared to polymer-based counterparts, their use expands the application potential of these metamaterials.

Because commercially viable multi-metallic PBF-LB systems have only recently become available, research in this field regarding material combinations, process dynamics, and interface quality is still in its early stages [7,10,36]. Challenges associated with dissimilar metal printing, such as the formation of brittle intermetallic phases, can hinder or delay the practical implementation of multi-metallic structures and components [6–8]. Therefore, few studies have gone so far as to investigate the actual performance of these components in their intended application environments.

This PhD thesis investigates metamaterials composed of Invar and Inconel 718 fabricated via bi-metallic PBF-LB, designed to have tunable CTE. The research is part of the SeRANIS project[1], which aims to apply a negative CTE metamaterial in a satellite experiment to achieve thermal dimensional stability through passive or active CTE compensation. The thesis comprises three peer-reviewed publications, each addressing a specific research question critical to realizing this goal:

[1] Seamless Radio Access Network for Internet of Space (SeRANIS) is a satellite mission funded by dtec.bw and NextGenerationEU, in which several experiments will be mounted to test new technologies for space applications.

- **P{1} : What is the appropriate laser scanning strategy to achieve defect-free vertical interfaces between Invar and Inconel 718?**
  This study investigates various scanning strategies and their impact on the interface quality in bi-metallic PBF-LB specimens, evaluating material intermixing, porosity, and crack formation.
- **P{2} : How do geometric features influence the CTE of the metamaterials, and what are the premises to enable an accurate prediction of the thermal behavior of printed metamaterials?**
  This work explores triangular unit cells with varying geometries. Finite element simulations under two boundary conditions and two different unit cells types of the metamaterial were studied and compared, resulting in the reliable prediction of the negative thermal expansion behavior of the printed metamaterials.
- **P{3} : How suitable are the negative CTE metamaterials fabricated via bi-metallic PBF-LB for space applications, and what are possible future applications in this field?**
  This publication evaluates the mechanical integrity of printed bi-metallic structures through mechanical testing, alongside experimental measurement of both negative and positive CTE metamaterials—highlighting the tunable nature of the design and its potential for future applications.

The structure of the thesis includes two literature review chapters – Chapter 2 focused on MMAM and Chapter 3 on metamaterials with negative CTE – followed by a concise description of the materials and methods used in Chapter 4. Finally, Chapter 5 provides extended abstracts of the three core studies, leading to conclusions and directions for future research. The peer-reviewed publications are included thereafter.

2. Multi-material Additive Manufacturing

This chapter starts with a broad overview of single-material AM and metal AM, including the principles of PBF-LB. Later, the advance into multi-material AM (MMAM) processes are described, pointing out available metal MMAM techniques, potential applications, and challenges.

2.1. Additive Manufacturing

AM consists of constructing a three-dimensional part by the successive deposition of material layers, which are digitally generated from the part's computer-aided design (CAD) model [37]. The first AM systems to be developed in the 1980s encouraged the research and development of this technology due to the simplicity of the path between digital and physical models and potential advantages over conventional manufacturing, allowing part customization, material savings, and fabrication of complex geometries [38–41].

The first AM techniques to be commercially available and consolidated used polymers as feedstock, such as stereolithography (SL) and fused deposition modeling (FDM) [1,42]. Nowadays, a variety of materials can be manufactured via AM, including metals, polymers, ceramics, and composites, and in different feedstock forms, such as powder, wire, liquid, filament, and sheet [42,43]. During these decades of development, the application of parts produced via AM shifted from visualization tools and rapid prototyping to end-use products in the aerospace, automotive, medical, electronics, and tooling industries, meeting the requirements for mechanical properties and structural integrity. As new techniques and novel materials are being developed for AM, its range of potential applications is also constantly increasing [40,42,43].

Current AM processes are classified into seven different categories by the ISO/ASTM 52900 (2021) norm, based on their energy sources, material joining strategies and feedstock shape: Binder Jetting (BJT), Directed Energy Deposition (DED), Material Extrusion (MEX), Material Jetting (MJT), Powder Bed Fusion (PBF), Sheet Lamination (SHL), and Vat Photopolymerization (VPP) [4,37,41,44]. Short descriptions and schematic representations of these categories are presented in Figure 2.

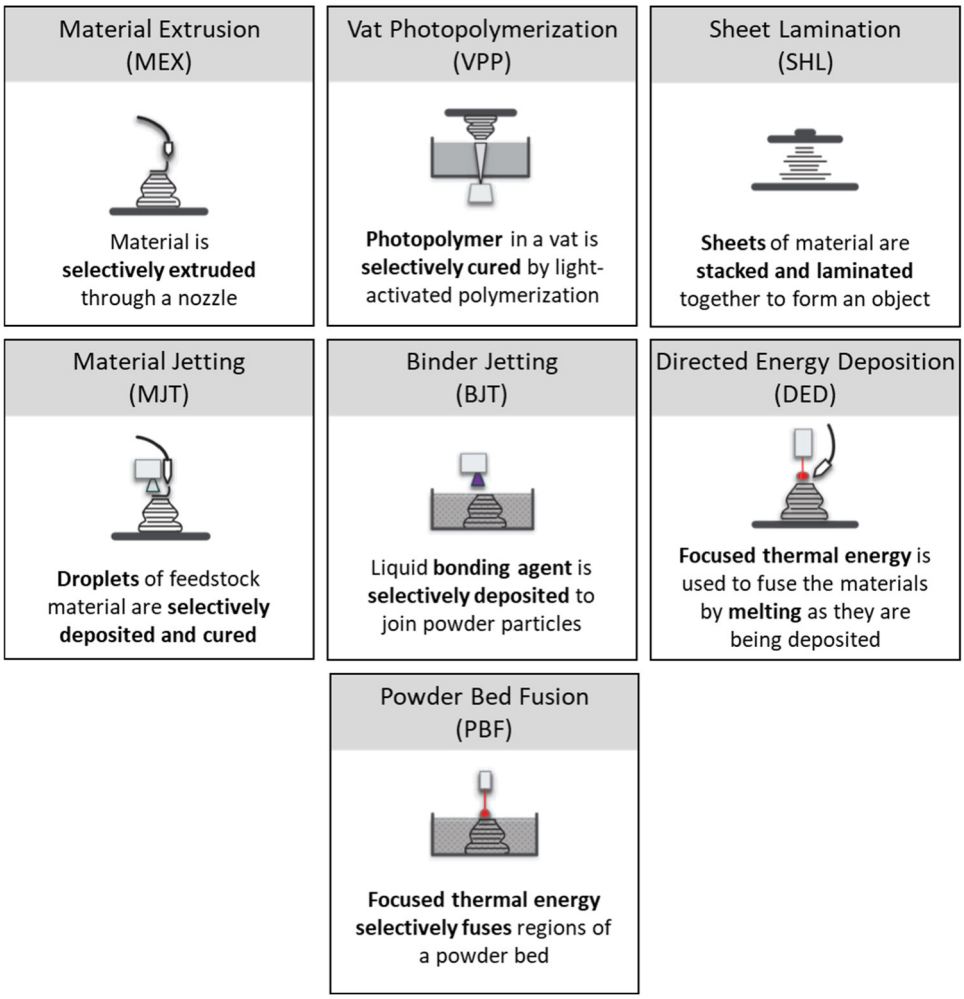


Figure 2 – The seven AM categories according to ISO/ASTM 52900 (2021) norm [37]. (Icons from [45])

2.2. Metal Additive Manufacturing

In the late 1990s, metal AM started to gain some attention with systems that allowed the processing of these materials in a layer-wise manner [2,42,46]. Similar to polymer AM, metal AM applications first started with rapid prototyping and advanced into end-use products in various industries [4,47].

Metal AM encompasses six of the seven AM categories represented in Figure 2: PBF, DED, SHL, MJT, BJT, and MEX, with all of them capable of producing fully dense parts, but the first two are the most widely researched and used [4,40,41,48]. These categories are also subdivided based on the energy source applied to melt the feedstock material. PBF processes employ a laser or an electron beam to selectively melt powder particles in a powder bed, while DED processes rely on these energy sources or a wire arc to create a melt pool into which the feedstock material (either in the form of powder or wire) is delivered [4,40,46,49]. The following section will focus on laser-based powder bed fusion (PBF-LB), which was the process used to produce the parts studied in this thesis.

2.2.1. Laser-based powder bed fusion

PBF-LB evolved from the Selective Laser Sintering process developed in the late 1980s and is currently the most popular category of metal AM, due to its ability to process a variety of metals with almost full relative density [4,43]. In the PBF-LB process, a laser beam selectively melts areas of a thin layer of metallic powder, typically ranging from 20-100μm, that is spread over a substrate or a previously deposited powder layer by a recoating mechanism. This process occurs in a closed chamber under an inert gas to avoid any reaction with the atmosphere, such as oxidation [2,4,9,40,47]. A schematic of the PBF-LB process is presented in Figure 3.

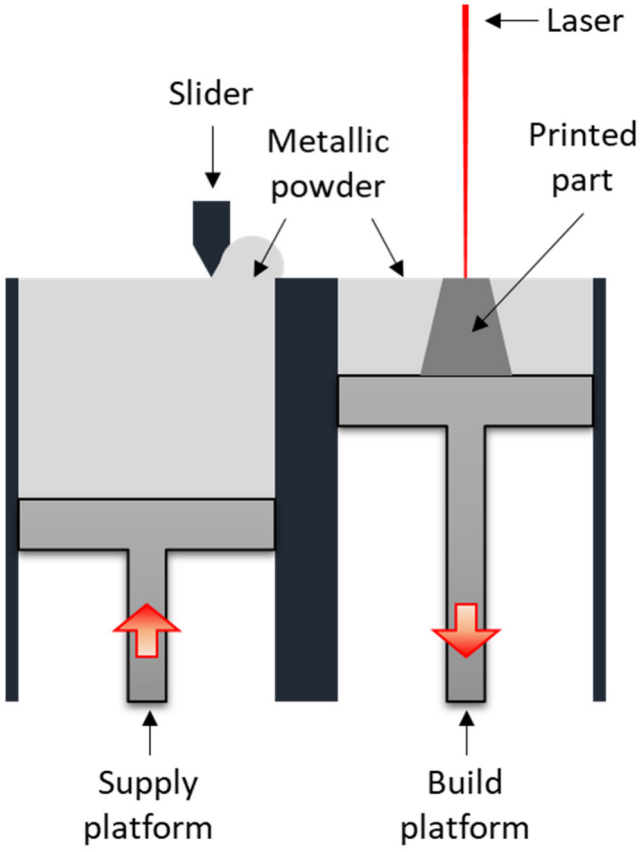


Figure 3 – PBF-LB process schematic. Metallic powder is loaded onto the supply platform, which moves incrementally upwards after each layer. The slider spreads a thin layer of the metallic powder (20-100μm) over the build platform, which lowers incrementally after each layer. The laser beam selectively melts the powder particles in each layer according to the relevant cross-section of the CAD.

The quality and density of the printed parts are strongly dependent on powder characteristics (e.g., chemical composition, particle shape and size distribution, powder flowability) and on process parameters (e.g., laser type, spot size diameter, laser power, scanning speed, hatch distance, layer thickness) [42,50].The volumetric energy density (VED) in Equation (1), given in J/mm³, establishes a relationship between relevant process parameters, where P is the laser power, s is the scanning speed, h is the hatch distance, and l is the layer thickness.

$$VED = \frac{P}{s * h * l} \quad (1)$$

Each metal has its own processing window, i.e., a range of VED, in which nominally dense parts are achieved. In general, a too low VED leads to lack of fusion, while a too high VED leads to keyhole porosity [4,43].

2.3. Metal Multi-material Additive Manufacturing

Similar to single-material AM, the first MMAM machines and processes were developed for polymers, due to reduced complexity and cost in comparison with metals and ceramics. Again, the first MMAM polymer parts served as prototypes for the potential applications of MMAM techniques. These join the aforementioned advantages of AM (geometric complexity, part customization, and design freedom) with the possibility of adding different functionalities and properties at strategic regions of the manufactured components [6–8]. A multi-material part can integrate functions of different materials within the same component to achieve desired properties, such as higher corrosion resistance, lower density, biocompatibility and higher thermal or electrical conductivity, at specific locations. This could therefore fulfill demands on parts from the aerospace, energy, biomedical, automotive, construction, and molding industries, resulting in potential advances in the fabrication of heat exchangers, electrical devices, implants, combustion chambers, wear-resistant components, cutting tools, etc. [7–10]. The harsh environments from the aerospace and energy industries, which could include high temperatures, high loads, and high corrosion, would benefit from parts that combine a material with high temperature and corrosion resistance with a material with higher strength, for example. In the biomedical industry, an implant with fine features that combine biocompatibility and stiffness from different metals could be manufactured by MMAM [7]. The performance of different molds could also be improved by adding internal cooling channels made of a material with higher thermal conductivity than the material used for the mold itself, which in turn should present a high wear resistance [51]. MMAM can also be applied to manufacture metamaterials, i.e., materials with an engineered design to achieve an artificial property, which is the main core of this thesis and will be further explained in Chapter 3 (references available in Table 2). In these examples, the parts with a specifically designed material distribution not only have a better performance than their single-material counterparts, but also bypass post-processing steps to join two different materials by conventional methods, increasing geometric freedom and reducing weight [7].

Conventional joining methods for metals include (1) metallurgical bonding by welding techniques, which can lead to thermal stresses and undesirable phase formation, and (2) mechanical bonding (such as rivets, bolts and nuts), which requires a minimum size of the components. This restricts the shape of the parts to be bonded and increases the weight to the manufactured part. In MMAM, two metals can be joined with unique bonding strategies and interface designs to achieve a bond superior to that of welding with less stress build up. This can be done without the need to change or enlarge the design of the component to accommodate a screw or a thread, for example [6,7,9]. However, challenges may arise when attempting to bond two dissimilar metals and this will be addressed in section 2.3.2.

2.3.1. Current MMAM systems available for metal PBF-LB

Although there are many commercial machines available for metal AM, most of them are limited to the manufacture of a single material, due to machine restrictions and the technical complexity of adding a second material to the process [6,9,10]. Wire and powder DED were, for a long time, the only processes capable of doing metallic MMAM, due to their higher flexibility, enabling the addition of one or more feedstock materials which could be delivered concurrently to the melt pool, without interfering with the inherent machine design [6,8,9]. Powder laser-based DED (DED-LB) easily allows the manufacture of functionally graded materials (FGMs) by mixing different weight ratios of powder from each hopper as the component is being built, creating a gradual interface from one material to the other. DED-LB also has the possibility of being introduced in a hybrid machine, where both additive and subtractive manufacturing can be done, by coupling a DED-head instead of a milling tool to the machine's spindle. On the other hand, PBF-LB produces parts with higher resolution, due to its smaller laser spot size and lower layer thickness, enabling parts with finer features to be printed, reducing or dispensing of the need for post-processing [7,9,41,52]. Therefore, due to its higher surface quality and dimensional accuracy, many different systems were developed in recent years to use PBF-LB to manufacture parts containing multiple materials [10,36,48].

In the literature, the multi-material PBF-LB processes are subdivided into two main categories, shown as schematics in Figure 4, depending on how the different metals are distributed in the build platform: (1) interlayer or 2D multi-material (Figure 4a) and (2) intralayer or 3D multi-material (Figure 4b) [7,53]. In the first category, multiple materials can be deposited, but only a single material is deposited per layer, i.e., the material changes occur only in the Z- or build direction, allowing only horizontal interfaces. In the second category, two or multiple materials can be deposited within the same layer, enabling more complex material interfaces.

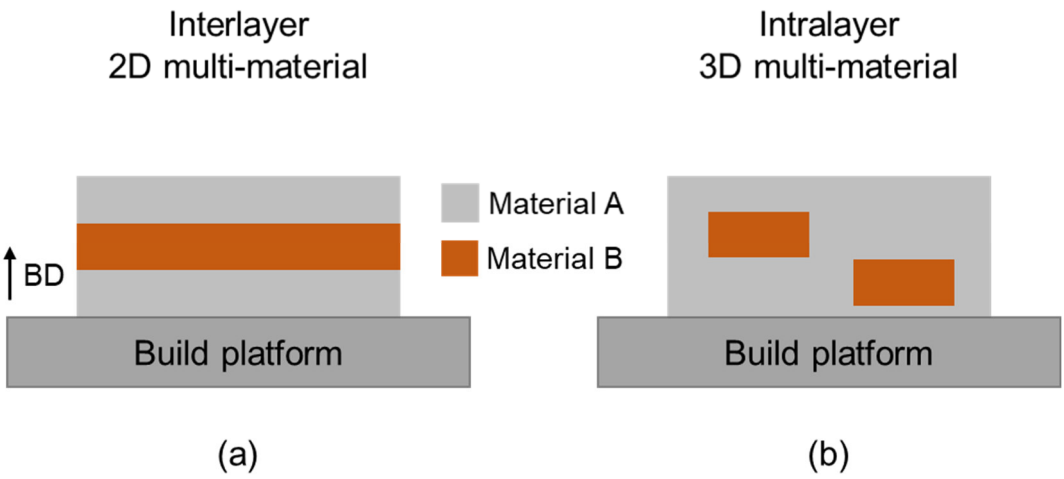


Figure 4 – Categories of multi-material PBF-LB: (a) interlayer or 2D multi-material, in which the material change occurs in the build direction, allowing manufacture of only horizontal interfaces; and (b) intralayer or 3D multi-material, in which two or more materials can be deposited within the same layer.

There are three ways of printing multi-material parts with the PBF-LB process: (1) when the substrate and the printed material are dissimilar metals, (2) when the supplied powder is manually changed during the single material printing process and (3) when the powder feeding system of an

PBF-LB machine is adapted or a special equipment is installed into it to perform MMAM. While the first two situations are restricted to 2D multi-material, the latter enables both 2D and 3D multi-material printing [7]. In this chapter, only multi-material works completed with the third method will be addressed.

Different machine adaptations and systems have been developed for multi-material PBF-LB, and several authors have suggested different classifications and naming conventions for each of them [10,36,48,54]. Schneck *et al.* (2021) [54] suggested three categories of multi-material powder bed systems: holohedral, nozzle-based, and masked. Wei *et al.* (2021) [48] classified the systems into 4 major categories: blade-based, ultrasonic-based, "blade and ultrasonic" hybrid, and electrographic-based. Neirinck *et al*. (2021) [36] and Mussatto (2022) [10] suggested a more detailed classification, subdividing the systems into 6 categories, which will be briefly explained and later compared in Table 1.

1. Alternating powder deposition: the machine is equipped with two powder supply pistons, one on each side of the machine. This system can be customized in a machine, but there are few commercially available options. The user is able to choose which material should be deposited in each layer, allowing only 2D multi-material parts [10,36,55,56].
2. Hopper powder feeding: this category applies a similar approach to the first one, but here the powders are delivered from hoppers, which can be mounted either within or external to the machine. However, it differs from the first category, as these systems can be adapted to blend the powders prior to the layer deposition or create material gradients within the same layer, allowing the printing of FGMs in the PBF-LB process and 3D multi-material printing [57].
3. Powder spreading with removal by suction: in the first step of this method, a single material powder layer is spread and exposed to the laser, then the unfused powder is removed by suction and, finally, the second material is spread and exposed to the laser. This process allows 3D multi-material printing, but only by using sequential deposition and exposure to the laser, excluding the possibility of applying different scanning strategies at the materials' interface [53,54,58].
4. Vibrating nozzles or pipettes: an ultrasonic vibration-assisted powder delivering nozzle deposits powders locally using gravity through small diameter orifices. The nozzles can either create a multi-material powder bed or work similarly to the previous category, where a powder bed of a single material is first deposited and exposed to the laser beam, and then a nozzle locally removes unfused powder by suction, and replaces it with a second material [59].
5. Electrophotographic powder deposition: the powder deposition process developed by Sintef pioneered the multi-material powder beds and works based on electrostatic attraction. An electric field charges a photoreceptor plate, which is subsequently exposed to a light projecting the image of the layer to be deposited. By doing this, the electrostatic charge is retained only where there was light exposure. The locally charged plate then attracts powder particles from a powder bed and deposits them onto a build plate [60–62].
6. Patterning drums: in this process, developed by Schaeffler Aerosint, a drum-based recoater selectively deposits powder, which is adhered to a drum via a negative suction pressure, via a point-by-point controlled micro-airflow onto a base plate. Each drum deposits a single material 2D image of the layer by selectively triggering actuators responsible for the ejection of the powder particles from the drum, combining to create a full powder layer containing multiple materials [63].

Table 1 – Advantages and limitations of the developed systems for multi-material PBF-LB.

Category		Advantages	Limitations
1	**Alternating powder deposition**	• Commercially available options • Can be easily added to adapted single-material PBF-LB machines • Relatively fast layer deposition	• Only 2D multi-material, i.e., horizontal interfaces
2	**Hopper feeding system**	• Gradient material transitions within the same layer and in the build direction are possible (FGMs)	• Powder gradient within the same layer is difficult to control • Limited design complexity, as intricate powder patterns are unable to be deposited (material variation is restricted to a single direction even within the same layer)
3	**Powder spreading with removal by suction**	• Reduced cross-contamination within the same layer • Control over the location of the different powders	• Removal and reapplication of powder reduces precision and productivity • Impossible to scan two materials with the same laser vector, limiting joining strategies
4	**Vibrating nozzle**	• Nozzles are relatively cheap (cheap maintenance) • Discrete and gradient material transitions within the same layer and in the build direction are possible (FGMs) • Control over the location of the different powders	• Powder flow from the nozzles is difficult to regulate, as many factors influence the powder's potential and kinetic energy • The powder delivery method usually leads to low-density powder beds
5	**Electrophotographic powder deposition**	• Control over the location of the different powders	• Quality and resolution of the part is strongly dependent on the electrostatic properties of the powders
6	**Patterning drums**	• Commercially available system that can be integrated into existing PBF-LB machines • Ensured repeatability after powder alignment procedures • Control over the location of the different powders	• The number of possible materials that can be deposited is restricted by the number of drums that fit into the machine • Resolution is dependent on the size of and spacing between the actuators for powder deposition

Besides the alternating powder deposition, which is basically a single material PBF-LB process with two powder supply pistons, the other systems require a longer time for the layer deposition than the traditional process, considerably increasing the printing time [10,36]. In a comparison between all the developed systems, Mussatto (2022) [10] characterized the hopper feeding system and the patterning drums technique as slow processes, while the remaining categories were characterized as very slow processes. Therefore, considering all the systems described in this chapter, the only one that allows 3D multi-material printing at a reasonable pace, with the freedom to apply various joining strategies at the interface, which is commercially available, is the patterning drums technique developed by Schaeffler Aerosint, which was the process further applied in this thesis and detailed in Chapter 4 .

2.3.2. Multi-material challenges

While the challenge of depositing more than one material onto a powder bed was overcome by the development of the aforementioned systems, new technical and metallurgical challenges arise from these multi-material systems. A general challenge is the powder contamination, not only from an economic and ecological point of view, which makes powder recycling nearly impossible, but also when it comes to cross-contamination within the powder layer, leading to possible defects in the printed part [7,8,10,36]. Anstaett *et al*. (2017) [53], for example, found particles of CuCrZr, which they called “alien particles”, in areas where only 12.709 steel was expected and vice-versa, although the technique with powder spreading with removal by suction was employed, which, in theory, reduces the cross-contamination. These particles were not well dissolved into the material “matrix” and were pointed out as possible sources for cracks. In other multi-material systems that do not utilize a powder removal procedure before feeding the next powder, the cross-contamination is higher at the interfaces of powder patterns, which cannot be as discretely defined as the laser vectors, often leading to an increased mixture of the two alloys at the interface. This issue can be particularly harmful when two dissimilar alloys, with very different miscibility, wetting properties, and process parameters (i.e., VEDs), are printed together [9].

One of the biggest challenges in metal MMAM, which makes it more complex than single material PBF-LB, is to achieve a good bonding between the two or more materials being printed. Due to the different thermal, chemical, optical, and physical properties of the materials (e.g., thermal conductivity, laser absorptivity, and melting temperature), each one requires different process parameters to be printed. The application of unsuitable parameters can lead to process defects, including porosity, balling, cracking, unmelted particles, and delamination. In an intralayer multi-material process, since an increased material mixture leads to an imprecise borderline between the two different powder patterns, there is a larger chance of applying the process parameters of one material onto the other material. This could compromise the bonding between them and could lead to the failure of the multi-material part [7–10,41,48]. A possible solution is to add an intermediate bonding layer, made of a third material that is chemically compatible with the other two materials, instead of a direct bonding between them. Although this approach has proven to be successful in welding processes, for example, this would require a multi-material system able to deposit three materials. While this is the case for the newest version of the Schaeffler Aerosint recoater [64], most of the multi-material systems were developed for only two feedstock materials. Some authors also suggest that a gradient transition between the materials, as in FGMs, leads to less abrupt process parameter changes, hence increasing the bonding strength between the two

materials [7,41,48]. However, most of the multi-material powder bed systems allow only discrete material transitions. Furthermore, while an increase in material mixture could potentially improve the bonding between two materials, it is not necessarily a defect-free approach, especially if the materials are not compatible with each other [65].

From a metallurgical point of view, material mixtures are not only an issue because of the different process parameters they may require, but also because of the potential formation of brittle intermetallic phases. These can lead to high residual stresses, delamination, and cracks in multi-material structures [7,9]. Intermetallic phases tend to form between metal elements that are relatively different in terms of atomic radius, and crystal lattice. These elements diffuse and combine whilst molten in the PBF-LB process, precipitating new phases, which can contain differing atomic ratios of these elements, depending on how much of each is available within the molten metal. Although PBF-LB is considered a non-equilibrium process, these intermetallic phases can often be predicted by equilibrium phase diagrams and are often brittle, making the material interface more susceptible to cracks and delamination. These defects can occur not only in the end-use application, but also during the printing process, due to the residual stresses caused by the thermal history induced by the PBF-LB process. Besides the addition of an intermediate layer made of a third material, a possible solution is to add alloying elements in the materials that thermodynamically inhibit the formation of these brittle phases. For that, a calculation of the phase diagram considering the alloying elements would be necessary [48]. Finally, the most viable alternative to avoid intermetallic phase formation at the interface relies on the choice of the material combination, which can be selected based on their metallurgical compatibility and absence of brittle phases in their phase diagram.

Aside from intermetallic phase formation, elemental segregation, due to reduced miscibility between the materials, and liquid metal embrittlement, which induces cracks in the typically researched Fe-Cu combination, are also possible metallurgical defects that can occur in MMAM [48]. Regardless of their origin, cracks, pores, and delamination weaken the interface between the materials, compromising the mechanical and fatigue properties of the printed part. Therefore, some studies have been conducted in recent years on bonding strategies to avoid or heal these defects [7,41].

As well as the already mentioned bonding strategies of direct bonding, intermediate layer, and gradient material transitions, studies were done on the optimization of process parameters and scanning strategies at the materials' interface to reduce defects, such as porosity and cracks [53,65–67]. Successful approaches include different scanning sequences [53], laser beam shaping [65,67] , special scanning strategies at the interface, such as laser wobble [67] and remelt [66,68–70], unique process parameters for the interlayers [67], and adjusting the VED applied in each layer, until material mixing no longer occurs, which is initially driven by the circular flow induced by the Marangoni effect.

While the majority of previous work focuses on strategies to achieve defect-free horizontal or vertical interfaces between dissimilar metals which cannot be printed with the same process parameters, no research had been done on strategies for similar metals, which have the same process parameters. In this thesis, different scanning strategies have also shown to impact the quality of the interfaces between two similar metals, Invar and Inconel 718. These results will be addressed in section 5.1, concerning P{1} .

2.3.3. Known material combinations

Wei *et al*. (2021) [48], Schneck *et al*. (2021) [54], and ZainElabdeen *et al*. (2024) [41] listed previously published works, showing the combinations of metals that had been studied in PBF-LB, including 2D multi-material approaches. Up to this point, many works have been conducted between similar metals, i.e., a combination of different steels, different Al-, or Ti-alloys; while among the dissimilar metal combinations, the most popular combinations were in the Fe-Cu system, with only a few papers (less than three, often just one) in other systems, such as Ag-Cu, Al-Cu, Al-Mg, Fe-Ni, Ni-Cu, Ni-Ti, Ti-Fe, and Ti-Al.

While compatible metal combinations typically form strong interfaces, with good bonding, dissimilar metal combinations are more prone to the aforementioned defects at the interface, with some pairings posing greater challenges than others [41,48]. The Fe-Ni system, which represents the material combination studied in this thesis, for example, is associated with the risk of hot cracking and elemental segregation, with the formation of Laves phase [41]. Some of the previous works with this system, listed by ZainElabdeen *et al*. (2024) [41], reported these defects, while others were able to achieve a pore- and crack-free interface between the materials, as they usually present a broad chemical compatibility and process window [66,71,72].

The choice for the material combination is largely dictated by the desired functional properties of the final part, but factors related to the processability should also be considered. Since the main objective of this thesis was to develop a metamaterial intended for a satellite experiment, it was critical to avoid the formation of cracks and brittle intermetallic phases between the materials to maintain the structural integrity of the metamaterial. Therefore, combinations in the literature that have previously led to defective interfaces were discarded and metallurgically compatible alloys were sought. Among the combinations that could fulfill both functional and processability requirements, in the Fe-Fe or the Fe-Ni system, Invar and Inconel 718 were chosen. These materials are not only compatible with each other, but are also printable with the same process parameters. Moreover, their large CTE difference is crucial to build metamaterials with negative CTE, as it will be explained in Chapter 3.

3. Metamaterials with negative coefficient of thermal expansion

The first published work with a detailed description of cellular solids and their properties was written by Gibson and Ashby in 1988 [73]. These structures are defined as lightweight materials made of an arrangement of interconnected solid struts or plates, which form a cell, or a *unit* cell, if they are a repeating unit in a periodically arranged lattice structure. The cells can be either open- or closed-cells and arranged in a periodic or stochastic manner, which can be spatially distributed in 2D or 3D forms. Although the properties of the cellular solids derive from their constituent materials, they extend the range of available properties of the bulk materials, allowing, for example, a higher strength/stiffness-to-weight ratio, ductility, energy absorption, or lower thermal conductivity. Some examples of these structures in nature are wood and cork, which inspired the development of similar artificial cellular solids to achieve desired physical, mechanical, thermal, electrical, magnetic, optical, and acoustic properties [11,73–76].

The term *metamaterial* refers to architected materials, based on lattice or cellular structures, that achieve extraordinary properties, which are not achievable by natural solid materials. These properties derive not only from their constituent materials, but also, and mostly, from their geometrical structure and spatial arrangement [11,15,22]. In recent decades, many metamaterials with tunable material properties have been proposed for various applications in several engineering fields, such as aerospace, automotive, and biomedical [12,77,78]. The engineered properties include, among others, negative Poisson's ratio, negative compressibility, negative refraction index, negative magnetic permeability, and negative coefficient of thermal expansion (CTE) [12,18]. Wu *et al*. (2025) [11] classified metamaterials in four categories, depending on their functionalities: mechanical, thermal, electromagnetic, and acoustic metamaterials.

Metamaterials with tunable CTE can be found within the category of mechanical metamaterials [11,18]. Thermal expansion, which is the increase of volume upon heating, is a critical limiting property in applications involving large temperature variations, temperature-sensitive devices, and high-precision systems, as it can lead to undesirable distortions and thermomechanical stresses. Therefore, the control of material expansion is of special interest [15,19,21,29]. While most materials present a positive CTE (PTE), i.e., expanding when heated, because of the increase in the kinetic energy of molecules and atoms, a few present a natural negative CTE (NTE), i.e., shrinking when heated. In Figure 5, the ranges of the possible CTEs found in each material group are depicted, together with the CTE range found in metamaterials with tunable CTE which have been manufactured up to this point.

Naturally found NTE is limited to some advanced materials, such as metallic glasses, ceramics, and fiber-reinforced composites, and a few natural solids with isotropic NTE, such as zirconium tungstate (ZrW_2O_8), and a few metal oxides with anisotropic NTE (e.g., $Sc_2W_3O_{12}$, $NaZr_2(PO_4)_3$, and $PbTiO_3$ perovskite). However, ceramic materials and glasses are inherently brittle and present very limited fracture toughness for many applications. The limitation of the fiber-reinforced composites is down to their anisotropic NTE and the large CTE mismatch between the fibers and the matrix, which often leads to excessive thermal stresses and failure. Moreover, ceramics and fiber-reinforced composites present limited processability, restricting the size and the shape of the structures built with them [17,21,24,27,30,79–81]. For the reasons outlined, metals with intrinsically low CTE are frequently used as an alternative for high-precision instruments, despite their limitations. The main drawbacks are that they (1) present low, yet positive CTEs and (2) this

property is observed in a limited temperature range. The commercially known Invar-36, or just Invar, a binary Fe-Ni alloy that contains approximately 36 wt.% in Ni content, presents CTEs lower than $2x10^{-6}$/K, which is comparable to some ceramics, but only below its Curie temperature[2], at approximately 230°C. This behavior is also called “Invar effect”. [17,30,81,83,84].

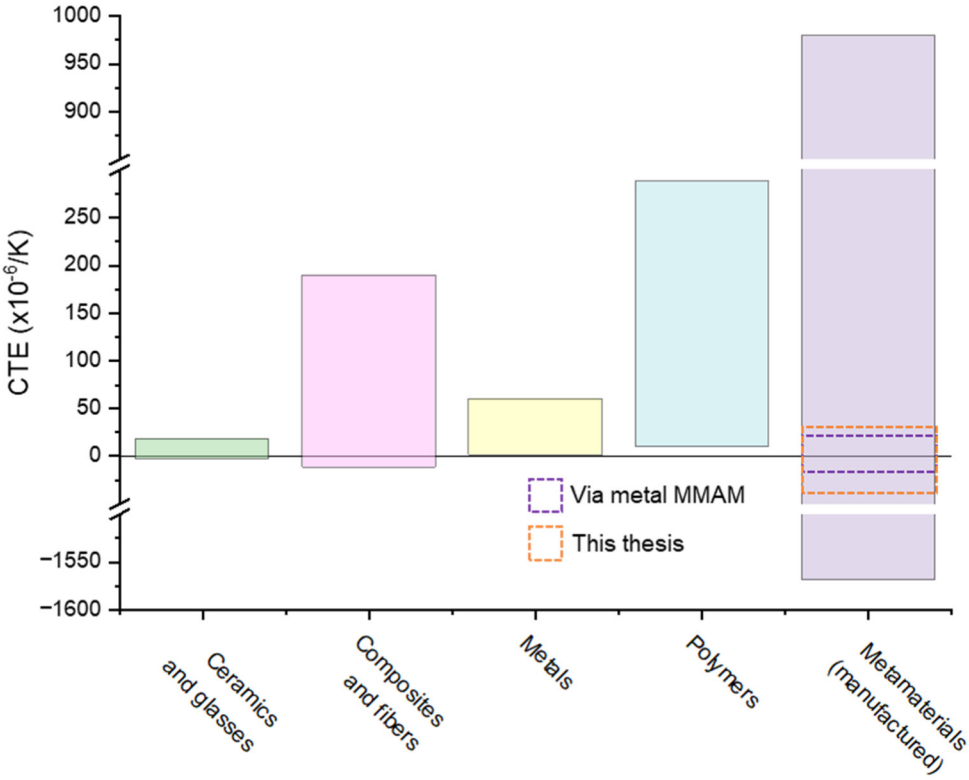


Figure 5 – Range of possible CTEs for each material category. Only metamaterials that were manufactured (conventionally or by AM) were considered for the CTE range of the metamaterials. The range of the metamaterials fabricated via metal MMAM of previous works is highlighted, as well as the range found in this thesis. For metamaterial references, see Table 2. Source for other materials: Granta EduPack 2025 R1 – Level 3 database.

Due to the limited material options for controllable CTE applications, many metamaterial designs have been proposed to tailor the CTE to a desired value, while maintaining adequate mechanical properties for engineering applications [17,18]. Although achieving a zero CTE (ZTE) is an intuitive solution for ensuring dimensional stability under temperature variations, NTEs are particularly useful to compensate for thermal expansions of natural PTE materials within a system, resulting in an effective overall ZTE. On the other hand, metamaterials with large PTEs can be potentially used as actuators [21,27,28,30,80,85,86]. For clarity, this chapter will focus primarily on NTE metamaterials, but ZTEs and PTEs will also be discussed where relevant.

Although NTE can be achieved by different mechanisms in a metamaterial, all the suggested designs found in literature present a common feature: they are composed of at least two different

[2] Invar is a ferromagnetic alloy and the mechanism that allows it to present very low CTEs is called magnetovolume effect. Above the Curie temperature, Invar loses its ferromagnetic properties, and the magnetovolume effect disappears. As a result, its CTE increases significantly, approaching the typical values for metals (i.e. above $12x10^{-6}$/K) [82].

materials with a large CTE difference between them [17,29,87,88]. Xu *et al*. (2018) [17] and Zhang *et al*. (2024) [18] present an overview of the studied NTE metamaterials in the literature and categorize them into different groups, according to their routes or principles to achieve the NTE.

In Figure 6, the four main design routes to achieve NTEs are presented as schematics: bi-material strips, cored-struts, the triangle mechanism, and topology optimized structures [17]. The bi-material strips work based on a bending-dominated principle: upon an increase in temperature, the material with higher CTE expands more than the material with lower CTE, causing the bi-material strip to bend, thus presenting an NTE in X-direction. This movement characterizes the principle of bending-dominated lattice structures. The cored-struts operate based on a coupling between thermal expansion and the Poisson effect: upon an increase in temperature, the inner core stretches the outer material circumferentially, leading to a Poisson contraction in the axial direction. In the triangle mechanism, the material with higher CTE is used for the base of the triangle, while the lower CTE material is used for the triangle's sides. As the temperature rises, the base expands more than the sides, forcing the triangle to deform and leading to an NTE in the Y-direction. The deformation mechanism of the cored-struts and the triangle mechanism characterizes the principle of stretching-dominated lattice structures. At last, the topology optimized structures can work based on one or both of bending- and stretching-dominated principles, but with a mathematically optimized material distribution. This optimization aims to maximize specific properties, e.g., bulk modulus, while still achieving a target NTE [27,89]. Any of these routes can be spatially arranged and combined with similar elements to achieve the NTE in two directions (2D models or 2.5D, if they are extruded in a third dimension) or in three directions (3D models), enabling isotropic NTE. Examples found in the literature of 2D/2.5D and 3D models of each route are shown in Figure 6.

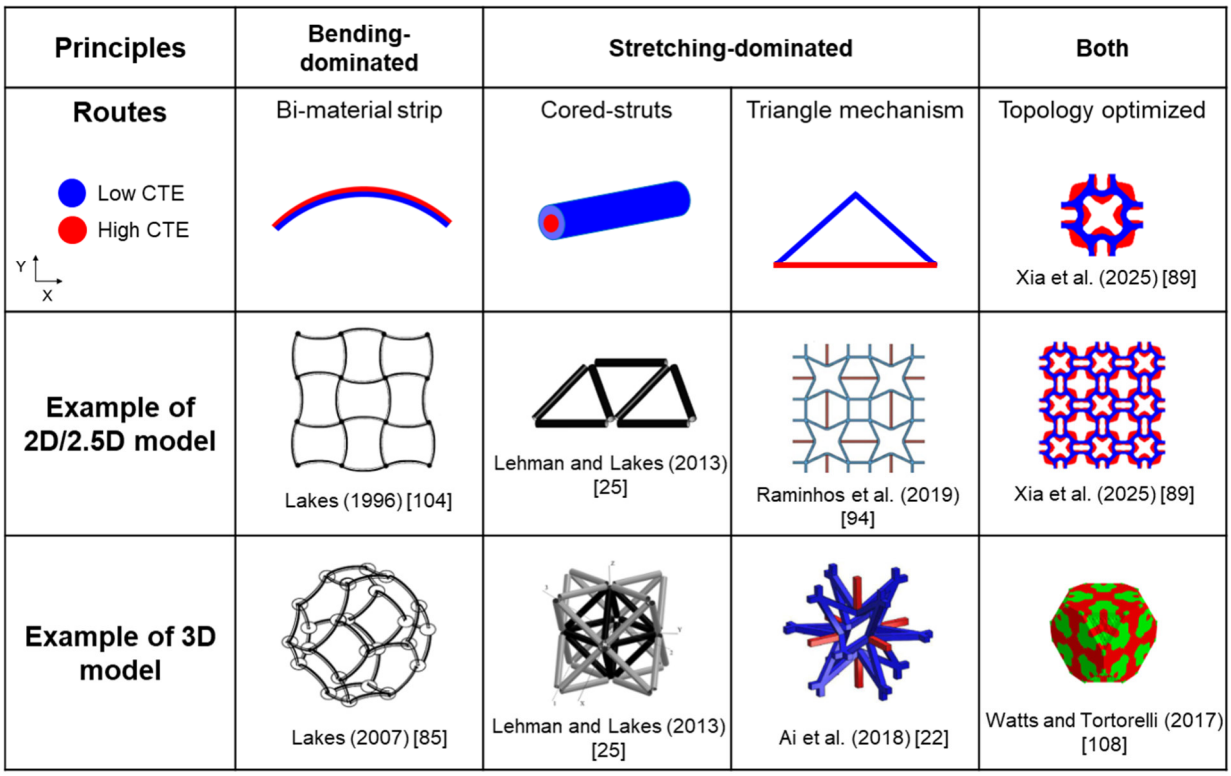


Figure 6 – Types of metamaterials with tunable CTE found in the literature. The four routes, which can be categorized into bending- or stretching-dominated or both, are depicted, with examples of 2D/2.5D and 3D models found in the literature.

In Figure 7, from Zhang *et al*. (2024) [18], other examples of tunable CTE metamaterials found in the literature are shown. Zhang *et al*. (2024) categorized the structures proposed in the literature according to the two main principles used to tune their CTE: bending- and stretching-dominated. In general, bending-dominated lattices exhibit more pronounced NTEs, whereas the stretching-dominated structures provide higher stiffness [15,18]. Bending-dominated structures can be further classified as chiral or achiral, depending on their rotational response upon rising temperatures. Their geometry can only be tuned to achieve CTEs lower than those of their parent materials, as the bi-material strips inherently bend in a single direction. In contrast, stretching-dominated structures allow greater tunability. By reversing the material assignment within the triangle structure, both NTE and PTE can be achieved. When the low CTE material is assigned to the triangle's base and the high CTE material to its sides, the structure responds in the opposite way, acting to induce CTEs higher than those of their parent materials [18]. This configuration is referred to as the "explicit" subdivision in Figure 7.

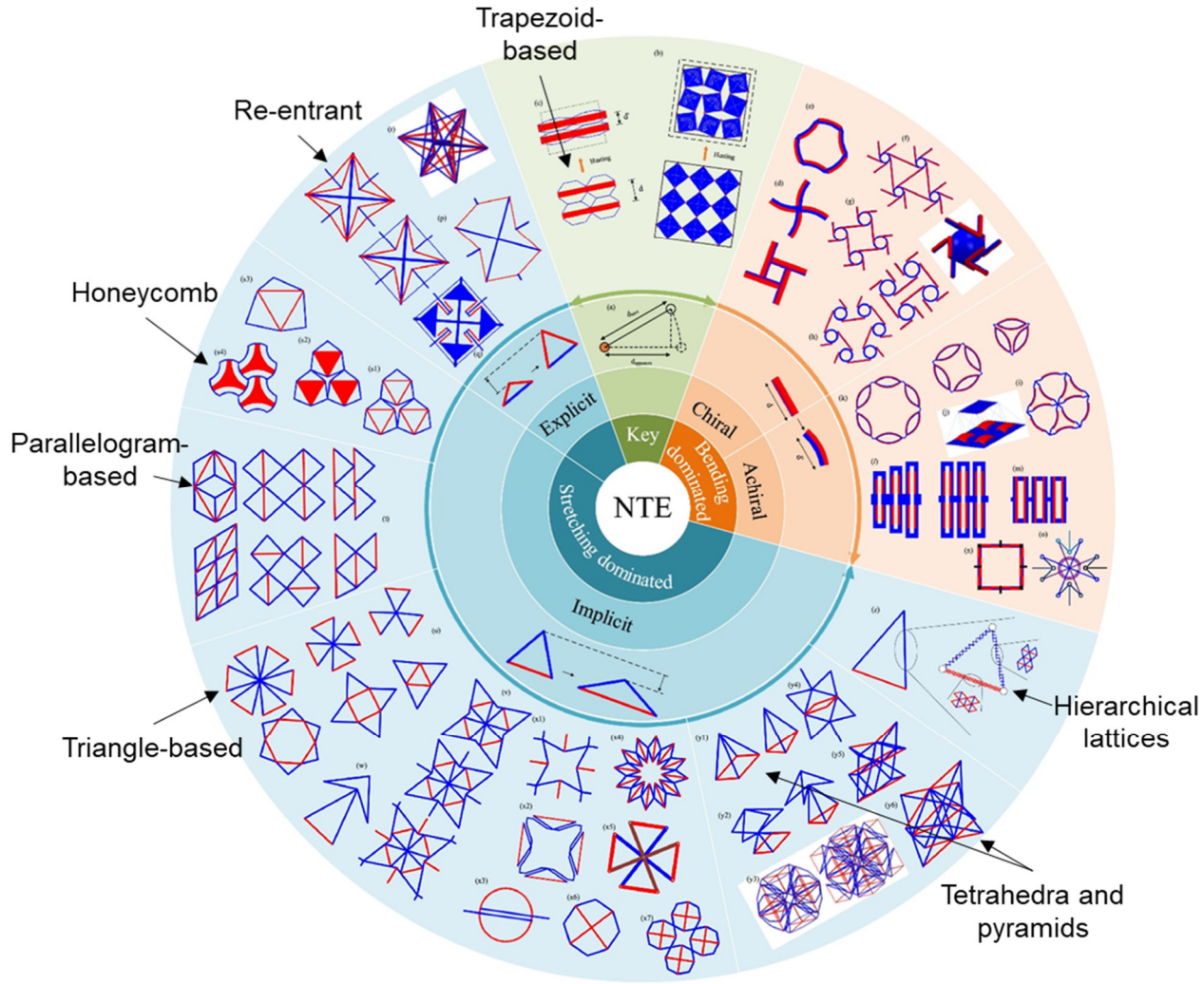


Figure 7 – Examples of geometries of metamaterials with tunable CTE developed in the literature, divided into bending- and stretching-dominated lattice structures. Some categories of geometries for stretching-dominated structures, which will be mentioned in 3.2, are pointed. Source: Zhang et al. *(2024) [18].*

3.1. Manufacturing of metamaterials

In general, due to their intricate geometries and often millimeter- to micrometer-sized unit cells, metamaterials of any kind are difficult to fabricate using traditional manufacturing methods. Therefore, the design and production of the metamaterials have significantly benefited from advances in AM techniques [11,12,87,90,91]. However, the manufacturing of metamaterials with tunable CTE is particularly challenging due to the need for at least two different materials. For this reason, the research on these structures remains less mature compared to other types of metamaterials, such as those with negative Poisson's ratio and negative stiffness metamaterials [18,80].

Since MMAM techniques only became available relatively recently, early attempts to fabricate these metamaterials relied primarily on conventional manufacturing techniques, such as pin-joining [92], laser spot welding [29], gluing [28], bolting [30], interface fitting [81] or snap fitting [83]. Later, polymer MMAM [23,24,31,88,91,93,94] and, more recently, metal MMAM [33–35,95,96] were applied to print some NTE metamaterials. A more detailed review of the NTE structures that have been designed, simulated, and manufactured in this way will be detailed in the following section (3.2).

Due to its geometric freedom, possibility to print at the microscale, and the elimination of the need for additional joining techniques that could increase the fabrication complexity and constrain the geometry of the metamaterials, MMAM is considered the most suitable technology to manufacture NTE metamaterials [11,12]. However, it is important to note that even single-material AM of lattice structures presents significant challenges. Additionally, MMAM – even for bulk material – introduces its own sets of complexities, as discussed in the section 2.3.2.

Typical defects in metal PBF-LB – such as porosity, delamination, residual stresses, cracking, balling, and surface roughness – are also commonly found in lattice structures. Due to their thin struts, dimensional inaccuracies are also reported as a typical defect, as the size of the melt pool in PBF-LB often limits the precision with which fine features can be fabricated. Struts printed at overhanging angles (i.e., not perpendicular to the build plate and lacking solid material support beneath them) often exhibit geometric deviations, such as ellipsoidal cross-sections instead of circular ones, and positional deviations, commonly referred to as strut waviness [97]. The powder bed acts as an insulator, and the concentration of short, frequent laser tracks in localized regions can lead to overheating, further contributing to dimensional inaccuracies. Consequently, process parameters for bulk and lattice structures may differ, even when using the same material [75,97–99].

A well-known issue affecting the dimensional accuracy of the struts is the "staircase" effect. This occurs due to the layer-by-layer nature of the process, where inclined surfaces are approximated as a series of steps, resulting in a staircase appearance. Surface roughness is particularly pronounced on down-skin surfaces - surfaces of the struts that face downwards, and are printed directly onto the unmelted powder bed from previous layers – as the melt pool tends to integrate loose powder particles [97,98]. However, this is not the only challenge related to overhanging angles in the PBF-LB of lattice structures.

In Figure 8, different ranges of overhanging angles are represented. In general, overhangs with angles greater than 45° relative to the build plate (Figure 8a) are considered printable without supports. Angles below 45° (Figure 8b) typically require support structures to ensure printability, improve dimensional accuracy, and down-skin surface quality, and assist with heat dissipation,

minimizing residual stresses, and thus preventing distortions [97,98,100]. However, in lattice structures, support structures are not a viable option because unit cells are repeated multiple times throughout, which makes them inaccessible and practically impossible to remove [100]. Nonetheless, some studies have printed metamaterials with support structures as a compromise [101,102], others have applied innovative strategies, such as using a pulsed laser to print struts at angles as low as 20° [103], or optimizing process parameters to print horizontal struts (0°) between vertical struts spaced up to 7 mm apart, effectively forming a bridge [100]. While these approaches show potential for producing high-quality metamaterials using PBF-LB, they may not fully address specific challenges of NTE metamaterials with three-dimensional unit cells. These structures often require struts at "negative angles" (Figure 8c), as acute angles are essential for achieving lower CTEs [22,35]. This indicates that considerable research is still needed in this area. A further analysis of NTE structures reported in the literature is presented in the following section.

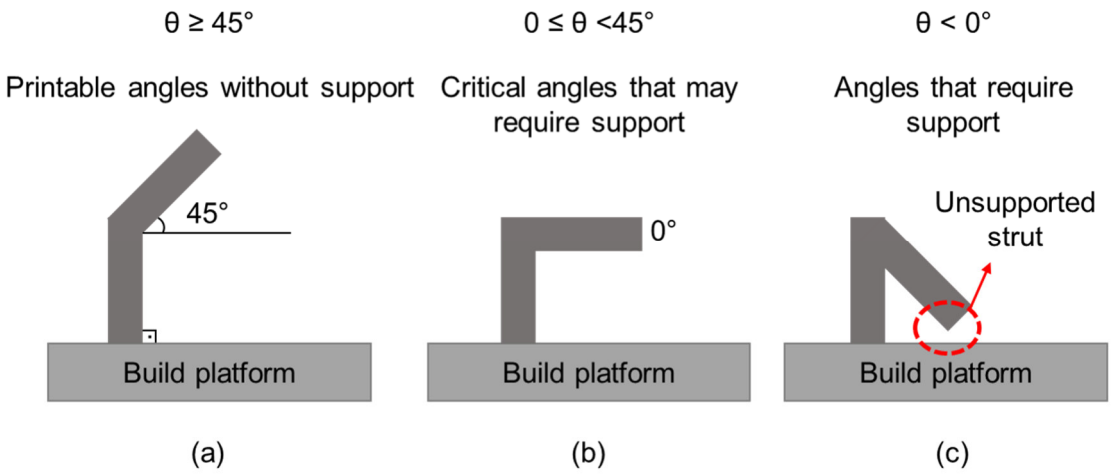


Figure 8 – Overhanging angles in PBF-LB lattice structures: (a) angles larger than 45° can be printed without support structures; (b) angles between 0° and 45° are critical and may require support structures, depending on the laser strategy used and the overhanging length; and (c) angles lower than 0° that would require support structures.

3.2. Chronological development of tunable CTE metamaterials

Up to this point, this chapter has provided an overview of modelling approaches for tunable CTE metamaterials and the associated manufacturing challenges. This current section summarizes the progress made in this field over time, based on the works listed in Table 2.

There has been a considerable amount of research in this area over the past three decades, initially focused on developing novel metamaterial designs and analytically or numerically assessing their theoretical CTEs. More recent work has been focusing not only on design and simulation of these metamaterials, but also on their manufacturing process, CTE measurement, and correlation with simulated values. The key works on tunable CTE metamaterials reviewed in this thesis are summarized chronologically in Table 2. In Table 2 the following details are presented: (1) which route was used to achieve the NTE (see Figure 6), (2) whether the geometry of the studied structures were in 2D (or 2.5D, if the 2D structure was extruded into the third dimension) or in 3D, (3) whether the CTE was calculated or simulated, (4) whether and how the structures were manufactured, and (5) whether and how their CTE was experimentally measured.

As can be observed from Table 2, with the exception of the study by Ding *et al*. (2018) [96], which mainly focused on the manufacturing process, all other works estimated the CTE of their proposed structures using either mathematical models or finite element method (FEM) simulations. It can also be seen that, due to their versatility in achieving both NTE and PTE structures, as well as their higher stiffness and lower manufacturing complexity, triangle mechanism-based designs have received greater attention in the literature.

Table 2 – Summary of previous studies about the design, manufacture and quantification of tunable CTE metamaterials in literature.

	Route				Geometry			Manufacturing			CTE meas.	
Paper	**Bi-material strips**	**Cored-struts**	**Triangle mechanism**	**Topology optimization**	**2D / 2.5D**	**3D**	**Calculated/Simulated CTE**	**Conventional techniques**	**MMAM - Polymer**	**MMAM - Metal**	**Optical / DIC**	**Dilatometry**
Lakes (1996) [104]	X				X		X					
Sigmund and Torquato (1996) [27]				X	X		X					
Lim (2005) [79]			X		X		X					
Steeves *et al*. (2007) [92]			X		X	X	X	X			X	
Lakes (2007) [85]	X				X	X	X					
Grima *et al*. (2008) [16]			X		X	X	X					
Miller *et al*. (2008) [26]			X		X	X	X					
Jefferson *et al*. (2009) [21]			X		X		X					
Lim (2012) [105] and Lim (2013) [106]			X		X	X	X					
Lehman and Lakes (2013) [25]		X			X	X	X					
Gdoutos *et al*. (2013) [29]			X		X		X	X			X	
Lehman and Lakes (2014) [107]	X	X			X	X	X					
Ha *et al*. (2015) [28]	X				X		X	X			X	
Wang *et al*. (2016) [23]			X			X	X		X		X	
Wei *et al*. (2016) [81]			X		X		X	X			X	
Wu *et al*. (2016) [24]	X				X	X	X	X	X		X	
Xu *et al*. (2016) [83]			X			X	X	X			X	
Xu *et al*. (2017) [77]			X		X		X	X			X	
Wei *et al*. (2017) [30]			X		X		X	X			X	
Takezawa and Kobashi (2017) [93]				X	X		X		X		X	
Qu *et al*. (2017) [31]	X					X	X		X		X	
Watts and Tortorelli (2017) [108]				X		X	X					
Ding *et al*. (2018) [96]			X		X					X		

	Route				Geometry			Manufacturing			CTE meas.	
Paper	**Bi-material strips**	**Cored-struts**	**Triangle mechanism**	**Topology optimization**	**2D / 2.5D**	**3D**	**Calculated/Simulated CTE**	**Conventional techniques**	**MMAM - Polymer**	**MMAM - Metal**	**Optical / DIC**	**Dilatometry**
Xu *et al*. (2018) [17]			X			X	X	X			X	
Wei *et al*. (2018) [86]			X			X	X					
Ai *et al*. (2018) [22]			X			X	X					
Zhang *et al*. (2019) [19]	X		X		X		X					
Li *et al*. (2019) [88]			X		X		X		X			
Parsons (2019) [95]			X		X		X			X	X	
Raminhos *et al*. (2019) [94]			X		X		X		X		X	
Chen *et al*. (2020) [109]			X		X	X	X					
Guo *et al*. (2021) [87]	X				X		X	X			X	
Wei *et al*. (2021) [91]			X		X		X		X		X	
Yu *et al*. (2021) [110]	X				X		X	X				
Zhang *et al*. (2024) [18]			X		X		X					
Zhang *et al*. (2024) [15]			X		X		X					
Bambach and Tucker (2024) [33]			X		X		X			X	X	
Cervinek *et al*. (2024) [34]			X		X		X			X	X	
Xia *et al*. (2025) [89]				X	X	X	X					
This thesis			**X**		**X**		**X**			**X**	**X**	**X**

The first appearances of tunable CTE metamaterials date back to the mid-1990s, beginning with the bi-material strip structure suggested by Lakes (1996) [104] and the topology optimized structures introduced by Sigmund and Torquato (1996) [27]. Later, Lakes (2007) [85] and Watts and Tortorelli (2017) [108] advanced these concepts by designing 3D geometries with isotropic NTE. Lehman and Lakes (2013 and 2014) [25,107] further proposed an octet-truss lattice – comprising eight tetrahedra, arranged on the faces of an octahedron – featuring cored-struts aimed at achieving isotropic CTE (3D model example shown for the cored-strut route in Figure 6). However, this approach was not further pursued in subsequent research.

Although Lim (2005) [79] and Steeves *et al*. (2007) [92] were the first to suggest structures based on the triangle mechanism (stretching-dominated structures), it was Miller *et al*. (2008) [26] and Grima *et al*. (2008) [16] who explicitly described this mechanism for tuning CTE and proposed metamaterials composed of interconnected triangles. Interestingly, Grima *et al*. (2018) [16] introduced bi- or tri-material structures that exhibit negative compressibility under pressure, operating under the same geometric principle, though not explicitly designed for negative CTE.

Between 2007 and 2013, more complex 3D geometries employing the triangle mechanism – often based on tetrahedra or pyramids – were proposed by Steeves *et al*. (2007) [92], Miller *et al*. (2008)

[26], Grima *et al*. (2008) [16] and Lim (2012 and 2013) [105,106]. Subsequently, new geometries were developed in both 2D/2.5D and 3D, including honeycomb structures [21], re-entrant structures [15,22,23,88], octet-trusses [83], hierarchical lattices [77], pyramids [17,86], parallelogram- [109] and trapezoid-based designs [18]. Examples of these categories of geometries are pointed in Figure 7, except for the octet-truss, which is graphically represented in Figure 6, as an example of 3D model for, in that case, a cored-strut.

By laser cutting aluminum and titanium alloy sheets and joining them via pinned or bonded joints, Steeves *et al*. (2007) [92] were the first to manufacture a unit cell of an NTE metamaterial, achieving a good agreement with the theoretically calculated CTE. Gdoutos *et al*. (2013) [29] fabricated a similar structure but assembled the two materials by laser spot welding. From that point on, several other studies have been published, reporting the fabrication of NTE unit cells and/or metamaterials (i.e., multiple unit cells combined). Most of these works include CTE measurements that closely matched their simulated or calculated values. Conventional joining techniques have been employed to fabricate NTE unit cells or metamaterials, as listed in section 3.1. However, as previously stated, these conventional methods constrain the geometry and size of the NTE metamaterials that can be manufactured. Moreover, these techniques require multiple steps to achieve the final structure.

With the emergence of polymer MMAM, some studies were done exploring its potential to print NTE metamaterials. In 2016, Wang *et al*. (2016) [23] fabricated a complex millimeter-scale re-entrant 3D geometry using PEGDA and reinforced PEGDA via multi-material polymer VPP (see Figure 2 for the description of the AM processes). The same technique was used by Qu *et al*. (2017) [31] to produce chiral lattices with bi-material strips at a micrometer scale. Li *et al*. (2019) [88] created various re-entrant 2.5D structures using the same process, though CTE measurements were not reported. Wu *et al*. (2016) [24] utilized a multi-material MJT process to print an achiral structure based on the bi-material strip concept, while Takezawa and Kobashi (2017) [93] applied the same technology to print topology optimized structures. Lastly, Raminhos *et al*. (2019) [94] and Wei *et al*. (2021) [91] used multi-material MEX to print NTE re-entrant 2.5D structures, and NTE and PTE unit cells of triangle structures.

These efforts in polymer MMAM played a key role in demonstrating AM's potential to fabricate NTE metamaterials, showing good correlation between measured and simulated/calculated CTEs. Nevertheless, metals are generally preferred in engineering applications due to their superior mechanical and thermal properties, including those that may benefit from NTE behavior, which will be further detailed in the next section (3.3). The first metallic NTE structure was reported by Ding *et al*. (2018) [96]. They used DED-LB to fabricate a re-entrant 2.5D metamaterial made of 316L stainless steel and Invar, but did not measure its CTE. One year later, Parsons (2019) [95] used SHL to alternate layers of aluminum and titanium alloys, from which triangular metamaterial structures were cut via electrical discharge machining. These metamaterials achieved an NTE behavior in alignment with simulations. However, the sheet-wise deposition approach from SHL limits the range of feasible geometries (similar to the 2D multi-material process shown in Figure 4a) and requires post-processing to extract the final structures.

Among the metal MMAM processes, PBF-LB is the most suitable for building these metamaterials, due to its superior resolution, surface quality, and dimensional accuracy compared to DED processes, and because it avoids post-processing steps, such as the cutting required by the SHL process [41,52]. However, as discussed in section 2.3, MMAM systems for PBF-LB have only recently become available, and thus the literature on tunable CTE metamaterials produced via

multi-material PBF-LB remains limited. Bambach and Tucker (2024) [33], along with Cervinek *et al*. (2024) [34] printed bi-metallic 2.5D structures based on the triangle principle using 316L stainless steel and the CuCrZr alloy. While they did not achieve NTE behavior, they measured CTEs lower than those of the parent materials [33,34], and the CTE could be tuned within a small positive range ($1.64x10^{-6}$/K to $2.51x10^{-6}$/K) by adjusting material distribution within the unit cell [34]. However, the degree of CTE tunability was limited due to the relatively small difference in CTE between the constituent materials. Literature indicates that greater CTE differences between materials allow for wider tunability [26,29,88,94]. Additionally, this material pair showed cracking near the interface, raising concerns about the structural integrity of the resulting metamaterials.

3.3. Potential applications

Due to the inherent thermal expansion of most materials, temperature variations result in thermal distortions and, consequently, thermomechanical stresses. These effects are particularly undesirable in components, devices, and systems that require high dimensional stability and fine precision, whilst being subjected to fluctuating temperatures. Therefore, metamaterials with controllable CTE are interesting for many engineering applications where temperature variations are extreme, dimensional accuracy is critical, or both. Compared to natural materials with low CTEs, metamaterials offer several advantages: (1) higher and tunable stiffness; (2) the possibility of being manufactured from materials with easier processability, thus increasing design freedom; (3) the ability for CTE to be tailored to a desired value through geometry and material manipulation; and (4) the potential to achieve low or even negative CTEs over wider temperature ranges [19,21,22,26,86].

Applications that benefit from ZTE metamaterials include engine and energy plant components, industrial machinery, and aircraft parts exposed to extreme thermal fluctuations. Biomedical engineering components (e.g., dental fillings) and microchips also benefit from such materials. Space and satellite components, which will be further detailed in this section, are also potential applications for ZTE metamaterials. Alongside ZTE, NTE metamaterials are valuable for compensating the PTE of surrounding materials in the same system. Furthermore, while many applications prioritize maintaining dimensional stability under temperature variations, others demand a specific deformation in response to temperature changes. For micro-electromechanical systems (MEMS), thermal adapters, and actuators, both NTE and PTE metamaterials are of great interest [19,21,25,28,30,79,85–87,94].

Space and satellite components, in particular, are exposed to severe temperature fluctuations in orbit, ranging from approximately -150°C to +150°C [83,111,112]. Additionally, these components must exhibit high stiffness and mechanical strength to withstand launch loads. For precision-critical systems such as satellite antennas, optical benches, mirrors, and adaptive connecting components, thermal distortions are highly undesirable. Thus, selecting materials capable of withstanding large temperature variations, maintaining low CTE, and enduring launch stresses poses a significant challenge [111,112].

Edeson, Aglietti, and Tatnall (2010) [113] listed commonly used materials in satellite components, including Invar, titanium alloys, aluminum alloys, fiber-reinforced composites, advanced ceramics, and glasses, evaluating them for use in optical benches. Although aluminum and titanium alloys exhibit good processability, low density for metals, and favorable mechanical properties, their high CTEs ($23.5x10^{-6}$/K and $8.6x10^{-6}$/K, respectively) make them unsuitable for dimensionally sensitive

applications. Despite its good processability and considerably low CTE (ranging from -0.5x10^{-6}/K to +2x10^{-6}/K, depending on the exact composition, processing history, and thermal treatment), Invar has a high density, and thus tends to be mainly used for stable joints, rather than for the whole optical bench. For these reasons, composites, ceramics, and glasses are often preferred due to their low density and low CTE. However, these materials also have limitations. Fiber-reinforced composites may suffer from thermal fatigue due to CTE mismatches between fiber and matrix. Ceramics and glasses, although possessing high stiffness, are brittle and prone to crack propagation. Furthermore, all these three classes of materials provide limited design freedom because of lower processability compared to metals [113].

Given these constraints, metamaterials with tunable or negative CTEs present a promising alternative for applications like optical benches. They can be tailored to achieve overall zero-CTE systems while maintaining the required stiffness and mechanical performance. Their lattice-based geometry results in lower density compared to bulk materials. Additionally, fabrication via MMAM eliminates the need for traditional joining methods. This simplification not only reduces the number of fabrication steps but also avoids the added weight and complexity associated with mechanical fasteners (bolts, screws, inserts), which require accessibility and specific geometries, thereby restricting design freedom and introducing the need to account for potential microslips at joints in structural modeling [113,114].

Toropova (2021) [112], Yu *et al*. (2023) [115], and Wei *et al*. (2016) [86] designed and simulated truss-like 3D structures based on stretching-dominated metamaterials (using the triangle principle), which typically offer higher stiffness than their bending-dominated counterparts, for satellite athermalization platforms. Holz *et al*. (2003) [116] constructed a conventionally manufactured NTE structure for a space optical bench and carried out several performance and space qualification tests. However, beyond this, tunable CTE metamaterials have not yet been tested in space.

Over the past two decades, the number of small satellite missions has risen significantly, driven by reduced costs and technical barriers. These missions provide opportunities to test novel space technologies and elevate the technology readiness level (TRL) of new components [117,118]. Metamaterials, not exclusively limited to tunable CTE applications, have been explored for various satellite functions [119–124]. Concurrently, interest in AM technologies for space components is growing, especially for integration into small satellites [114]. Nonetheless, due to the recent emergence of these manufacturing methods, research remains limited regarding the specific use of tunable CTE metamaterials produced via metal MMAM in satellite applications. While the studies based on metal MMAM in Table 2 [33,34,95] mention potential applications of their metamaterials in space, none of them had the primary objective of delivering a component for an actual satellite, and therefore did not further investigate the metamaterials in terms of performance. In this work, an NTE metamaterial fabricated via metal MMAM was developed to be tested for the first time in space.

3.4. Summary and present work

Chapters 2 and 3 presented the state-of-the-art in MMAM and metamaterials with tunable CTE, respectively. The central challenge in MMAM lies in achieving strong and reliable bonds between materials, by avoiding defects such as cracks, pores, and delamination. While the choice of material combinations is largely dictated by the desired functional properties of the final part, factors related

to the processability should also be considered. Ideally, the metals should be metallurgically compatible to reduce the risk of brittle intermetallic phase formation.

Mechanical metamaterials can exhibit a tunable CTE by combining two or more materials within specific lattice structures. MMAM technologies have significantly expanded the manufacturability of these metamaterials, though important challenges remain, particularly when targeting metallic 3D unit cell designs. Nonetheless, metal PBF-LB systems enable the fabrication of metamaterials with promising applications in satellite structures, where dimensional stability is critical. Despite these advances, due to the novelty of this technology, there remains a gap in research, specifically addressing the development and testing of tunable CTE metamaterials for satellite applications fabricated via metal MMAM.

In this work, both NTE and PTE metamaterials were fabricated via bi-metallic PBF-LB. CTE tunability was achieved by combining Invar and Inconel 718 in triangular 2.5D unit cells, following the triangle mechanism illustrated in Figure 6. Owing to the large CTE mismatch between these two alloys, the resulting metamaterials exhibit a wide range of thermal expansion values (see Figure 5). Moreover, the selected materials, which belong to the Fe-Ni system, are metallurgically compatible, thus satisfying both metallurgical and functional requirements.

In P{1}, different laser scanning strategies were applied to the vertical interfaces of Invar and Inconel 718. This enabled a novel investigation into how these strategies influence interfacial defects and material intermixing in material combinations that can be processed using identical parameters. Based on the insights obtained in this study, tunable-CTE metamaterials were subsequently fabricated using the selected strategy. These metamaterials, as shown in Table 2, were simulated, manufactured, and experimentally characterized to determine their CTEs.

In P{2}, the focus shifted to the influence of unit cell geometry on the resulting metamaterial CTE. Simulation results were compared with dilatometry measurements to validate the design approach.

In P{3}, greater emphasis was placed on the metamaterial’s target application: implementation in a satellite experiment. Accordingly, both the CTE and the structural integrity of the metamaterial were assessed, representing pioneering work toward space-qualified metamaterials with real-world application.

4. Materials and methods

The workflow of this thesis is depicted in Figure 9. This chapter provides a general overview of the materials and methods applied throughout the various experimental stages. Specific details of each stage, e.g., boundary conditions of FEM simulations, laser scanning strategies, programmed thermal cycle in the dilatometer, are described in each paper separately.

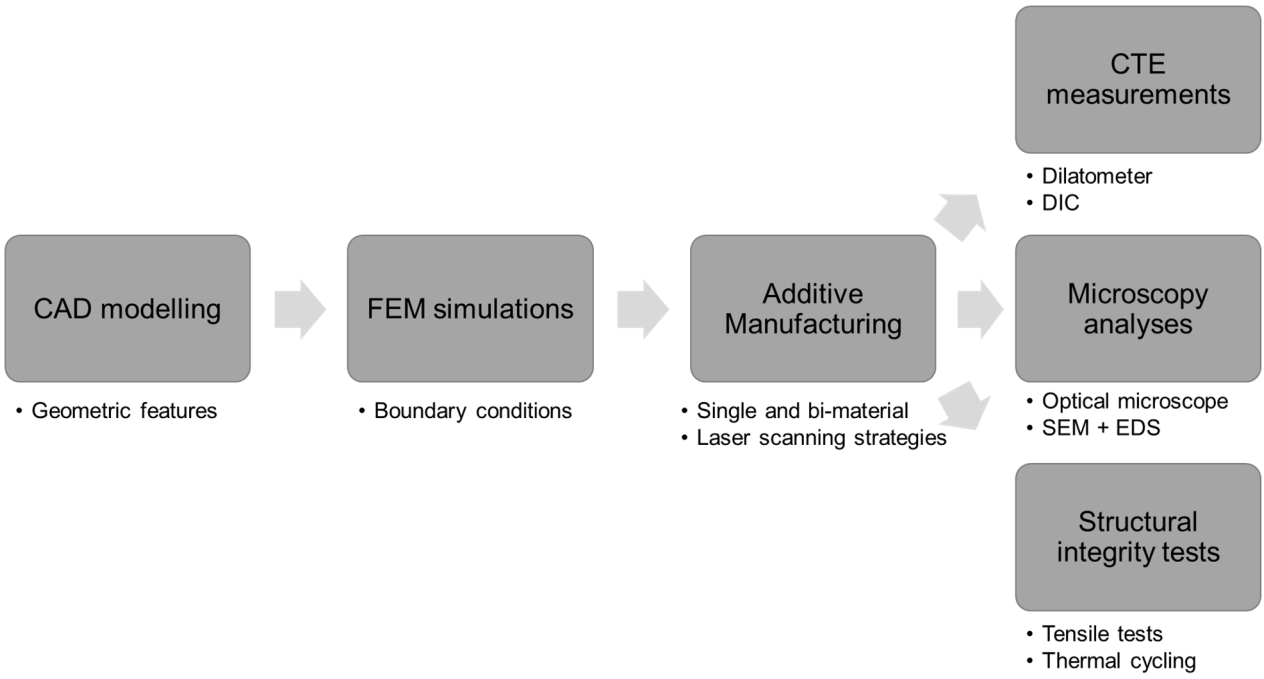


Figure 9 – Workflow of experiments in this thesis. The bullet points detail which features were studied or varied, or which tests were conducted in each experimental step.

4.1. CAD modelling of the metamaterials

While different metamaterial unit cells were explored during the early stages of this work, including unit cells that would present an NTE in two or three directions, this thesis focused on 1D structures resembling a triangle, thus following the triangle mechanism illustrated in Figure 6. For the CAD modelling of these structures, the CAD software Rhino 7 SR37 was used in combination with the Grasshopper extension. This extension enabled a fully parametric generation of unit cells, eliminating the need to manually model each geometry from scratch.

In Figure 10, the modelling workflow is outlined. In the Grasshopper extension (Figure 10a), key geometric parameters – including strut thickness, triangle height, base length, and an optional offset between the triangle's base and sides – were defined. Additional commands were implemented to generate the necessary point connections and apply mirroring operations, allowing arrays of triangular unit cells to be efficiently constructed. The resulting geometry was automatically transferred to the Rhino software (Figure 10b), where final manual refinements were performed, such as surface extrusions, filleted edges, and trimming operations. These adjustments led to the final CAD model of the triangular unit cell (Figure 10c).

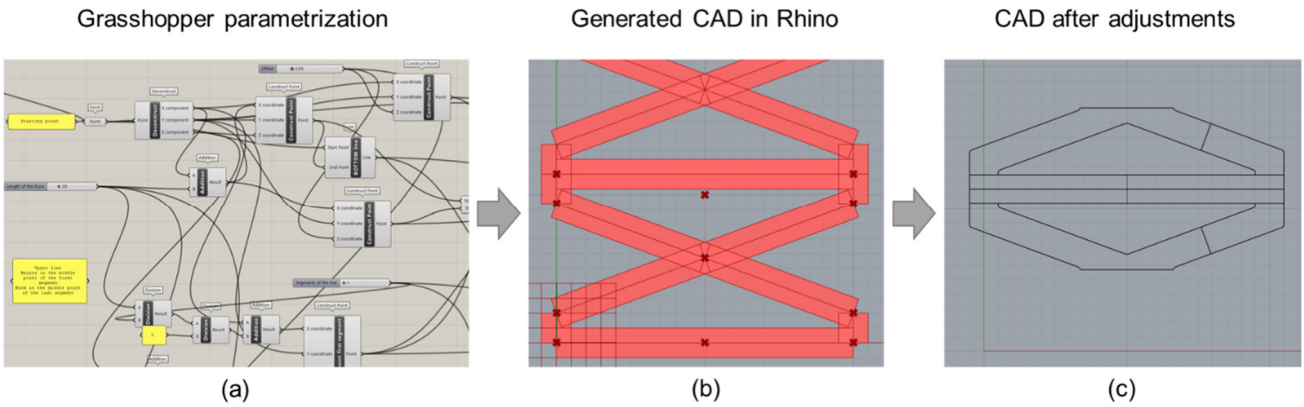


Figure 10 – Workflow of the modelling process for the unit cells and arrays. (a) In the Grasshopper extension (only a partial screenshot of the commands is shown), the geometric features, such as triangle height, were defined and commands were added to create lines between these points. (b) The commands in Grasshopper automatically generate a CAD model of the part in the Rhino software. (c) After manual adjustments, such as surface extrusions, addition of fillets edges and cuts, the CAD model of a triangular unit cell was complete.

The metamaterials modelled, simulated, and printed include single unit cells, matrices of combined unit cells (i.e., metamaterials), and an actuator aimed for a satellite experiment. Specific geometric features of the explored metamaterials and their unit cells are described in each paper separately.

4.2. Finite element method simulations

The structures were simulated in a fully elastic thermomechanical Finite Element Model implemented in the "Static Structural Module" of Ansys Workbench v2023 R2. The temperature-dependent Young's Modulus values of each material were kept as defined in the software database, and are given in Table 3. However, CTE values in the database were replaced by the measured temperature-dependent CTE values of the as-printed bulk materials. Further details of this values are given in P{2}. The boundary conditions applied to the unit cells of the metamaterials are further described in each paper separately.

Table 3 – Default temperature-dependent Young's Modulus values of each material found in the Ansys Workbench v2023 R2 database.

Invar		**Inconel 718**	
Temperature (°C)	**Young's Modulus (GPa)**	**Temperature (°C)**	**Young's Modulus (GPa)**
-260	126	21	165
-187	129	537	152
-114	133	815	110
-40	139	982	55
33	144	1093	34
106	149		
180	153		
253	156		
326	157		
400	155		

4.3. Sample manufacturing

The samples and metamaterials explored in this thesis were printed in an Aconity3D MIDI+ PBF-LB machine. Single material samples for parameter optimization were printed via the typical single material PBF-LB process, shown in the schematic in Figure 3. To print the bi-material samples, a selective powder deposition (SPD) recoater V1.0 developed by Schaeffler Aerosint was mounted within the machine. This system allows for 3D multi-material AM and uses the patterning drums methodology, as explained in section 2.3.1, and with advantages and limitations detailed in Table 1.

The SPD recoater, shown in Figure 11a, is equipped with two rotating drums, above which powder hoppers are installed. The drums are composed of a fine porous mesh, allowing a suction or ejection pressure to be applied and therefore powder particles to be either adhered to or blown from the drum, respectively. Each powder material is fed into the powder hoppers and, due to a negative pressure within the drums, the powder particles get adhered to the drums' surface, creating a layer of approximately 200 µm around the drums. Inside each drum, a line of small ejection tubes releases specific powder pixels from a line on the drum directly above the powder bed during deposition, using pressure supplied by inert Argon gas. This allows a bi-metallic powder bed to be deposited, as shown in the schematic in Figure 11b. To achieve the desired uniform layer thickness along the entire build platform, a leveler blade mounted on the right-hand side of drum 2 (not shown in Figure 11b) then removes the excess powder. Prior to each build job, alignment of the powder patterns of each material and their respective alignment with the laser beam are visually carried out. A detailed alignment procedure is described in P{1} .

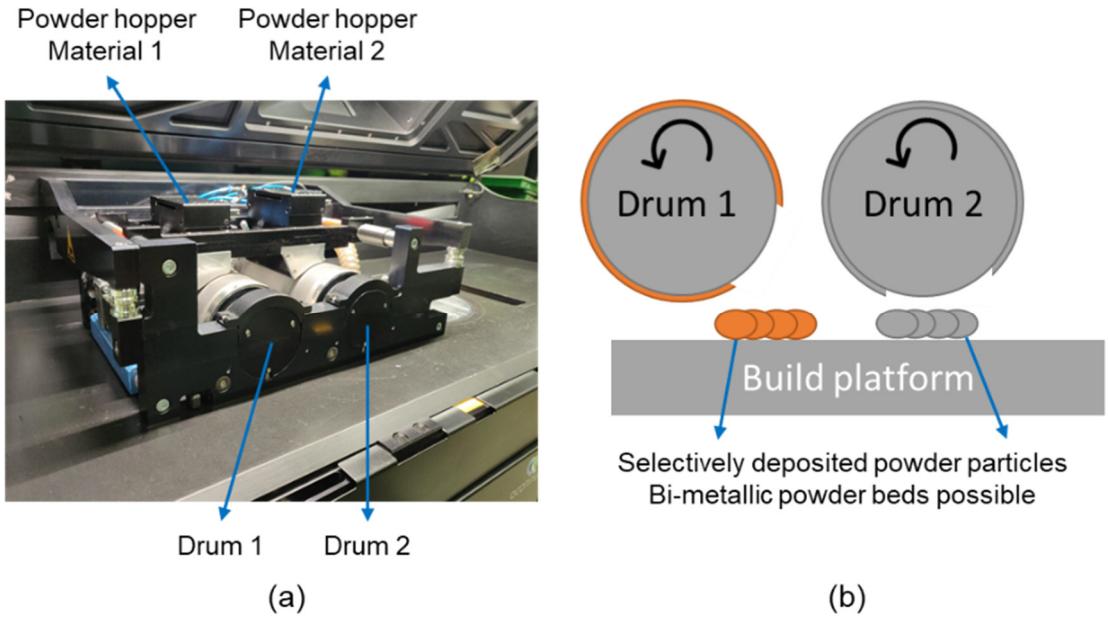


Figure 11 – (a) SPD recoater developed by Schaeffler Aerosint mounted in the Aconity3D MIDI+ PBF-LB machine. (b) Each drum deposits a different material onto the build platform within the same layer, enabling the formation of a 3D bi-metallic powder bed. Source: [66].

The deposition pixel size of 0.5×0.5 mm² defines the possible recoater resolution and restricts the minimum feature size of printed parts to ca. 1 mm. Nonetheless, some cross-contamination is expected at the powder pattern boundaries and, inevitably, some individual particles of one powder infiltrate into the deposited pattern of the other powder. This is evidenced in the energy dispersive spectroscopy (EDS) images in Figure 12. Loctite 496 superglue was dropped at a vertical interface powder pattern of Invar and Inconel 718 that had not been exposed by the laser. Green particles, rich in Fe, represent Invar powder particles, whereas pink particles, rich in Cr, represent Inconel 718 particles. The regions that were designed to be completely pure Invar and Inconel 718 patterns, i.e., Figure 12a and b, respectively, present some isolated foreign particles. The interface between Invar and Inconel 718 powder patterns, in Figure 12b, is easily recognized, although there is a range with higher cross-contamination directly at the interface.

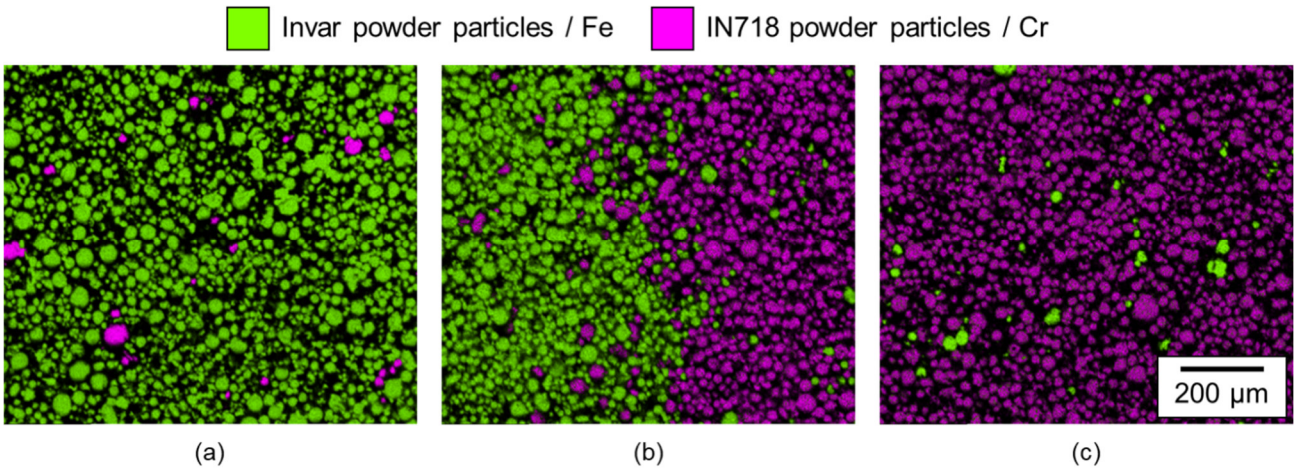


Figure 12 – EDS mappings of the powder patterns deposited by the SPD recoater. Green particles, rich in Fe, represent Invar powder particles, and pink particles, rich in Cr, represent Inconel 718 powder particles. Loctite 496 superglue was dropped onto powder patterns deposited by the SPD recoater: (a) Invar powder pattern; (b) vertical interface between Invar and Inconel 718 powder patterns; and (c) Inconel 718 powder pattern. The scale bar of 200 µm in (c) is the same for the images in (a) and (b).

Specific process parameters, which were chosen based on prior parameter optimization build jobs and laser scanning strategies are described in each appended paper separately. The printing process for the manufacture of both single-material and bi-material samples ran under an argon atmosphere, with a maximum O_2 content of 800 ppm.

4.3.1. Feedstock materials

In selecting suitable material combinations for the design of tunable CTE metamaterials, an initial screening was done across alloy systems that are both processable with PBF-LB and metallurgically compatible. The systems considered included Ti-Ti, Al-Al, Fe-Fe, Ni-Ni, and Fe-Ni alloys. Within each system, potential alloy combinations were evaluated based on the achievable difference in CTE, a key requirement to build NTE metamaterials. While most systems offered only moderate CTE variation between their alloys, the Fe-Fe and Fe-Ni systems contained the Invar alloy, which presents an exceptionally low CTE relative to other metals.

From these systems, two alloy combinations were considered initially: (1) Invar + 316L stainless steel and (2) Invar + Inconel 718. Subsequent parameter optimization studies for each alloy separately showed that only Invar + Inconel 718 could be printed using the same set of PBF-LB parameters. This compatibility reduces the porosity at the interface, according to the study in P{1}.

The Invar and Inconel 718 powders were provided by Linde, gas atomized and had particle size distributions ranging from 15 to 45 µm. The chemical composition of these powders according to the manufacturer is presented in Table 4.

Table 4 – Chemical composition of the powder feedstock materials used in this thesis, according to the supplier.

wt.%	Fe	Ni	Cr	Al	C	Mo	Nb	Ti	Co
Inconel 718	17.73	52.97	19.27	0.48	0.03	2.94	4.99	1.00	0.33
Invar	Balance	36.00	0.04	-	0.00	-	-	-	0.04

4.4. Microscopy analyses

Optical microscope images of this work of polished or etched samples were taken in a Zeiss Axiophot. For the metallography preparation, Invar + Inconel 718 samples were polished with a colloidal silica solution (“OP-S” by Struers) with 1% HCl added to it. The etchant used was a solution consisting of 75 ml ethanol + 25 ml HCl + 9 ml H_2O_2.

Scanning electron microscope (SEM) analyses were done in a Zeiss Ultra 55 SEM equipped with an EDAX Octane Elite EDS system. EDS mappings and line scans were performed to measure the elements' distribution at the bi-metallic interface.

4.5. CTE measurements

The CTE of the unit cells and metamaterials printed was measured either by dilatometry or by digital image correlation (DIC). The dilatometry measurements of this work were performed in a vertical pushrod dilatometer model L75 by Linseis (see Figure 13a), equipped with a low-temperature system that can be heated, as a usual furnace, as well as cooled, by using liquid nitrogen (N_2). The dilatometer can be operated with several measuring systems (i.e., sample measurement chambers), including one for samples with a diameter up to 30 mm (see Figure 13b), which allows the measurement of the unit cells and metamaterial matrices with a few combined unit cells. The length of the printed samples was measured with calipers prior to the thermal cycle.

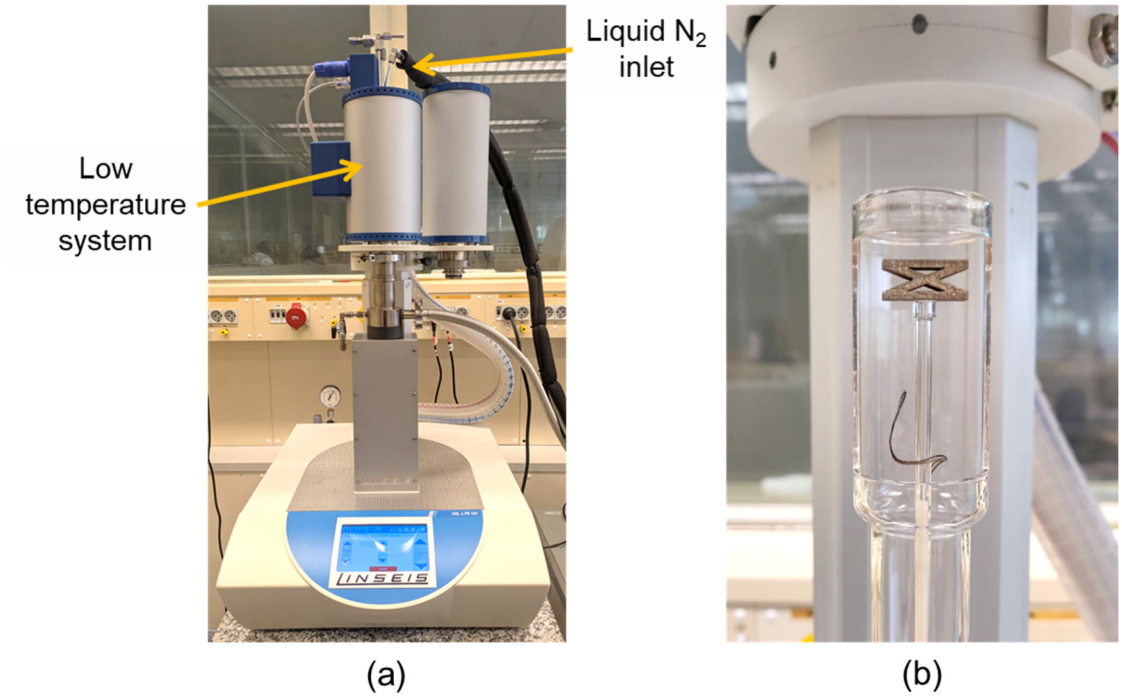


Figure 13 – (a) Linseis L75 vertical dilatometer used for the dilatometry measurements in this work. The low temperature system can be heated, as a usual furnace, as well as cooled, by using liquid N_2, whose inlet is indicated in the picture. (b) Unit cell placed in the ø30 mm measurement system.

Samples that could not fit into the dilatometer measuring system, i.e., large material matrices, had their CTE acquired by DIC. A two-dimensional displacement analysis was performed with a Q-400-2D Limess camera in combination with the software IstraD 4.4.6 from Dantec Dynamics.

Specifications of the programmed thermal cycles on the dilatometer and the DIC setup are described in each paper separately.

4.6. Structural integrity tests

Tensile tests and thermal cycling tests were performed to check the structural integrity of the printed metamaterials. Tensile tests were performed for single- and bi-material specimens in a servo-hydraulic testing machine from Schenck with a static loading capacity of 10kN, controlled by Doli Test&Motion software version 5.5.3.0. The elongation values were taken from the machine crosshead, since no extensometer was attached to the specimens. The Young's modulus of the printed materials was determined by measuring the ultrasonic velocity of longitudinal and shear waves in the bulk material at room temperature, following the procedure described in [125]. For these measurements, two cubes (10x10x10 mm^3) of each material were printed, had their top and bottom surfaces polished, and their density measured by the Archimedes method. The ultrasound echoes were acquired by Schenck ultrasonic transducers model *tri CF-SW* (shear waves) and model *harisonic ABM-0504* (longitudinal waves), both working at a frequency of 5MHz. The echoes were assessed in a ScanMaster's software version 3.5o.

The printed unit cells were thermally cycled in a Voetsch VT3 7006 S2 furnace that cyclically transfers the samples from a hot chamber to a cold chamber. The hot chamber temperature was set to +200 °C while the cold chamber was set to -70 °C, resulting in a temperature span of 270

°C, which is the same temperature span predicted during the satellite experiment (from -120 °C to +150 °C).

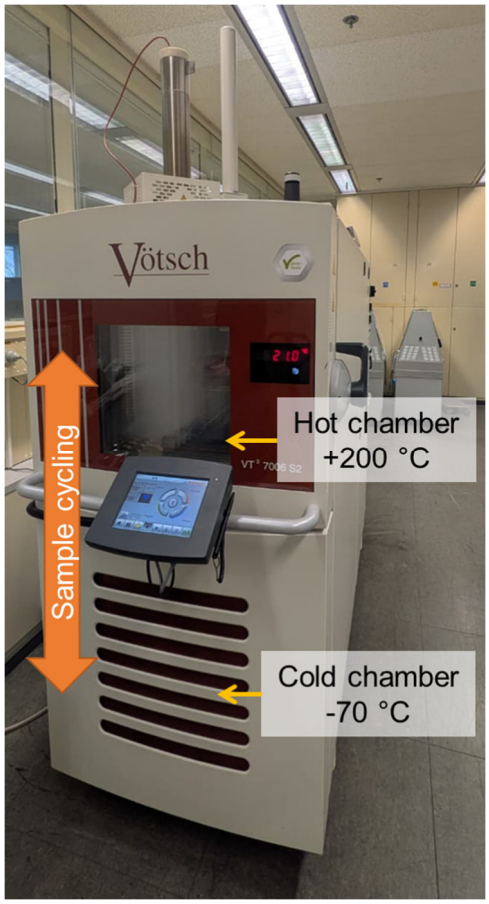


Figure 14 – Voetsch VT3 7006 S2 furnace used for thermal cycling tests.

5. Results and publications

In this thesis, investigations were carried out on tunable CTE metamaterials fabricated via bi-metallic PBF-LB, with the focus on an NTE metamaterial for a satellite experiment. Three peer-reviewed journal papers were written and attached in this thesis, each addressing a specific step in the NTE metamaterial development. The peer-reviewed papers that will be summarized in this chapter are listed below:

P{1} Prestes, I.B., Jägle, E.A.

Influence of the laser strategy on bi-metallic interfaces printed via multi-material laser-based powder bed fusion

Additive Manufacturing Letters 13 (2025) 100274

DOI: 10.1016/j.addlet.2025.100274

P{2} Prestes, I.B., Buchmann, E., Höfer, P., Jägle E.A.

Prediction of the negative thermal expansion behavior of metallic metamaterials printed via bi-material laser-based powder bed fusion

Materials & Design 256 (2025) 114276

DOI: 10.1016/j.matdes.2025.114276

P{3} Prestes, I.B., Rottler, J., Jägle E.A.

Towards space application of a mechanical metamaterial fabricated via bi-metallic additive manufacturing to guarantee dimensional accuracy

Submitted to Smart Materials and Structures.

Further publications and conference contributions with related topics, which are not part of this thesis, but emerged during this period are listed below:

Peer-reviewed journal contributions

Buchmann, E., Prestes, I.B., Jägle, E.A., Höfer, P. Athermalization of space instruments with mechanical metamaterials: structural instrument architectures and conceptual design of an in-orbit demonstration experiment. CEAS Space J (2025). https://doi.org/10.1007/s12567-025-00631-w

Conference papers

Prestes, I.B., Buchmann, E., Höfer, P., Jägle, E.A. (2025) Space application of a mechanical metamaterial fabricated via bi-metallic additive manufacturing for dimensional stability. Paper ID: 95108. In: IAC 2025 congress proceedings, 76th International Astronautical Congress (IAC), Sydney, Australia

Buchmann, E., Prestes, I.B., Musil, B., Höfer, P. (2023). Design and Investigation of a Thermoelastic Actuator with Tailored Unidirectional Thermal Expansion and Stiffness using Mechanical Metamaterials and Joule Heating Activation. In: Rieser, J., Endress, F., Horoschenkoff, A., Höfer, P., Dickhut, T., Zimmermann, M. (eds) Proceedings of the Munich Symposium on Lightweight Design 2022. MSLD 2022. Springer Vieweg, Cham. https://doi.org/10.1007/978-3-031-33758-1_1

Conference presentations

Prestes, I.B. Metallic metamaterials with tunable coefficient of thermal expansion produced via multi-material PBF-LB. Alloys for Additive Manufacturing Symposium (AAMS) 2025: Neuchâtel, Switzerland.

Prestes, I.B. Negative thermal expansion behavior of metallic metamaterials produced via multi-material L-PBF. International Conference on Advanced Computational Engineering and Experimenting (ACEX) 2024: Barcelona, Spain.

Prestes, I.B. Negative thermal expansion behavior of metallic metamaterials produced via multi-material L-PBF. The Minerals, Metals & Materials Society (TMS) 2024: Orlando, USA.

Prestes, I.B. Negative thermal expansion behavior of metallic metamaterials produced via multi-material L-PBF. Alloys for Additive Manufacturing Symposium (AAMS) 2023: Madrid, Spain.

Prestes, I.B. Metal multi-material Additive Manufacturing of metamaterials with negative CTE. Materials Science and Technology in Europe (FEMS Euromat) 2023: Frankfurt, Germany.

Conference poster

Prestes. I.B. Metal multi-material Additive Manufacturing of metamaterials with negative coefficient of thermal expansion (CTE). Alloys for Additive Manufacturing Symposium (AAMS) 2022: Neubiberg, Germany. (Best poster award)

5.1. Publication {1}: The bi-material PBF-LB process

This publication presents an investigation of the bi-material PBF-LB process that was used to print the NTE metamaterials reported in the subsequent works. Different laser scanning strategies were applied in cuboids with vertical interfaces between Invar and Inconel 718, which was the material combination selected for the NTE metamaterials. Unlike many published studies in MMAM involving dissimilar alloys, Invar and Inconel 718 can be printed using the same PBF-LB parameters. This enabled the application of the single scan strategy, in which both materials are printed simultaneously without interrupting the scan vectors at the interface. In contrast, double scan was the term used to define the laser scanning strategy in which one material was printed first, with scan vectors ending exactly at the material interface, and the second material was printed subsequently. In addition to comparing these two strategies, the effects of other parameters were studied: angle increment per layer (45° vs. 67°) and the application of a remelt procedure at the interface.

The material interfaces were characterized using optical microscopy, and EDS mappings and line scans. The single scan strategy led to a jagged mixing pattern at the interface, whose periodicity is governed by the angle increment per layer. The element mixing is attributed to the melt pool, which drags the material from one side into the adjacent one. On the other hand, the application of the double scan significantly reduced the material mixing at the interface. A quantitative analysis of the material mixture was done by normalizing element counts of Fe across EDS line scans and fitting the sigmoid function of Boltzmann to the data. The steepness of the fitted curves was used to assess the width of the intermixing zone. While the remelt strategy seems to have broadened this zone, its influence was not consistent across the observed samples. Hatch angle increment per layer had no significant influence on the width of the intermixing zone. On the other hand, the single scan strategy led to considerably broader mixing zone compared to the double scan strategy. When combining two highly dissimilar metals, such intermixing may be detrimental, potentially leading to the formation of brittle intermetallic phases. However, as both Invar and Inconel 718 are FCC alloys with similar chemical compositions, the observed material mixture did not introduce defects and detrimental phases, thus achieving a sound metallurgical bond.

Porosity and cracks at the material interface were observed at the material interface in samples printed using the double scan strategy, but were not found in those printed with the single scan. The application of a remelt at the interface was able to only partially heal these defects. While the exact cause of the pores could not be definitively identified, potential contributing factors include: (1) powder denudation at the interface when printing the first material; (2) surface irregularities of the printed part, shielding neighboring powder from laser exposure or reducing the wettability of the molten powder; and (3) gaps between the deposited powder patterns that could not be entirely filled by the melt pool, since the scan vectors abruptly stop at the materials' interface. The cracks, which were consistently observed near pores, may have originated from a localized overheating or insufficient molten material to fill the pores from previously deposited layers.

The study has shown that different laser strategies in vertical interfaces play an important role in the quality of and magnitude of material intermixing in parts printed by bi-metallic PBF-LB. The choice of the strategy should be made considering the final application of the printed part. Based on these findings, the single scan strategy was adopted for fabricating the NTE metamaterials described in this thesis, as it provided dense, defect-free interfaces. To maintain process simplicity

and since no clear benefit was observed from other variables, a 67° angle increment per layer without remelt was applied for the subsequent printed parts.

5.2. Publication {2}: The principle behind NTE metamaterials

In this publication, unit cells and multi-unit-cell segments of NTE metamaterials were fabricated using the bi-metallic PBF-LB process and the material combination investigated in P{1} . The CTE of the printed structures, based on the triangle mechanism illustrated in Figure 6, was predicted via FEM simulations and validated by dilatometry measurements. The main objective of this study was to demonstrate the manufacturability of NTE metamaterials by metallic MMAM and to evaluate their thermal behavior under conditions relevant to space applications.

This work enabled the analysis of (1) how the geometric features of the metamaterials influence their measured CTE, and (2) which boundary conditions must be applied in the FEM simulations to reliably predict the NTE behavior of the printed structures. These insights establish how NTE metamaterials should be designed and fabricated to achieve reproducible and predictable CTE measurements.

Initially, various geometric parameters of the triangular NTE metamaterial were modified to assess their influence on the CTE. The FEM simulations were performed using two approaches: with periodic boundary conditions (PBC), representing an infinite array of unit cells; and without PBC, simulating an isolated unit cell free to deform. Based on these initial simulation results, five representative geometries were selected for fabrication and experimental CTE measurement via dilatometry. Two types of unit cells of each geometry were analyzed – X- and triangle-unit cell – depending on the selected segment of the metamaterial structure.

The results have shown that hinge stiffness, governed by geometric parameters, significantly impacts the resulting CTE. To achieve very negative CTE values, the hinge stiffness should be minimized. Dilatometry CTE curves for both X- and triangle-unit cells exhibited characteristic “jumps”, which were observed in and predicted by the simulations. The jumps were attributed to a bulging effect on the top and bottom surfaces of unit cells when they are not surrounded by others. However, the triangle-unit cells showed more consistent and reproducible measurements and better agreement with simulation results.

While FEM simulations of single unit cells could reliably predict the NTE behavior of printed samples, they were insufficient to capture the full metamaterial response. Therefore, multi-unit-cell structures arranged in 2×1 and 2×2 unit cell matrix configurations were printed and tested. It was observed that increasing the number of connected unit cells reduced the bulging effect and brought the measured CTE closer to the predicted values for the full metamaterial.

This study successfully demonstrated the fabrication of NTE metamaterials composed of Invar and Inconel 718 using a bi-metallic PBF-LB process. A reliable prediction of the CTE requires appropriate boundary conditions to be used in the simulations and the selection of a representative metamaterial segment. Beyond validating the NTE concept for the intended satellite experiment, the findings contribute to a better understanding of how these structures behave thermally across the temperatures expected in their application.

5.3. Publication {3}: The application in a satellite experiment

Since the microstructure and the thermal behavior of NTE metamaterials fabricated via bi-metallic PBF-LB were characterized in the previous publications, the focus of this publication shifted to exploring their suitability for their intended application: a satellite experiment. The objectives of this publication were: (1) to evaluate the structural integrity of metamaterials made of Invar and Inconel 718 fabricated via bi-metallic PBF-LB; and (2) to further investigate the influence of additional unit cells and extra geometrical features – designed for active heating – on the CTE of the metamaterials.

Beyond what was explored in P{2} , this study examines not only metamaterials with tunable negative CTE, but also those with tunable positive CTE. This behavior can be achieved by inverting the material assignment within the triangular unit cell design. Metamaterials with positive CTE are of particular interest for use as actuators in space applications. In this study, these unit cells were also combined with negative CTE counterparts to result in a stable CTE across the operational temperature range, even above the Curie temperature of Invar. This is desirable because the metamaterials are designed to compensate for the positive thermal expansion of surrounding materials, which typically exhibit a relatively constant CTE over a wide temperature range. Additionally, the combination of positive and negative CTE unit cells extends the achievable range of tunable CTE values beyond what either type could provide individually.

To support active thermal control in the metamaterial for the satellite experiment, an additional trapezoidal geometry was incorporated into the unit cells to accommodate a heating element. To assess the impact of this added geometry on CTE behavior, both negative and positive CTE unit cells were simulated and fabricated with the trapezoid extension. While a slight effect on the CTE was predicted and observed, it was inconsistent and considered negligible.

In the previous work P{2}, it was shown that increasing the number of unit cells improved agreement between measured and simulated CTE values, though the measurements remained lower than predicted. In P{3} , larger unit cell matrices (4×1 and 10×5) were printed to better match the simulation results. The 4×1 matrix further approached the simulated CTE curve, but only the 10×5 matrix fully matched the predicted values.

Finally, the structural integrity of the metamaterials was assessed by tensile testing and thermal cycling. Bi-metallic tensile specimens consistently failed in the weaker material (Invar) rather than at the material interface, supporting earlier EDS results from P{1}, which indicated strong metallurgical bonding. For thermal cycling, unit cells were subjected to 500 cycles over the temperature span expected in the satellite experiment. Inspection under an optical microscope revealed no cracks or visible plastic deformation in the hinge regions, where the stresses were the highest according to the FEM simulations.

In summary, this publication has shown the feasibility and robustness of tunable CTE metamaterials fabricated via bi-metallic PBF-LB for space applications.

6. Conclusions and future work

This thesis has presented a comprehensive investigation of NTE metamaterials fabricated via bi-metallic PBF-LB, from their manufacturing process to their applicability in space components. The MMAM technique employed in this work is novel; thus, the fabrication of such metamaterials was only recently enabled. Consequently, the literature in this specific area is still limited. This work has contributed to the field of metallic MMAM and identified a potential application in space systems. This chapter summarizes the main conclusions drawn from each publication with the intent of providing a foundation and reference point for future research and development in this field.

P{1} - The bi-metallic PBF-LB process

- In multi-material PBF-LB, the parameter study goes beyond finding optimal PBF-LB parameters for each material individually, as the laser scanning strategies at bi-metallic interfaces determine whether they will be defect-free or not.
- Interfacial porosity is more prone to happen with the double scan strategy, in which each material is exposed to the laser separately. Consequently, cracks may arise due to overheating. While remelting can partially heal these defects, it does not ensure a fully sound interface.
- Single scan strategies are more robust against porosity caused by eventual powder pattern gaps at the interface. However, this approach require both materials to share the same set of PBF-LB parameters.
- Metallurgical compatibility is essential when using a single scan approach, as this scanning strategy generates a wide (up to 1 mm) intermixing zone, which, depending on the material combination, could potentially form brittle intermetallic phases.
- Invar and Inconel 718 interfaces fabricated using the single scan strategy exhibited good metallurgical bond and defect-free interfaces. Variation in angle increment per layer had no effect on the interface quality or on the intermixing intensity, although the regularity of the “jagged” interface patterns could be influenced (more regular with 45° and more randomized with 67°).
- For manufacturing NTE metamaterials for space applications, where defect-free interfaces are essential, the single scan strategy is preferred. Parameters such as angle increment per layer and remelt at the interface have minimal influence on the intermixing width and can thus be chosen based on other considerations.

P{2} – The principle behind NTE metamaterials

- NTE metamaterials based on the triangle mechanism were successfully printed via bi-metallic PBF-LB. Their experimentally measured negative CTEs closely matched FEM simulation predictions, depending on the applied boundary conditions and on which segment of the metamaterial was printed.
- FEM simulations without periodic boundary conditions reliably predicted the CTE of single triangle-unit cells. Simulations with periodic boundary conditions represented the behavior of a full metamaterial composed of unit cell arrays more accurately.
- The geometry of the unit cells strongly influences the CTE. Therefore, CTE values can be tuned within a defined range depending on the material combination used.
- Hinge stiffness plays a key role in defining metamaterial CTE. Reducing wall thickness and introducing an offset between the triangle base and sides increases the hinge compliance,

resulting in a more negative CTE. However, excessively low angles ($\theta < 20°$) increase the hinge mass due to the accumulation of bulk material around it. This increased mass reduces the hinge's compliance and inhibits the expected rotational motion of the triangle sides, ultimately counteracting the mechanism behind the negative thermal expansion. As a result, a minimum CTE value is reached, beyond which further reductions in angle no longer produce more negative CTEs. While a reduction of wall thickness could help reduce the mass around the hinge, process limitations such as resolution and minimum printable feature size constrain this reduction.

- Single unit cells or small unit cell arrays behave differently from larger metamaterial structures. Single unit cells are prone to a bulging effect at their top and bottom surfaces, which reduces the measured CTE and causes "jumps" in the measured and simulated CTE curves.
- Adding more unit cells to an NTE structure – e.g., in 2×1 and 2×2 matrices of unit cells – reduces the bulging effect and leads to CTE curves more representative of a complete metamaterial, without abrupt jumps.

P{3} – The application in a satellite experiment

- The further addition of unit cells in the structure eventually led to CTE values that matched the FEM simulations with periodic boundary conditions. This supports the expected behavior of the metamaterial printed for the satellite experiment, where constraints from surrounding unit cells and fixing structures suppress the bulging effect.
- The integration of additional geometries for active heating did not significantly or consistently alter the CTE of single unit cells, supporting the predictability of the metamaterial's overall thermal behavior.
- The Invar and Inconel 718 material combination was also suitable for tuning positive CTEs by inverting the material assignment within the unit cell. As with the NTE metamaterials, the geometry of the unit cells allowed tuning within a defined CTE range.
- By combining positive and negative CTE unit cells, metamaterials can be designed with a near-zero or more stable CTE curve over a broader temperature range. This is particularly useful when compensating for thermal expansion in adjacent structures made of natural materials, which usually present a positive and rather constant CTE curve.
- From a structural integrity perspective, the metamaterial demonstrated promising performance, indicating its suitability for application in space environments, where reliability under thermal cycling and structural loads is critical. Tensile tests in bi-metallic samples consistently failed in the weakest material (Invar), confirming that the interface was metallurgically sound. No failures or deformations were observed after thermal cycling within the expected temperature span of the satellite mission.

The PhD thesis concluded with the successful demonstration of a reliable NTE metamaterial – both thermally and mechanically – for use in space systems. Nevertheless, several open questions and directions have emerged, as outlined below:

- The extent of material intermixing at vertical interfaces is influenced by melt pool characteristics. Although this aspect was not critical for the current application and material combination, it may require stricter control in other cases. Future work should explore

strategies such as varying scanning speed, on-the-fly parameter change, laser wobble, defocused beam, and pulsed laser to tailor the intermixing width and intensity.

- To broaden the tunable CTE range, other material combinations should be investigated, prioritizing those compatible with single scan strategy printing. Alternatives to Invar may be sought to work around its CTE increase above its Curie temperature, which compromises the stability of the metamaterial's CTE curves. Additionally, if an improved bonding is necessary for new material combinations, alternative powder pattern interface designs can be considered, such as interlocking or zig-zag.
- Material distributions within unit cells can be modified to improve stress distribution, particularly at triangle hinges, or to further tailor the CTE. Geometric variations – such as curvature, local thickening, or thinning – may also aid in fine-tuning mechanical and thermal responses.
- The current triangle CTE unit cells allow CTE tuning in only one direction. Using the same material combination, structures enabling 2D or 3D CTE tuning could be developed. This would also open the possibility for tuning additional properties, like Poisson's ratio.
- Advances in the pattern drums technique now allow the deposition of up to three materials. This enables interesting new possibilities, such as:
    - Incorporating an intermediate-CTE material between Invar and Inconel 718 to reduce stress at hinges.
    - Using an intermediate buffer layer to bond highly dissimilar metals in NTE metamaterials.
    - Fabricating removable support structures within 3D unit cells by using a third, sacrificial material.

In conclusion, this work provides a detailed experimental and analytical basis for future research into tunable CTE metamaterials fabricated via metallic MMAM. The findings can support future investigations focused on material combination selection, optimization of scanning strategies for robust bi-metallic bonding, and the design of metamaterials for thermomechanical stability in space and other temperature-critical applications.

References

[1] I. Gibson, D. Rosen, B. Stucker, Additive Manufacturing Technologies, Springer New York, New York, NY, 2015.

[2] D. Herzog, V. Seyda, E. Wycisk, C. Emmelmann, Additive manufacturing of metals, Acta Materialia 117 (2016) 371–392. https://doi.org/10.1016/j.actamat.2016.07.019.

[3] S. Asapu, Y. Ravi Kumar, Design for Additive Manufacturing (DfAM): A Comprehensive Review with Case Study Insights, JOM 77 (2025) 3931–3951. https://doi.org/10.1007/s11837-025-07164-x.

[4] P. Badoniya, M. Srivastava, P.K. Jain, S. Rathee, A state-of-the-art review on metal additive manufacturing: milestones, trends, challenges and perspectives, J Braz. Soc. Mech. Sci. Eng. 46 (2024). https://doi.org/10.1007/s40430-024-04917-8.

[5] A.W. Gebisa, H.G. Lemu, A case study on topology optimized design for additive manufacturing, IOP Conf. Ser.: Mater. Sci. Eng. 276 (2017) 12026. https://doi.org/10.1088/1757-899X/276/1/012026.

[6] A. Bandyopadhyay, B. Heer, Additive manufacturing of multi-material structures, Materials Science and Engineering: R: Reports 129 (2018) 1–16. https://doi.org/10.1016/j.mser.2018.04.001.

[7] Di Wang, L. Liu, G. Deng, C. Deng, Y. Bai, Y. Yang, W. Wu, J. Chen, Y. Liu, Y. Wang, X. Lin, C. Han, Recent progress on additive manufacturing of multi-material structures with laser powder bed fusion, Virtual and Physical Prototyping 17 (2022) 329–365. https://doi.org/10.1080/17452759.2022.2028343.

[8] M. Vaezi, S. Chianrabutra, B. Mellor, S. Yang, Multiple material additive manufacturing – Part 1: a review, Virtual and Physical Prototyping 8 (2013) 19–50. https://doi.org/10.1080/17452759.2013.778175.

[9] A. Nazir, O. Gokcekaya, K. Md Masum Billah, O. Ertugrul, J. Jiang, J. Sun, S. Hussain, Multi-material additive manufacturing: A systematic review of design, properties, applications, challenges, and 3D printing of materials and cellular metamaterials, Materials & Design 226 (2023) 111661. https://doi.org/10.1016/j.matdes.2023.111661.

[10] A. Mussatto, Research progress in multi-material laser-powder bed fusion additive manufacturing: A review of the state-of-the-art techniques for depositing multiple powders with spatial selectivity in a single layer, Results in Engineering 16 (2022) 100769. https://doi.org/10.1016/j.rineng.2022.100769.

[11] X. Wu, H. Yan, Y. Zhou, P. Zhang, Q. Lu, H. Shi, Review of additive manufactured metallic metamaterials: Design, fabrication, property and application, Optics & Laser Technology 182 (2025) 112066. https://doi.org/10.1016/j.optlastec.2024.112066.

[12] A. Álvarez-Trejo, E. Cuan-Urquizo, D. Bhate, A. Roman-Flores, Mechanical metamaterials with topologies based on curved elements: An overview of design, additive manufacturing and mechanical properties, Materials & Design 233 (2023) 112190. https://doi.org/10.1016/j.matdes.2023.112190.

[13] B. McDonnell, V. Errico, P. Posa, A. Angelastro, A. Furman, E. O'Hara, S.L. Campanelli, N. Harrison, Bi-metallic lattice structures manufactured via an intralayer multi-material powder bed fusion method, Additive Manufacturing 89 (2024) 104301. https://doi.org/10.1016/j.addma.2024.104301.

[14] A. Engel, O. Al-Ketan, A. Jung, 2025. Multimaterial Approach to Improve the Mechanical Properties of a Novel Modified Auxetic Reentrant Honeycomb Structure. Adv Eng Mater 27, 2500332. https://doi.org/10.1002/adem.202500332.
[15] Q. Zhang, Y. Sun, A series of auxetic metamaterials with negative thermal expansion based on L-shaped microstructures, Thin-Walled Structures 197 (2024) 111596. https://doi.org/10.1016/j.tws.2024.111596.
[16] J.N. Grima, D. Attard, R. Gatt, Truss-type systems exhibiting negative compressibility, Phys. Status Solidi B 245 (2008) 2405–2414. https://doi.org/10.1002/pssb.200880267.
[17] H. Xu, A. Farag, D. Pasini, Routes to program thermal expansion in three-dimensional lattice metamaterials built from tetrahedral building blocks, Journal of the Mechanics and Physics of Solids 117 (2018) 54–87. https://doi.org/10.1016/j.jmps.2018.04.012.
[18] Q. Zhang, Y. Sun, Novel metamaterial structures with negative thermal expansion and tunable mechanical properties, International Journal of Mechanical Sciences 261 (2024) 108692. https://doi.org/10.1016/j.ijmecsci.2023.108692.
[19] Y.C. Zhang, Y.J. Liang, S.T. Liu, Y.D. Su, A new design of dual-constituent triangular lattice metamaterial with unbounded thermal expansion, Acta Mech. Sin. 35 (2019) 507–517. https://doi.org/10.1007/s10409-018-0811-y.
[20] R. Lakes, Cellular solid structures with unbounded thermal expansion, J Mater Sci Lett 15 (1996) 475–477. https://doi.org/10.1007/BF00275406.
[21] G. Jefferson, T.A. Parthasarathy, R.J. Kerans, Tailorable thermal expansion hybrid structures, International Journal of Solids and Structures 46 (2009) 2372–2387. https://doi.org/10.1016/j.ijsolstr.2009.01.023.
[22] L. Ai, X.-L. Gao, Three-dimensional metamaterials with a negative Poisson's ratio and a non-positive coefficient of thermal expansion, International Journal of Mechanical Sciences 135 (2018) 101–113. https://doi.org/10.1016/j.ijmecsci.2017.10.042.
[23] Q. Wang, J.A. Jackson, Q. Ge, J.B. Hopkins, C.M. Spadaccini, N.X. Fang, Lightweight Mechanical Metamaterials with Tunable Negative Thermal Expansion, Phys. Rev. Lett. 117 (2016) 175901. https://doi.org/10.1103/PhysRevLett.117.175901.
[24] L. Wu, B. Li, J. Zhou, Isotropic Negative Thermal Expansion Metamaterials, ACS Appl. Mater. Interfaces 8 (2016) 17721–17727. https://doi.org/10.1021/acsami.6b05717.
[25] J. Lehman, R. Lakes, Stiff, strong zero thermal expansion lattices via the Poisson effect, J. Mater. Res. 28 (2013) 2499–2508. https://doi.org/10.1557/jmr.2013.154.
[26] W. Miller, D.S. Mackenzie, C.W. Smith, K.E. Evans, A generalised scale-independent mechanism for tailoring of thermal expansivity: Positive and negative, Mechanics of Materials 40 (2008) 351–361. https://doi.org/10.1016/j.mechmat.2007.09.004.
[27] O. Sigmund, S. Torquato, Composites with extremal thermal expansion coefficients, Appl. Phys. Lett. 69 (1996) 3203–3205. https://doi.org/10.1063/1.117961.
[28] C.S. Ha, E. Hestekin, J. Li, M.E. Plesha, R.S. Lakes, Controllable thermal expansion of large magnitude in chiral negative Poisson's ratio lattices, Phys. Status Solidi B 252 (2015) 1431–1434. https://doi.org/10.1002/pssb.201552158.
[29] E. Gdoutos, A.A. Shapiro, C. Daraio, Thin and Thermally Stable Periodic Metastructures, Exp Mech 53 (2013) 1735–1742. https://doi.org/10.1007/s11340-013-9748-z.
[30] K. Wei, Y. Peng, W. Wen, Y. Pei, D. Fang, 2017. Tailorable Thermal Expansion of Lightweight and Robust Dual-Constituent Triangular Lattice Material. Journal of Applied Mechanics 84, 101006. https://doi.org/10.1115/1.4037589.

[31] J. Qu, M. Kadic, A. Naber, M. Wegener, Micro-Structured Two-Component 3D Metamaterials with Negative Thermal-Expansion Coefficient from Positive Constituents, Sci. Rep. 7 (2017) 40643. https://doi.org/10.1038/srep40643.
[32] A. Takezawa, M. Kobashi, Design methodology for porous composites with tunable thermal expansion produced by multi-material topology optimization and additive manufacturing, Composites Part B: Engineering 131 (2017) 21–29. https://doi.org/10.1016/j.compositesb.2017.07.054.
[33] M. Bambach, M.R. Tucker, Laser powder bed fusion of planar bi-metallic thermally auxetic lattice structures, CIRP Annals (2024). https://doi.org/10.1016/j.cirp.2024.04.023.
[34] O. Červinek, M.R. Tucker, D. Koutný, M. Bambach, 2024. Computational and experimental investigation of thermally auxetic multi-metal lattice structures produced by laser powder bed fusion. Virtual and Physical Prototyping 19, e2396069. https://doi.org/10.1080/17452759.2024.2396069.
[35] I.B. Prestes, E. Buchmann, P. Höfer, E.A. Jägle, Prediction of the negative thermal expansion behavior of metallic metamaterials printed via bi-material laser-based powder bed fusion, Materials & Design 256 (2025) 114276. https://doi.org/10.1016/j.matdes.2025.114276.
[36] B. Neirinck, X. Li, M. Hick, Powder Deposition Systems Used in Powder Bed-Based Multimetal Additive Manufacturing, Acc. Mater. Res. 2 (2021) 387–393. https://doi.org/10.1021/accountsmr.1c00030.
[37] ISO/ASTM, ISO/ASTM 52900:2021) - Additive Fertigung: Grundlagen - Terminologie, DIN Deutsches Institut für Normung, Berlin, 2022.
[38] X. Zheng, C. Williams, C.M. Spadaccini, K. Shea, Perspectives on multi-material additive manufacturing, Journal of Materials Research 36 (2021) 3549–3557. https://doi.org/10.1557/s43578-021-00388-y.
[39] D. Han, H. Lee, Recent advances in multi-material additive manufacturing: methods and applications, Current Opinion in Chemical Engineering 28 (2020) 158–166. https://doi.org/10.1016/j.coche.2020.03.004.
[40] T.D. Ngo, A. Kashani, G. Imbalzano, K.T. Nguyen, D. Hui, Additive manufacturing (3D printing): A review of materials, methods, applications and challenges, Composites Part B: Engineering 143 (2018) 172–196. https://doi.org/10.1016/j.compositesb.2018.02.012.
[41] I.H. ZainElabdeen, L. Ismail, O.F. Mohamed, K.A. Khan, A. Schiffer, Recent advancements in hybrid additive manufacturing of similar and dissimilar metals via laser powder bed fusion, Materials Science and Engineering: A 909 (2024) 146833. https://doi.org/10.1016/j.msea.2024.146833.
[42] D.D. Gu, W. Meiners, K. Wissenbach, R. Poprawe, Laser additive manufacturing of metallic components: materials, processes and mechanisms, International Materials Reviews 57 (2012) 133–164. https://doi.org/10.1179/1743280411Y.0000000014.
[43] G. Gong, J. Ye, Y. Chi, Z. Zhao, Z. Wang, G. Xia, X. Du, H. Tian, H. Yu, C. Chen, Research status of laser additive manufacturing for metal: a review, Journal of Materials Research and Technology 15 (2021) 855–884. https://doi.org/10.1016/j.jmrt.2021.08.050.
[44] J.J. Lewandowski, M. Seifi, Metal Additive Manufacturing: A Review of Mechanical Properties, Annu. Rev. Mater. Res. 46 (2016) 151–186. https://doi.org/10.1146/annurev-matsci-070115-032024.
[45] U.M. Dilberoglu, B. Gharehpapagh, U. Yaman, M. Dolen, The Role of Additive Manufacturing in the Era of Industry 4.0, Procedia Manufacturing 11 (2017) 545–554. https://doi.org/10.1016/j.promfg.2017.07.148.

[46] W.J. Sames, F.A. List, S. Pannala, R.R. Dehoff, S.S. Babu, The metallurgy and processing science of metal additive manufacturing, International Materials Reviews 61 (2016) 315–360. https://doi.org/10.1080/09506608.2015.1116649.
[47] V. Madhavadas, D. Srivastava, U. Chadha, S. Aravind Raj, M.T.H. Sultan, F.S. Shahar, A.U.M. Shah, A review on metal additive manufacturing for intricately shaped aerospace components, CIRP Journal of Manufacturing Science and Technology 39 (2022) 18–36. https://doi.org/10.1016/j.cirpj.2022.07.005.
[48] C. Wei, L. Li, Recent progress and scientific challenges in multi-material additive manufacturing via laser-based powder bed fusion, Virtual and Physical Prototyping 16 (2021) 347–371. https://doi.org/10.1080/17452759.2021.1928520.
[49] Z. Liu, D. Zhao, P. Wang, M. Yan, C. Yang, Z. Chen, J. Lu, Z. Lu, Additive manufacturing of metals: Microstructure evolution and multistage control, Journal of Materials Science & Technology 100 (2022) 224–236. https://doi.org/10.1016/j.jmst.2021.06.011.
[50] S. Chowdhury, N. Yadaiah, C. Prakash, S. Ramakrishna, S. Dixit, L.R. Gupta, D. Buddhi, Laser powder bed fusion: a state-of-the-art review of the technology, materials, properties & defects, and numerical modelling, Journal of Materials Research and Technology 20 (2022) 2109–2172. https://doi.org/10.1016/j.jmrt.2022.07.121.
[51] X. Li, Z. Pan, L. Smolej, V. Karthik Nadimpalli, M. Moshiri, Towards manufacturing intra-layer multi-material mould tools with vertical interfaces using laser-based powder bed fusion, Materials & Design 243 (2024) 113056. https://doi.org/10.1016/j.matdes.2024.113056.
[52] A. Nazir, K.M. Abate, A. Kumar, J.-Y. Jeng, A state-of-the-art review on types, design, optimization, and additive manufacturing of cellular structures, Int J Adv Manuf Technol 104 (2019) 3489–3510. https://doi.org/10.1007/s00170-019-04085-3.
[53] C. Anstaett, C. Seidel, and G. Reinhart (Ed.), Fabrication of 3D Multi-material Parts Using Laser-based Powder Bed Fusion. Proceedings of the 28th Annual International Solid Freeform Fabrication Symposium - An Additive Manufacturing Conferece, Austin, 2017.
[54] M. Schneck, M. Horn, M. Schmitt, C. Seidel, G. Schlick, G. Reinhart, Review on additive hybrid- and multi-material-manufacturing of metals by powder bed fusion: state of technology and development potential, Prog Addit Manuf 6 (2021) 881–894. https://doi.org/10.1007/s40964-021-00205-2.
[55] P. Regenfuß, R. Ebert, H. Exner, Laser Micro Sintering – a Versatile Instrument for the Generation of Microparts, LTJ 4 (2007) 26–31. https://doi.org/10.1002/latj.200790139.
[56] D. Goll, D. Schuller, G. Martinek, T. Kunert, J. Schurr, C. Sinz, T. Schubert, T. Bernthaler, H. Riegel, G. Schneider, Additive manufacturing of soft magnetic materials and components, Additive Manufacturing 27 (2019) 428–439. https://doi.org/10.1016/j.addma.2019.02.021.
[57] J. Chen, Y. Yang, C. Song, M. Zhang, S. Wu, Di Wang, Interfacial microstructure and mechanical properties of 316L /CuSn10 multi-material bimetallic structure fabricated by selective laser melting, Materials Science and Engineering: A 752 (2019) 75–85. https://doi.org/10.1016/j.msea.2019.02.097.
[58] M. Schneck, M. Horn, M. Schindler, C. Seidel, Capability of Multi-Material Laser-Based Powder Bed Fusion—Development and Analysis of a Prototype Large Bore Engine Component, Metals 12 (2022) 44. https://doi.org/10.3390/met12010044.
[59] T. Stichel, T. Laumer, T. Baumüller, P. Amend, S. Roth, Powder Layer Preparation Using Vibration-controlled Capillary Steel Nozzles for Additive Manufacturing, Physics Procedia 56 (2014) 157–166. https://doi.org/10.1016/j.phpro.2014.08.158.

[60] T. Stichel, T. Laumer, P. Amend, S. Roth, Electrostatic Multi-Material Powder Deposition for Simultaneous Laser Beam Melting. International Conference on Information, Communication and Automation Technologies (ICAT), Vienna, 2014.
[61] V. Brøtan, O.Å. Berg, E.J. Øvrelid, A. Rudenkov, M. Demesh, T.L. Sebastian Reinery, I. Sorokina, Multi-material additive manufacturing through electrostatic metal powder attraction and laser-induced forward transfer, Procedia CIRP 126 (2024) 662–667. https://doi.org/10.1016/j.procir.2024.08.284.
[62] C. van der Eijk, O. Åsebø, Ø. Kolnes, T. Mugaas, R. Karlsen, R. Skjevdal, K. Boivie (Eds.), Metal Printing Process: A Rapid Manufacturing Process Based on Xerography using Metal Powders. Proceedings of the World PM2004 Conference, Vienna, 2004.
[63] K. Sertoglu. Aerosint and Aconity3D Develop Multi-Material Metal 3D Printer. 3D Printing Industry (3 October 2020). Available in: https://3dprintingindustry.com/news/aerosint-and-aconity3d-develop-multi-material-metal-3d-printer-168919/. Accessed on: June 30th 2025.
[64] A. Bulloch, A. Cruchley, A. Groom, A. Harris, F. Schulz, C.J. Tuck, R. Hague, M. Simonelli, Effect of interface orientation in laser powder bed fusion of IN718/GRCop-42 bimetallic parts for Aerospace, Additive Manufacturing Letters 15 (2025) 100331. https://doi.org/10.1016/j.addlet.2025.100331.
[65] C.P. Martendal, P. Esteves, L. Deillon, F. Malamud, A.M. Jamili, J.F. Löffler, M. Bambach, Effects of beam shaping on copper-steel interfaces in multi-material laser beam powder bed fusion, Journal of Materials Processing Technology 327 (2024) 118344. https://doi.org/10.1016/j.jmatprotec.2024.118344.
[66] I.B. Prestes, E.A. Jägle, Influence of the laser strategy on bi-metallic interfaces printed via multi-material laser-based powder bed fusion, Additive Manufacturing Letters 13 (2025) 100274. https://doi.org/10.1016/j.addlet.2025.100274.
[67] T. Schroeder, M. Lehmann, M. Horn, P. Kindermann, I. Uensal, F. Michal, A. Lippus, G. Schlick, C. Seidel, Transition zone parameter development in multi-material powder bed fusion: a general approach, Prog Addit Manuf (2024). https://doi.org/10.1007/s40964-024-00663-4.
[68] C. Wei, L. Liu, H. Cao, X. Zhong, X. Xu, Y. Gu, D. Cheng, Y. Huang, Z. Li, W. Guo, Z. Liu, L. Li, Cu10Sn to Ti6Al4V bonding mechanisms in laser-based powder bed fusion multiple material additive manufacturing with different build strategies, Additive Manufacturing 51 (2022) 102588. https://doi.org/10.1016/j.addma.2021.102588.
[69] S.L. Sing, S. Huang, G.D. Goh, G.L. Goh, C.F. Tey, J. Tan, W.Y. Yeong, Emerging metallic systems for additive manufacturing: In-situ alloying and multi-metal processing in laser powder bed fusion, Progress in Materials Science 119 (2021) 100795. https://doi.org/10.1016/j.pmatsci.2021.100795.
[70] Y. Bai, J. Zhang, C. Zhao, C. Li, H. Wang, Dual interfacial characterization and property in multi-material selective laser melting of 316L stainless steel and C52400 copper alloy, Materials Characterization 167 (2020) 110489. https://doi.org/10.1016/j.matchar.2020.110489.
[71] V. Errico, P. Posa, A. Fusco, A. Angelastro, S. Luisa Campanelli, Intralayer multi-material structure stainless-steel/nickel-superalloy fabricated via laser-powder bed fusion process, Manufacturing Letters 35 (2023) 11–15. https://doi.org/10.1016/j.mfglet.2022.11.004.
[72] Y. Wen, Y. Gao, R.L. Narayan, W. Cai, P. Wang, X. Wei, B. Zhang, U. Ramamurty, X. Qu, Tensile behavior of additively manufactured Inconel 718 and stainless steel 316L with compositionally graded joints, International Journal of Plasticity 189 (2025) 104342. https://doi.org/10.1016/j.ijplas.2025.104342.

[73] L.J. Gibson, M.F. Ashby, Cellular solids: Structure and properties, Second edition, Cambridge University Press, Cambridge, 1997.
[74] L.J. Gibson, Cellular Solids, MRS Bull. 28 (2003) 270–274. https://doi.org/10.1557/mrs2003.79.
[75] Z. Alomar, F. Concli, A Review of the Selective Laser Melting Lattice Structures and Their Numerical Models, Adv. Eng. Mater. 22 (2020) 2000611. https://doi.org/10.1002/adem.202000611.
[76] M.J. Mirzaali, A. Azarniya, S. Sovizi, J. Zhou, A.A. Zadpoor, Lattice structures made by laser powder bed fusion, in: Fundamentals of Laser Powder Bed Fusion of Metals, Elsevier, 2021, pp. 423–465.
[77] H. Xu, A. Farag, D. Pasini, Multilevel hierarchy in bi-material lattices with high specific stiffness and unbounded thermal expansion, Acta Materialia 134 (2017) 155–166. https://doi.org/10.1016/j.actamat.2017.05.059.
[78] S. P., J.D. Quadros, Y.I. Mogul, M. Mohin, A. Aabid, M. Baig, O.S. Ahmed, A review on mechanical metamaterials and additive manufacturing techniques for biomedical applications, Mater. Adv. 6 (2025) 887–908. https://doi.org/10.1039/D4MA00874J.
[79] T.-C. Lim, Anisotropic and negative thermal expansion behavior in a cellular microstructure, J Mater Sci 40 (2005) 3275–3277. https://doi.org/10.1007/s10853-005-2700-6.
[80] K. Wang, J. Chen, Z. Han, K. Wei, X. Yang, Z. Wang, D. Fang, Synergistically program thermal expansional and mechanical performances in 3D metamaterials: Design-Architecture-Performance, Journal of the Mechanics and Physics of Solids 169 (2022) 105064. https://doi.org/10.1016/j.jmps.2022.105064.
[81] K. Wei, H. Chen, Y. Pei, D. Fang, Planar lattices with tailorable coefficient of thermal expansion and high stiffness based on dual-material triangle unit, Journal of the Mechanics and Physics of Solids 86 (2016) 173–191. https://doi.org/10.1016/j.jmps.2015.10.004.
[82] Y. Nakamura (Ed.), Invar Systems. In: Ishikawa, Y., Miura, N. (eds) Physics and Engineering Applications of Magnetism. Springer Series in Solid-State Sciences, Springer, Berlin, Heidelberg, 1991.
[83] H. Xu, D. Pasini, Structurally Efficient Three-dimensional Metamaterials with Controllable Thermal Expansion, Sci. Rep. 6 (2016) 34924. https://doi.org/10.1038/srep34924.
[84] Z. Zeng, S. Gao, D.K. Pokkalla, S. Zhang, C. Han, F. Liu, Z. Xiao, S.Y. Kandukuri, Y. Liu, K. Zhou, Additive manufacturing of metallic metamaterials with enhanced mechanical properties enabled by microstructural and structural design, International Journal of Machine Tools and Manufacture 199 (2024) 104172. https://doi.org/10.1016/j.ijmachtools.2024.104172.
[85] R. Lakes, Cellular solids with tunable positive or negative thermal expansion of unbounded magnitude, Appl. Phys. Lett. 90 (2007) 221905. https://doi.org/10.1063/1.2743951.
[86] K. Wei, Y. Peng, K. Wang, S. Duan, X. Yang, W. Wen, Three dimensional lightweight lattice structures with large positive, zero and negative thermal expansion, Composite Structures 188 (2018) 287–296. https://doi.org/10.1016/j.compstruct.2018.01.030.
[87] X. Guo, X. Ni, J. Li, H. Zhang, F. Zhang, H. Yu, J. Wu, Y. Bai, H. Lei, Y. Huang, J.A. Rogers, Y. Zhang, Designing Mechanical Metamaterials with Kirigami-Inspired, Hierarchical Constructions for Giant Positive and Negative Thermal Expansion, Adv. Mater. 33 (2021) e2004919. https://doi.org/10.1002/adma.202004919.
[88] X. Li, L. Gao, W. Zhou, Y. Wang, Y. Lu, Novel 2D metamaterials with negative Poisson's ratio and negative thermal expansion, Extreme Mechanics Letters 30 (2019) 100498. https://doi.org/10.1016/j.eml.2019.100498.

[89] Z. Xia, W. Zhao, Y. Wang, P. Li, M. Xiao, L. Gao, Multi-material isogeometric topology optimization for thermoelastic metamaterials, International Journal of Heat and Mass Transfer 245 (2025) 126995. https://doi.org/10.1016/j.ijheatmasstransfer.2025.126995.
[90] B.C. White, A. Garland, B.L. Boyce, Topological homogenization of metamaterial variability, Materials Today 53 (2022) 16–26. https://doi.org/10.1016/j.mattod.2022.01.021.
[91] K. Wei, X. Xiao, J. Chen, Y. Wu, M. Li, Z. Wang, Additively manufactured bi-material metamaterial to program a wide range of thermal expansion, Materials & Design 198 (2021) 109343. https://doi.org/10.1016/j.matdes.2020.109343.
[92] C.A. Steeves, S.L. dos Santos e Lucato, M. He, E. Antinucci, J.W. Hutchinson, A.G. Evans, Concepts for structurally robust materials that combine low thermal expansion with high stiffness, Journal of the Mechanics and Physics of Solids 55 (2007) 1803–1822. https://doi.org/10.1016/j.jmps.2007.02.009.
[93] A. Takezawa, M. Kobashi, Design methodology for porous composites with tunable thermal expansion produced by multi-material topology optimization and additive manufacturing, Composites Part B: Engineering 131 (2017) 21–29. https://doi.org/10.1016/j.compositesb.2017.07.054.
[94] J.S. Raminhos, J.P. Borges, A. Velhinho, Development of polymeric anepectic meshes: auxetic metamaterials with negative thermal expansion, Smart Mater. Struct. 28 (2019) 45010. https://doi.org/10.1088/1361-665X/ab034b.
[95] E.M. Parsons, Lightweight cellular metal composites with zero and tunable thermal expansion enabled by ultrasonic additive manufacturing: Modeling, manufacturing, and testing, Composite Structures 223 (2019) 110656. https://doi.org/10.1016/j.compstruct.2019.02.031.
[96] Y. Ding, M. Akbari, X.-L. Gao, L. Ai, R. Kovacevic, Use of a Robotized Laser Powder-Feed Metal Additive Manufacturing System for Fabricating Metallic Metamaterials, in: T.S. Srivatsan, T.S. Sudarshan, K. Manigandan (Eds.), Manufacturing Techniques for Materials, CRC Press, 2018, pp. 51–65.
[97] I. Echeta, X. Feng, B. Dutton, R. Leach, S. Piano, Review of defects in lattice structures manufactured by powder bed fusion, Int J Adv Manuf Technol 106 (2020) 2649–2668. https://doi.org/10.1007/s00170-019-04753-4.
[98] T. Maconachie, M. Leary, B. Lozanovski, X. Zhang, M. Qian, O. Faruque, M. Brandt, SLM lattice structures: Properties, performance, applications and challenges, Materials & Design 183 (2019) 108137. https://doi.org/10.1016/j.matdes.2019.108137.
[99] M. Ackermann, J. Šafka, L. Voleský, Selective Laser Melting Technology and Manufacturing of Accurate Thin Structures, MSF 862 (2016) 104–111. https://doi.org/10.4028/www.scientific.net/MSF.862.104.
[100] W.W. Wits, C. de Vos, M. Montero-Sistiaga, M. de Smit, Laser powder bed fusion process parameters for the fabrication of unsupported overhang structures of metamaterial lattices, CIRP Annals (2025). https://doi.org/10.1016/j.cirp.2025.03.003.
[101] S. Li, H. Hassanin, M.M. Attallah, N.J. Adkins, K. Essa, The development of TiNi-based negative Poisson's ratio structure using selective laser melting, Acta Materialia 105 (2016) 75–83. https://doi.org/10.1016/j.actamat.2015.12.017.
[102] J. Xiong, D. Gu, H. Chen, D. Dai, Q. Shi, Structural optimization of re-entrant negative Poisson's ratio structure fabricated by selective laser melting, Materials & Design 120 (2017) 307–316. https://doi.org/10.1016/j.matdes.2017.02.022.
[103] J. Grünewald, P. Clarkson, R. Salveson, G. Fey, K. Wudy, Influence of Pulsed Exposure Strategies on Overhang Structures in Powder Bed Fusion of Ti6Al4V Using Laser Beam, Metals 11 (2021) 1125. https://doi.org/10.3390/met11071125.

[104] R. Lakes, Cellular solid structures with unbounded thermal expansion, Journal of Materials Science Letters 15 (1996) 475–477.
[105] T.-C. Lim, Negative thermal expansion structures constructed from positive thermal expansion trusses, J Mater Sci 47 (2012) 368–373. https://doi.org/10.1007/s10853-011-5806-z.
[106] T.-C. Lim, Negative thermal expansion in transversely isotropic space frame trusses, Phys. Status Solidi B 250 (2013) 2062–2069. https://doi.org/10.1002/pssb.201384234.
[107] J. Lehman, R.S. Lakes, Stiff, strong, zero thermal expansion lattices via material hierarchy, Composite Structures 107 (2014) 654–663. https://doi.org/10.1016/j.compstruct.2013.08.028.
[108] S. Watts, D.A. Tortorelli, Optimality of thermal expansion bounds in three dimensions, Extreme Mechanics Letters 12 (2017) 97–100. https://doi.org/10.1016/j.eml.2016.06.007.
[109] M.-M. Chen, M.-H. Fu, L.-H. Lan, S.V. Sheshenin, A novel 3D structure with tunable Poisson's ratio and tailorable coefficient of thermal expansion based on a tri-material triangle unit, Composite Structures 253 (2020) 112803. https://doi.org/10.1016/j.compstruct.2020.112803.
[110] H. Yu, B. Liang, Z. Zhao, P. Liu, H. Lei, W. Song, M. Chen, X. Guo, Metamaterials with a controllable thermal-mechanical stability: Mechanical designs, theoretical predictions and experimental demonstrations, Composites Science and Technology 207 (2021) 108694. https://doi.org/10.1016/j.compscitech.2021.108694.
[111] M.M. Toropova, C.A. Steeves, Adaptive bimaterial lattices to mitigate thermal expansion mismatch stresses in satellite structures, Acta Astronautica 113 (2015) 132–141. https://doi.org/10.1016/j.actaastro.2015.03.022.
[112] M.M. Toropova, Thermally adaptive axisymmetric trusses for satellite platforms, Acta Astronautica 181 (2021) 139–150. https://doi.org/10.1016/j.actaastro.2021.01.014.
[113] R. Edeson, G.S. Aglietti, A. Tatnall, Conventional stable structures for space optics: The state of the art, Acta Astronautica 66 (2010) 13–32. https://doi.org/10.1016/j.actaastro.2009.06.015.
[114] I. Levchenko, O. Baranov, M. Keidar, C. Riccardi, H. Roman, S. Xu, K. Alexander, 2024. Additive Technologies and Materials for the Next-Generation CubeSats and Small Satellites. Adv Funct Materials 34, 2407602. https://doi.org/10.1002/adfm.202407602.
[115] D. Yu, G. Hu, W. Ding, Y. Yang, J. Hong, Zero-thermal-expansion metamaterial with broadband vibration suppression, International Journal of Mechanical Sciences 258 (2023) 108590. https://doi.org/10.1016/j.ijmecsci.2023.108590.
[116] Jill M. Holz, Cengiz Kunt, Chris Lashley, Douglas B. McGuffey (Ed.), Development of a lightweight near-zero CTE optical bench for the Wide-Field Camera 3 instrument. Proceedings Volume 4854, Future EUV/UV and Visible Space Astrophysics Missions and Instrumentation, Waikoloa, 2003. https://doi.org/10.1117/12.459824.
[117] S. Serjeant, M. Elvis, G. Tinetti, The future of astronomy with small satellites, Nat Astron 4 (2020) 1031–1038. https://doi.org/10.1038/s41550-020-1201-5.
[118] A. Kinzel, J. Bachmann, Jaiswal, Rishi,R., Karnal, M., Novo, E., Porcelli, F., Schmidt, A., Schwarz, R., Hofmann, C., Forstner, R Knopp, A. (Eds.), Seamless Radio Access Network for Internet of Space (SeRANIS): New Space Mission for Research, Development, and In-Orbit Demonstration of Cutting-Edge Technologies. 73rd International Astronautical Congress (IAC), Paris, 2022.
[119] J.D. Binion, C.A. Mussman, E. Lier, T.H. Hand, D.H. Werner, 2025. A Near-Zero Index Metamaterial Lens for Reduced Complexity and High-Performance Active Electronically Scanned Arrays. Adv Elect Materials 11, 2400224. https://doi.org/10.1002/aelm.202400224.

[120] M.A. Ardeshana, F.N. Thakkar, S.G. Domadia, 2025. Composite structure design for broadband metamaterial absorption: Integrated nonlinearity and enhanced performance using lumped resistors. Journal of Applied Physics 137, 093104. https://doi.org/10.1063/5.0250746.
[121] P. Rohit, A. Datta, M. Satyanarayana, 2025. Optimized Graph Sample and Aggregate-Attention Network-Based High Gain Meta Surface Antenna Design for IoT Application. Int J Communication 38, e6043. https://doi.org/10.1002/dac.6043.
[122] S. Arora, S. Sharma, R. Anand, A. Gupta, R. Kumar, A.J.A. Al-Gburi, Integration of metamaterials for quintuple band-notched ultra-wideband antennas, Analog Integr Circ Sig Process 123 (2025). https://doi.org/10.1007/s10470-025-02355-7.
[123] R. Parasher, D. Yadav, A. Saharia, Design and analysis of hybrid fractal frequency-band reconfigurable metamaterial antenna for multi-standard wireless applications, Results in Engineering 26 (2025) 104696. https://doi.org/10.1016/j.rineng.2025.104696.
[124] J.-H. Cho, K.-Y. Park, C.-M. Lim, H.-W. Son, Design and Implementation of an X-Band Horn Antenna With a Metamaterial Lens Using 3D Printing Technology, IEEE Access 12 (2024) 17773–17781. https://doi.org/10.1109/ACCESS.2024.3358834.
[125] P. Langer, K. Sepahvand, C. Guist, J. Bär, A. Peplow, S. Marburg, Matching experimental and three dimensional numerical models for structural vibration problems with uncertainties, Journal of Sound and Vibration 417 (2018) 294–305. https://doi.org/10.1016/j.jsv.2017.11.042.

Publication {1}

Influence of the laser strategy on bi-metallic interfaces printed via multi-material laser-based powder bed fusion

Prestes, I.B., Jägle, E.A.

Additive Manufacturing Letters 13 (2025) 100274

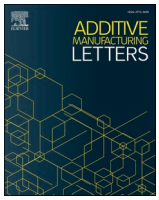
Additive Manufacturing Letters 13 (2025) 100274



Contents lists available at ScienceDirect

Additive Manufacturing Letters

journal homepage: www.elsevier.com/locate/addlet



Short Communication

Influence of the laser strategy on bi-metallic interfaces printed via multi-material laser-based powder bed fusion

Isabel B. Prestes *, Eric A. Jägle

Institute of Materials Science, Universität der Bundeswehr München, Werner-Heisenberg-Weg 39, Neubiberg, 85579, Germany

ARTICLE INFO

Keywords:
Multi-material additive manufacturing
Aerosint recoater
Laser powder bed fusion
scanning strategies

ABSTRACT

Metallic Multi-material Additive Manufacturing (MMAM) is an emerging research topic, with potential applications in heat exchangers, metamaterials and satellite components. In recent years, new multi-material laser powder bed fusion (PBF-LB) techniques have been developed. However, processing challenges may arise, since materials with dissimilar properties are mixed at the interfaces, which might lead to defects such as cracks. This work aims to investigate the influence of different laser scan strategies to achieve sound interfaces with different material mixing gradients. The samples, made of Inconel 718 and Invar were deposited by the patterning drums technique and were analyzed by means of optical microscopy and energy-dispersive X-ray spectroscopy (EDS) mappings and line scans. The orientation in which melt pools cross the material interface plays an important role in mixing the materials. Different orientations in subsequent layers create a certain "jagged" pattern of mixing at the interface. Sigmoid functions of Boltzmann fitted to the line scans show a significant slope steepness increase – up to 75 % – in the element count from double scan to single scan, suggesting a stronger material mixing. The double scan strategy leads to porosity at the interface and thus should be avoided. The remelt at the interface partially healed defects such as cracks but does not seem to influence the mixing width at the interface. These findings give general guidance for selecting scan strategies in MMAM depending on the desired mixing pattern at the material interface.

1. Introduction

Multi-material Additive Manufacturing (MMAM) technologies have the potential to improve the performance of parts manufactured by Additive Manufacturing (AM) by adding new properties and functions to them. Materials with different mechanical, thermal, chemical, optical or magnetic behavior may be printed together in order to introduce or enhance a desired property in specific regions of a part [1,2]. MMAM could additionally enable the 3D-printing of metamaterials, i.e. materials that are engineered to achieve properties that are not found in nature, that require a material combination. These are, for example, metamaterials that present a negative coefficient of thermal expansion, which have for example applications in passively thermally stabilized structures for satellites [3–6].

In recent years, metallic MMAM solutions have been developed, especially for the PBF-LB process, to broaden the applications of AM parts [2,7–10]. While blown-powder DED processes present a simpler way of joining two or more metals by switching between powder feeders, PBF-LB techniques are preferred for printing overhanging structures and intricate features with higher resolution, due to their smaller melt pools [8].

Mussatto [7] and Neirinck et al. [9] list the multi-material PBF-LB techniques that have been developed: conventional powder deposition [11], patterning drums [12], powder spreading with removal by suction [13,14], vibrating nozzles [15], hopper powder feeding [16], alternating powder deposition [17] and electrophotographic powder deposition [18]. The conventional and the alternating powder deposition are considered 2D-multi-material approaches, as only single-material layers can be deposited, but layers of different materials can be deposited in the same build job. The other techniques are 3D-multi-material approaches, where different material powders can be deposited in the same xy-plane [1,10]. Due to this capability, in association to a reasonable accuracy during powder deposition, the patterning drums, electrophotographic powder deposition and vibrating nozzle systems are considered the most significant techniques in metallic MMAM [7]. In this work, samples printed by the patterning drums technique are investigated.

The introduction of two materials in metallic MMAM leads to new processing challenges. One of these is the unavoidable intermixing of the

* Corresponding author.
E-mail address: isabel.prestes@unibw.de (I.B. Prestes).

https://doi.org/10.1016/j.addlet.2025.100274
Received 10 June 2024; Received in revised form 29 January 2025; Accepted 9 February 2025
Available online 10 February 2025
2772-3690/© 2025 The Authors. Published by Elsevier B.V. This is an open access article under the CC BY license (http://creativecommons.org/licenses/by/4.0/).

two materials when different powders are melted in the same melt pool, effectively locally creating a new alloy with intermediate composition. This mixed material may show a solidification behavior and other properties that are detrimental to the printed part, causing defects, such as cracks and the formation of intermetallic phases [11,13,19–22]. Therefore, the materials' interface design and AM process parametrization as well as its characterization play an important role in the research of metallic MMAM [7,11].

Although some works have already been conducted using the above-mentioned metallic MMAM techniques [11,13–21], this research area is still not widely investigated [7,8], especially using the patterning drums technique [9]. The exposure of two different materials deposited in the same xy-plane had not been possible until recent years, with the development of systems that allow the deposition of bi-metallic powder beds [7]. Moreover, most of the work developed in this area so far focused on printing dissimilar metals together such as Cu- and Fe-alloys. These materials have highly different printing parameters and thus are restricted to being exposed separately [11,13,16,19–21]. By using an adapted powder bed, Errico et al. [23] were able to print a nickel superalloy and a stainless steel together with the same parameters, but the authors did not investigate different scanning strategies at the materials' interface. In this work, two alloys (Invar and Inconel 718) were printed using the same parameters, enabling a novel study of the influence of different scanning strategies on their interface.

The choice for this combination was based on their good metallurgical compatibility, since both present an FCC lattice structure and intermetallic phases are not foreseen between Fe and Ni in the composition range covered by these alloys [24–27]. On the other hand, the large coefficient of thermal expansion (CTE) difference between these materials contradicts good practices in dissimilar metal welding approaches, as it might lead to issues such as cracking [26,28–30]. However, there are applications, e.g. metamaterials with tunable thermal expansion for satellite applications, where this feature plays an important role and Invar is especially adequate due to its very low CTE [3,4,31].

2. Materials and methods

In this work, different laser strategies were used to print bi-metallic cuboidal samples (8 × 8 mm width and length, 6 mm height) made of Invar and Inconel 718. Both powders were provided by Praxair, gas atomized and had a particle size range of 15–45 μm ($D10_{Invar}$=15.8 μm; $D10_{IN718}$=20 μm; $D50_{Invar}$=30.8 μm; $D50_{IN718}$=30 μm; $D90_{Invar}$=52.6 μm;$D90_{IN718}$=44 μm).

The 3D multi-material PBF-LB process was performed in an Aconity MIDI+ machine equipped with a selective powder deposition recoater developed by Aerosint (see Fig. A.1 for the schematic of the patterning drum principle). Alignment steps prior to the build job in which the cubes were printed were done as follows (see Fig. A.2 for schematic): First, the alignment between the powders is checked visually by depositing a layer of powder pattern consisting of both materials. Insufficient alignment is visible by gaps between the deposited powders and can be rectified by adjusting the drum position forward/backward (if the gaps are parallel to the powder deposition direction), or by adjusting deposition timings in the software (if the gaps are perpendicular to the deposition direction). Subsequently, the alignment between the powder pattern and the laser is adjusted by exposing a specific laser pattern on a powder test pattern and by changing the laser scanner origin as necessary. All cuboids were printed in the same build job to guarantee that they had the same alignment conditions.

The laser strategies that were applied to be compared were all simple, bidirectional scanning, with the following differing parameters: (1) 45° vs. 67° angle increment per layer; (2) single scan (Fig. 1a) vs. double scan (Fig. 1b) and (3) with vs. without remelt at the interface (Fig. 1c). "Single scan" means that both materials are printed

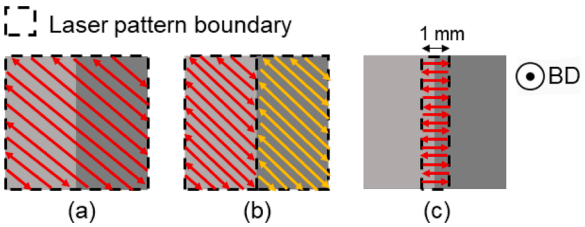


Fig. 1. Different printing strategies of the bi-material cubes: a) single scan, on which both materials were printed simultaneously, without interrupting the scanning vector at the material interface; b) double scan, on which Inconel 718 was printed first and Invar was printed subsequently; and c) remelt, on which the material interfaces were lasered again once the materials were printed with one of the two strategies detailed before.

simultaneously, without interrupting the scan vectors at the interface, while "double scan" means that one material is printed first (in this case, Inconel 718) with scan vectors ending exactly at the material interface, and the second material (Invar) is printed subsequently. The remelt strategy consists of exposing the materials' interface again once the materials were printed. The remelt width symmetrically covers 1 mm of the interface region.

The angle increments of 45° and 67° are typically found in literature and the former allows repeated patterns to be observed, while in the latter, a scan direction only repeats after many layers. While double scan is usually applied in the MMAM literature due to the dissimilar PBF-LB parameters between the materials, the current material combination also allows single scan to be applied. Finally, the remelt strategy can potentially heal defects, such as cracks and pores.

A prior parameter study to obtain dense parts (>99 % density) was performed for both materials. The PBF-LB parameters used to print the two materials were the same: 180 W laser power, 940 mm/s scanning speed, 80 μm hatch spacing and laser beam diameter and 40 μm layer height. For the remelt step, the same conditions were applied, except that the laser power was reduced to 150W.

The six cuboids observed in this work are described in Table 1. A picture of the multi-material build job and optical microscopy images of the cubes analyzed in this work is shown in Fig. 2.

The cuboids' cross sections were metallographically prepared, polished with a colloidal silica solution ("OP-S" by Struers) solution with 1 % HCl added, and etched with a solution consisting of 75 ml ethanol + 25 ml HCl + 9 ml H_2O_2. Optical microscopy pictures were taken in a Zeiss Axiophot, while SEM analyses were done in a Zeiss Ultra 55 SEM equipped with an EDAX Octane Elite EDS system. EDS mappings and line scans with a width of 95 μm and a length of approximately 900 μm were performed at the materials' interface to observe the material mixture using a 20 kV beam voltage, 120 μm aperture and a 2 μm step size. Considering the chemical composition of the two metals (Table 2),

Table 1
Description of laser strategies used for the studied cuboids.

Cuboid	Scan strategy	Angle increment	Remelt
S45	Single	45°	No
S45R	Single	45°	Yes
S67	Single	67°	No
S67R	Single	67°	Yes
D67	Double	67°	No
D67R	Double	67°	Yes

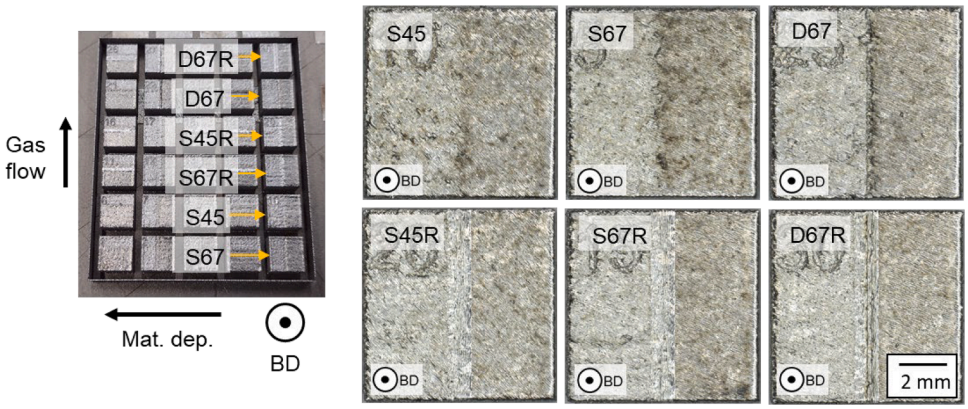


Fig. 2. Picture of the multi-material build job, on the left-hand side, with yellow arrows pointing the cubes analyzed in this work; and optical microscopy images of these cubes, on the right-hand side.

Table 2
Chemical composition of the metal powders provided by Praxair.

wt.%	Fe	Ni	Cr	Al	C	Mo	Nb	Ti	Co
Inconel 718	17.73	52.97	19.27	0.48	0.03	2.94	4.99	1.00	0.33
Invar	Balance	36.00	0.04	–	0.00	–	–	–	0.04

Fe was chosen to represent regions where Invar was present, while Cr was chosen to represent regions where Inconel 718 was present.

The mappings aimed to observe the mixing pattern created at the interface, while the line scans aimed to measure the width of the mixing zone by taking the mean value of five line scans. In the cases where the line scan length of 900 μm was not enough to cover the entire mixing zone, i.e. no clear plateau of element counts was achieved at the beginning or the end of the line scans, additional line scans were taken from regions to the left and to the right of the interface. The element counts were normalized from 0 to 100 and the sigmoid function of Boltzmann (Eq. (1)) was fit to them in order to extract the gradient of the element count. This function was applied as a fitting curve due to its similarity to the resulting line scans: two plateaus connected by an S-shaped curve.

$$Y = A2 + \frac{A1 - A2}{1 + e^{\left(\frac{x - x_0}{dx}\right)}} \tag{1}$$

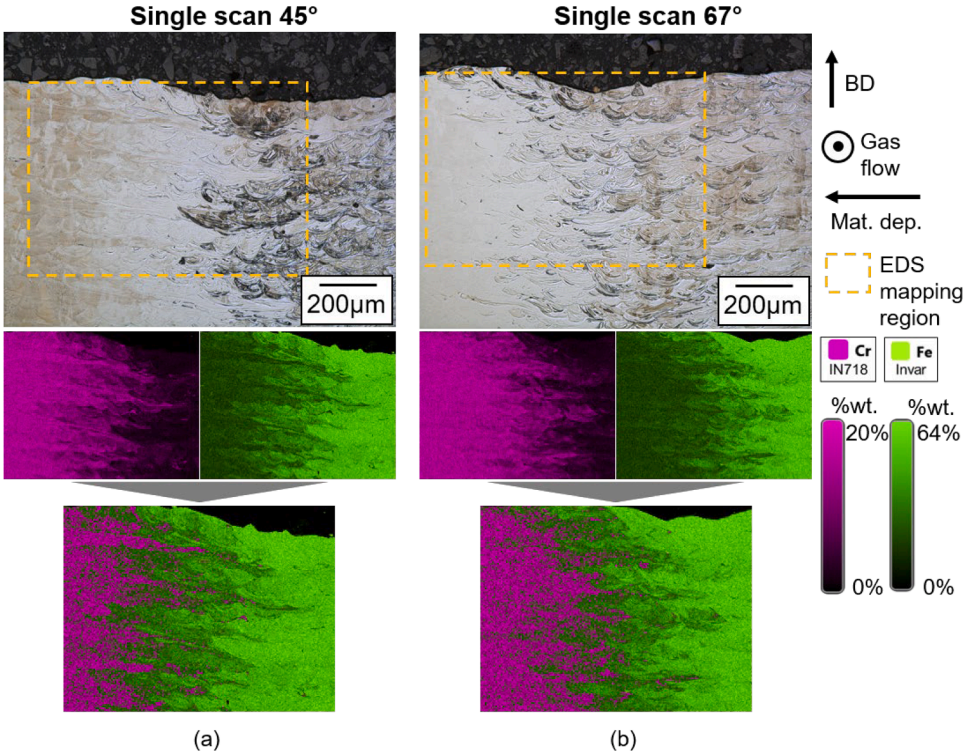


Fig. 3. Micrographs and EDS mappings of S45 (a) and S67 (b) samples printed with single scan strategy, but with different increment angles. The EDS mappings of the elements Cr (pink), representing regions containing IN718, and Fe (green), representing regions containing Invar, are shown separately and overlaid.

3. Results

This section is divided in three subsections, each of them comparing different strategies investigated in this work. First, angle increments of 45° and 67° are observed, where only single scan samples were compared. Secondly, single scan and double scan samples with the same angle increment are compared. Finally, all the samples are compared with their corresponding pair with remelt at the interface. In Fig. 2, the printed cuboids analyzed in this work are shown.

3.1. Angle increment

Micrographs of the cross-section of the S45 and S67 samples are shown in Fig. 3a and b, respectively. Below the micrographs, EDS mappings are shown presenting where Cr (pink) and Fe (green) atoms are to be found in each sample, representing where Inconel 718 and Invar are present, respectively. Below, these mappings are also shown added together.

In the EDS mappings, color patterns are visible at the materials' interface, which indicate the mixing of one material into the other. These patterns will be henceforth called "jagged" patterns. While these jagged patterns seem to be irregular in the S67 sample, they appear regularly in the S45 sample and repeat every four material layers, when the same scanning direction is repeated, considering the 45° angle increment. As both materials are always deposited side by side, their mixture is attributed to the melt pool, that drags one material into the next one, as shown schematically in Fig. 4. The powders are initially deposited side-by-side (Fig. 4a) and, depending on the scanning direction, different mixing degrees will occur. When the scanning direction is, for example, parallel to the interface (Fig. 4b), the melt pool will cause mixing only where powder particles of both materials are present. On the other hand, taking the other extreme example, when the scanning direction is perpendicular to the interface of deposited materials (Fig. 4c), much more mixing will occur, as the melt pool carries yet unsolidified material of the first powder pattern into the powder pattern of the next material. Therefore, the scanning direction and, consequently, its angle increment have an influence on the jagged pattern.

To illustrate this effect, simple schematic images were created using a basic algorithm. Under the assumptions of a semi-elliptical melt pool (width of 120 μm and depth of 65 μm determined from micrographs), and the laser scan strategies used in the experiments, instantaneous and complete mixing of the two powders in the melt pool was simulated. This was achieved by starting with a three-dimensional material with a sharp interface between the two materials. At each step of the algorithm, i.e., at every pixel along the scan vectors, all pixels within the melt pool of predefined size are assigned the current average composition of the entire melt pool. The resulting mixing patterns of multiple layers with angle increments of 45° and 67°, respectively, are illustrated in Fig. 4d and e. The regular mixing pattern in every four layers is clearly visible in

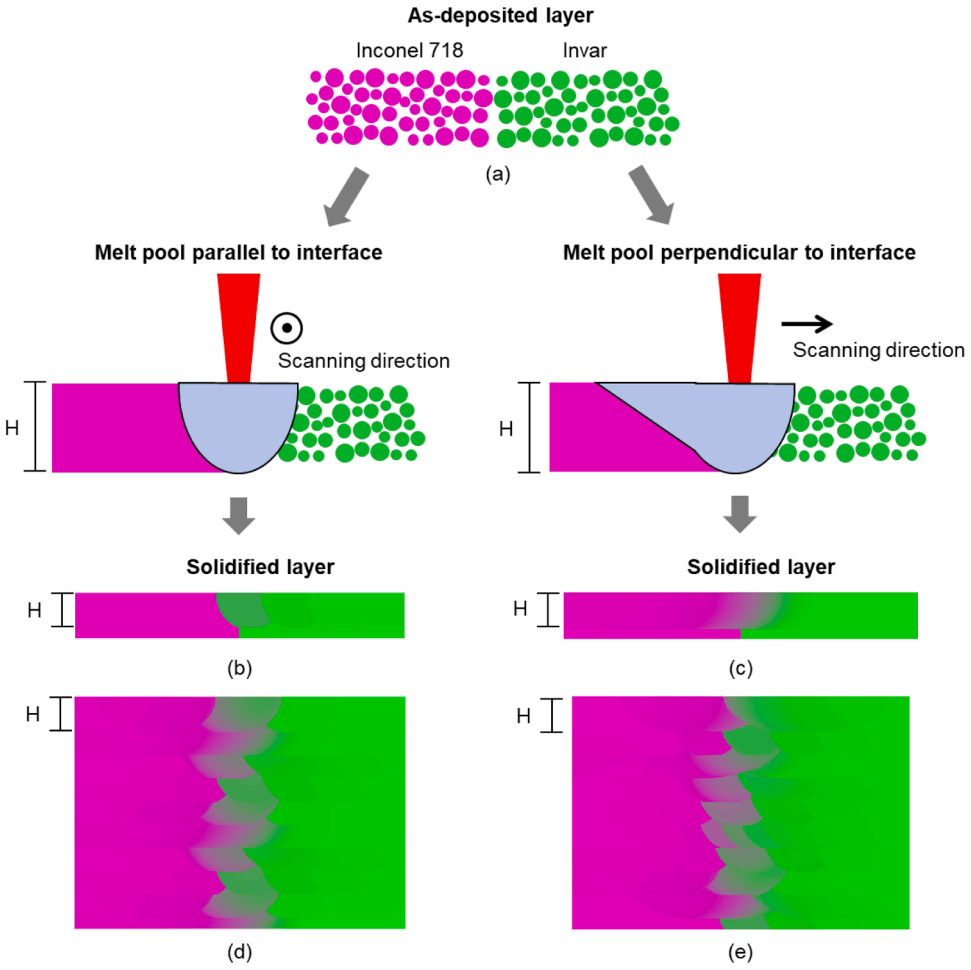


Fig. 4. Schematization of material mixing depending on the scanning direction: (a) as-deposited material powder patterns side-by-side; (b) scanning direction parallel to the interface, on which the material mixing occurs mainly at the interface itself, where powder particles of both materials are present and; (c) scanning direction perpendicular to the interface, on which the melt pool carries Inconel 718 that is not yet solidified into Invar's powder pattern, causing more mixing; (d) simulation of multiple-layer mixing with angle increments of 45° and (e) 67°.

the former, and the irregular jagged mixing pattern is visible in the latter scan strategy. Note that this simulation algorithm does not attempt to correctly model the physical reality of the PBF-LB process (e.g. Marangoni convection is omitted), but rather only to illustrate the effect that the choice of scan strategy has on mixing conditions under idealized circumstances.

3.2. Scan strategy

Single scan and double scan strategies can be compared by observing the micrographs of the samples S67 and D67, shown in Fig. 5a and b, respectively. The porosity at the interface appears regularly and in a much larger scale when using the double scan strategy.

Another interesting observation is that no cracks were found close to the interface of the cuboids printed with single scan strategy, but some were found along the interface of the double scan cuboids (Fig. 6). These cracks were only found in the Inconel 718 side, which was the material exposed first.

3.3. Remelt

Fig. 7 contains EDS mappings (Cr counts) of samples printed with different scan strategies (Fig. 7a, c, e) and their respective remelt version (Fig. 7b, d, f). The EDS mappings of Fe (green) show the mixing pattern and indicate where each material is to be found, with darker regions representing where Inconel 718 is present and a more intense green color, where Invar is present. For micrographs of these samples, see Fig. B.1.

The Fe counts taken from the line scans of the interfaces and normalized from 0 to 100 are shown in Fig. 8a. In order to quantify the concentration gradient that the remelt strategy has caused, the sigmoid function of Boltzmann was fit to each of the line scans (Fig. 8b) and the resulting best-fit parameter dx in Eq. (1), which is indicative of the curves' slopes, is given in Table 3.

By comparing Fig. 8a and b, the Boltzmann functions fit well to the line scans and presented an R-squared larger than 0.98 in all cases. Therefore, the steepness of the Fe count slope can be correlated to the material mixture caused by the different strategies. The single scan strategy obviously broadens the mixing at the interface in comparison to the double scan strategy, evidenced by the 71 % slope steepness increase from D67 to S67 and a 75 % increase from D67R to S67R. However, no clear influence in mixing is seen when remelting is applied. Remelting increased the slope by 43 % in the S67 sample, 25 % in the D67 sample, but only 1 % in the S45 sample.

In comparison to the D67 sample (Fig. 6), the D67R sample, which had its interface remelted, showed significantly fewer cracks and pores, as is to be seen in Fig. 9. It may be attributed to the fact that the remelt procedure helps fill up possible cracks and smaller pores that were produced during the printing process. Moreover, the cracks found appear mostly at the top of the sample, where there might not have been enough remelt procedures from the following layers to close them.

4. Discussion

As different laser strategies have an influence on the interface of multi-material parts and may even determine whether it will be defect-free or not, the results show the importance of parameter studies in multi-material printing that go beyond finding optimal parameters for the single materials. Previous works in MMAM affirm that unsuitable printing parameters for multi-material parts may lead to porosity, balling, cracking, intermetallic phase formation and delamination, due to different chemical, physical, optical and thermal properties of the materials [7,8]. Due to the dissimilar nature of the materials used in these works, studies would be restricted to double scan strategies, as the two materials require quite different printing parameters. This present work has shown that even similar alloys that can be printed with the same parameters require a more careful look into their interfaces, since different scanning strategies may be applied and lead to different results.

In the EDS mappings, a clear mixing of elements by fluid flow between the materials can be seen, regardless if remelting was applied or not, which, according to Liu et al. [21], indicates a good metallurgical bonding of the materials. The multi-material deposition process with the Aerosint recoater may inherently lead to the presence of isolated foreign particles in the deposited powder pattern, however, the observed jagged patterns could not be explained by an irregular powder deposition, as they are dependent on the angle increment per layer, as shown in Fig. 3. The melt pools that cross from one material into the other in the single scan strategy seem to play an important role in affecting the material mixture, as elements that are not yet solidified from the first material are carried to the next one by the melt pool. Therefore, an increase or decrease in the material mixture could be tuned by changing the melt pool length, i.e. by changing the laser scanning speed, as the Marangoni flow is directly proportional to it [8]. The sharp interface between the materials when the double scan strategy is applied (Fig. 7e-f) corroborates this hypothesis, as the melt pools are interrupted at the interface, leading to a minimum material mixture.

The remelt strategy has somewhat broadened the mixture zone in every strategy analyzed in this work, but this effect was not observed consistently in the line scans and their Boltzmann sigmoid function fits. In order to better understand the influence of remelt at the interface, further investigation is needed.

On the other hand, the EDS mappings and line scans have shown that the double scan strategy significantly reduces the material mixture,

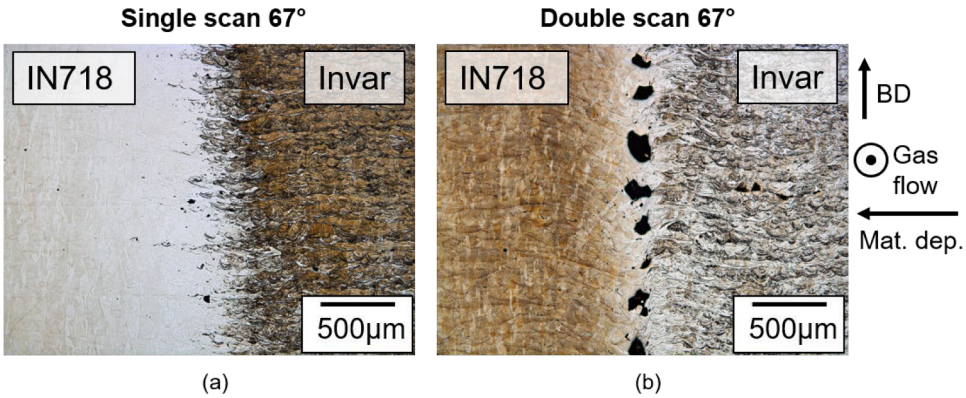


Fig. 5. Micrographs of S67 (a) and D67 (b) samples printed with single scan and double scan strategy, respectively.

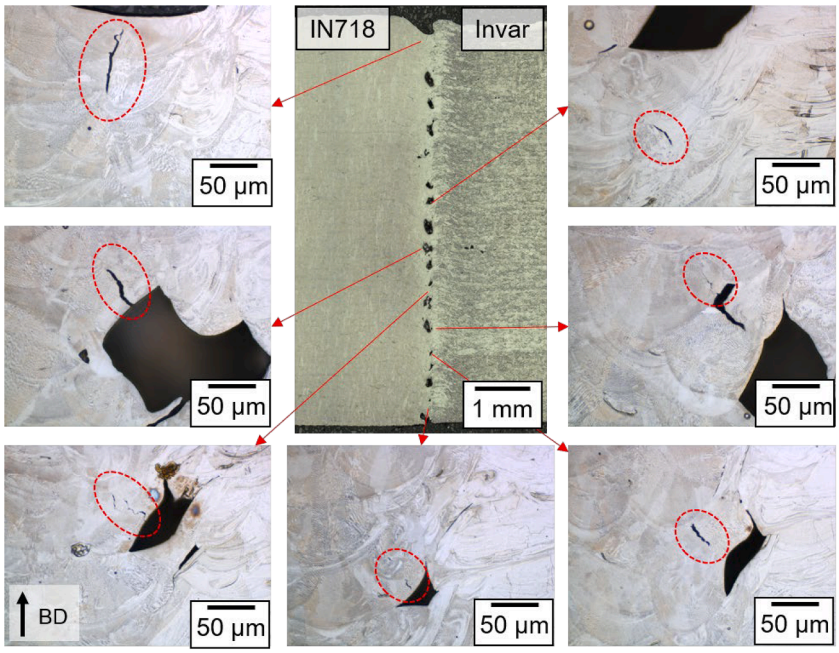


Fig. 6. Cracks found at the materials' interface of sample D67 , printed with double scan strategy.

which could be an interesting outcome for alloy combinations that could lead to the formation of undesirable brittle phases when thoroughly mixed. However, one must keep in mind that these results rely not only on the proper alignment of the powder patterns and the laser, but also on the quality and accuracy of the deposition system. The application of the double scan strategy in this work has led to porosity at the materials' interfaces (see Fig. 5), that could not be healed by remelting (see Fig. 9). Since there was no gap between the laser vectors that scanned each material and the laser parameters were kept constant, one of the possible causes for this porosity might be the powder denudation caused by the laser tracks as they approach the interface, leaving not enough particles where the second material was yet to be printed. Matthews et al. [32] observed dependency of the width of the denudation zone on the laser parameters and chamber pressure and showed that the width of this zone may reach up to 800 µm. Importantly, when the double scan strategy is applied in either Invar or Inconel 718 single material cuboids, the porosity shape and recurrence seen in this work are not reproduced.

Another possible explanation is that the side surface of 3D printed parts is irregular and the printed parts tend to be about 10 to 20 µm larger than the CAD model because of the melt pool size. The irregular surface that advances into the next powder pattern may act as a shield to the second material powder particles from the laser beam, preventing them from getting melted and thus leading to porosity. Moreover, the as-printed surface might reduce the wettability of the molten powder.

Finally, a gap between the powder patterns could be responsible for or, at least, contribute to the porosity, since the periodicity and size of the pores in double scan strategy cubes printed in different multi-material build jobs were different. In this work, the material interfaces were perpendicular to the deposition direction, which means that the powder alignment is adjusted by configuring deposition timing in the software and can also be influenced by the mesh resolution of the multi-material recoater. A lack of powder at the interface in the same order of magnitude of the pores (~100 µm), together with scan vectors that abruptly stop before reaching the next powder pattern, could possibly lead to the porosity seen in this work. This explanation was initially discounted because in the same build job with the same powder drum alignment, cuboids with single scan strategy did not show porosity. However, it is possible that in the single scan strategy the porosity may not appear, because the melt pool advances from one into the next powder pattern, and thus transports material into a possible powder pattern gap. If the gap is smaller than the melt pools, this may entirely heal any pores and only lead to a slight dip at the interface (observed at the top layer of S45 and S67, in Fig. 3a and b, respectively). This would be the case only for the single scan strategy and not for the double scan strategy where scan vectors stop at the materials' interface.

Besides porosity, cracks were also seen in the samples exposed with the double scan strategy, specifically, in the Inconel 718 side close to the interface (see Fig. 6). Works done in Inconel 718 single-material PBF-LB did not mention the formation of cracks in the as-built material [33–38] and also in our work, cracks were only found close to the bi-metallic interface. Imbrogno, Alhuzaim and Attallah [39] printed Inconel 718 via DED and noticed the presence of intermetallic Laves phase, which could lead to cracking due to its brittle nature. However, probably due to DED being a deposition process with much lower cooling rates than PBF-LB, no intermetallic phases were identified in our EDS analyses done close to the cracks.

A necessary precondition for any cracking during AM is the solidification and shrinkage stresses inherent to the AM process. It is known that the top layer of a printed part will be subjected to tensile residual stresses, as the solid layers below restrict the expansion of the molten material, which later might lead to cracking [39,40]. A similar behavior could happen when double scan strategy is applied, as the second printed material would also have its expansion restricted by the material printed first. In the samples of this work, however, the cracks were found in Inconel 718, which was printed before Invar. Therefore, the formation of the cracks cannot be attributed to this geometric constraint effect.

Previous works in multi-material additive manufacturing also reported the presence of cracks close to the interface, although they combined alloys different from the ones used in this work [11,13,16,19–22]. Chen et al. [16,19] printed Cu10Sn on top of 316 L and observed cracks in the steel. The authors attributed this to the CTE mismatch that induced Cu10Sn to tear the already printed 316 L apart. In their work, the cracks appeared perpendicular to the interface and were considerably larger (in the order of 100 µm) than the ones found in this work. Bai et al. [11] printed a C52400 copper alloy part between 316 L parts and identified similar cracks in 316 L, independently if it was printed below or on top of the copper alloy. The cause of the cracks was also attributed to the CTE mismatch. However, the CTE mismatch of the alloy

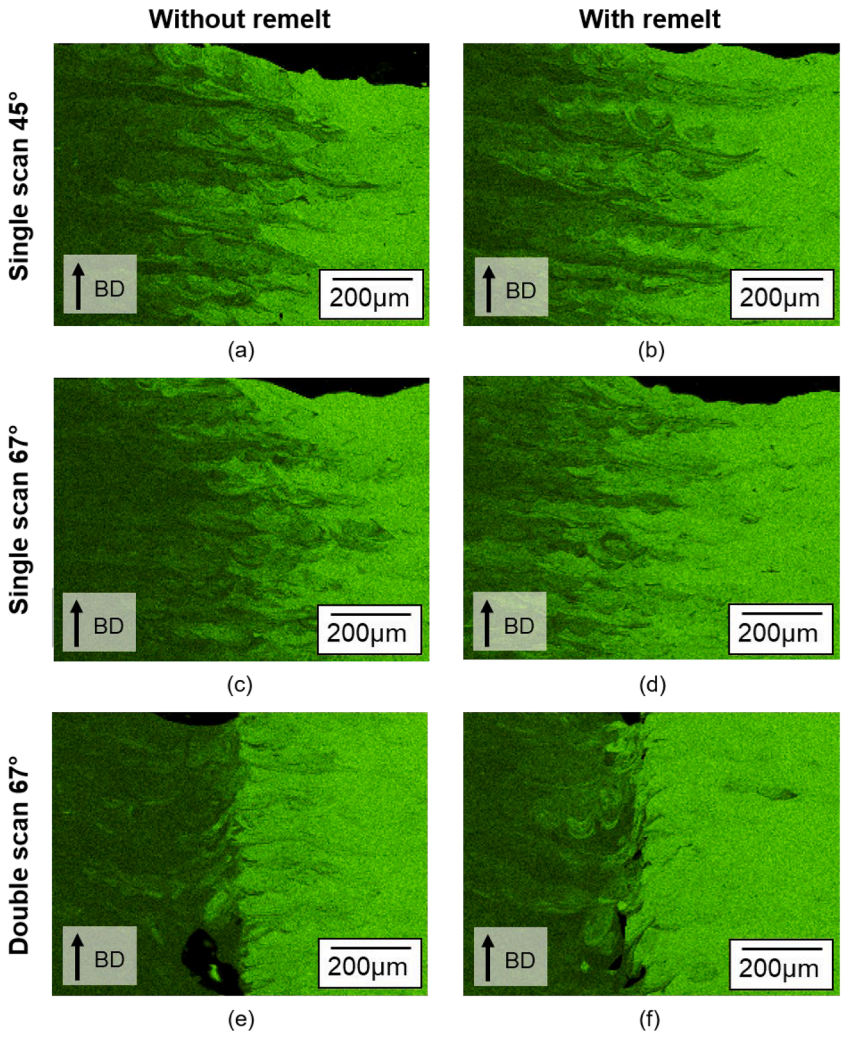


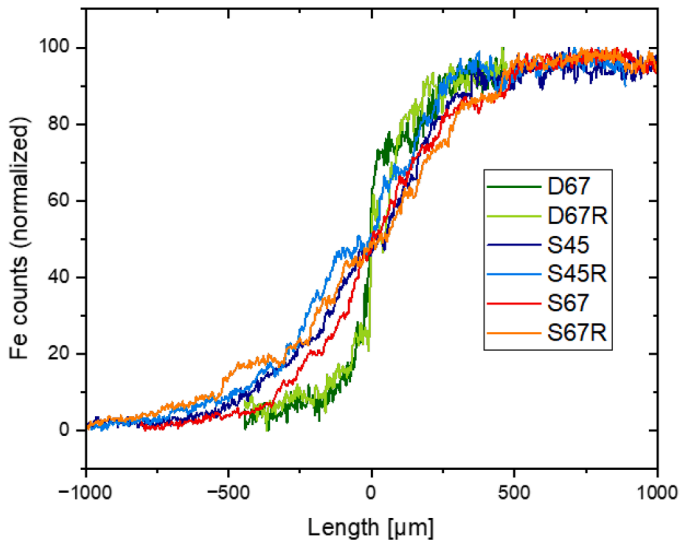
Fig. 7. Comparison of samples printed with different laser strategies: (a) S45, (b) S45R, (c) S67, (d) S67R, (e) D67 and (f) D67R. The EDS mappings are overlaid, showing regions where Cr was detected, representing regions containing IN718, and where Fe was detected, representing regions containing Invar36.

combination used in this work was considerably higher and yet cracks were not found in the cuboids exposed with the single scan strategy.

Mei et al. [20] produced multi-material parts by printing IN718 parts between 316 L and observed cracks in the 316 L sides close to the interface. The size and shape of the cracks are similar to those seen in this work and the authors believe the cracks were formed by non-optimal printing parameters at the interface, since the two materials were printed with considerably different energy densities. Moreover, the new alloy created at the interface of the two materials might require a new set of parameters, different from the ones used to print the original alloys. In this work, however, the two materials were printed with the same parameter set and these cracks were not found even when a more intense mixing of the alloys occurred by applying the single scan strategy.

Due to the absence of intermetallic phases in the crack vicinity, their presence only in the mixed material region, and their morphology, we hypothesize that these cracks are solidification cracks. Since the cracks were always found close to pores or coming directly from them, as seen in Fig. 6 and Fig. 9, their appearance could be associated with overheating of the material. When a powder layer is being exposed and the printed layer beneath it presents a lower heat conductivity due to porosity and hence does not dissipate heat quickly enough, the energy density might be too high and lead to cracking. Another contributing factor is that the liquid material provided by the melting of the subsequent layers is not enough to fill the pore created on the previous layer. Thus, during solidification, there will not be sufficient molten material to fill the gaps created by shrinkage. This effect could be intensified by the possible gap between the powder patterns, which reduces the amount of molten material available.

The remelt procedure has helped the healing of defects, such as porosity and cracks, in previous works [8,40,41] and the infiltration of molten material into previously built cracks is also considered in some multi-material works as a potential way to heal them [11,13]. Due to the sizes of the pores in the double scan samples, the remelt strategy seems to have led only to a slight reduction of the porosity. On the other hand, the cracks became much less frequent. If solidification cracking occurs due to residual stresses and a lack of material to backfill cracks, a remelt strategy may help in healing them. Moreover, besides remelt, we speculate that other laser scan strategies could potentially improve interface defects, including laser defocusing, beam shaping and path wobbling. The confirmation of these is subject to future work.



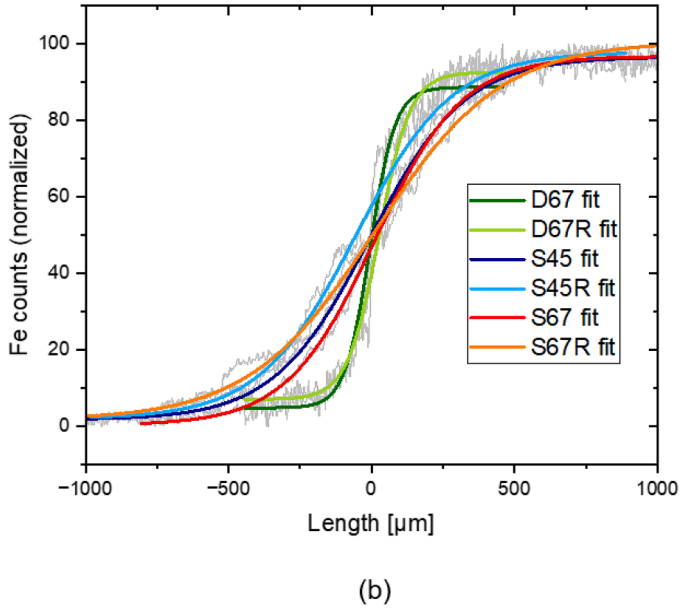


Fig. 8. Results of the line scans taken from the materials' interface of the analyzed samples: (a) Fe counts taken from the mean value of five line scans normalized from 0 to 100 and (b) the Boltzmann sigmoid function fit to these line scans, in order to extract the steepness of the Fe count slope and, thus the intensity of material mixing.

Table 3
Steepness of the Boltzmann sigmoid function slope fit to the line scans of each sample.

Sample	S45	S45R	S67	S67R	D67	D67R
dx (Boltzmann)	166.56 ± 0.81	169.03 ± 1.22	153.92 ± 0.70	219.70 ± 1.19	43.89 ± 0.95	54.79 ± 0.80

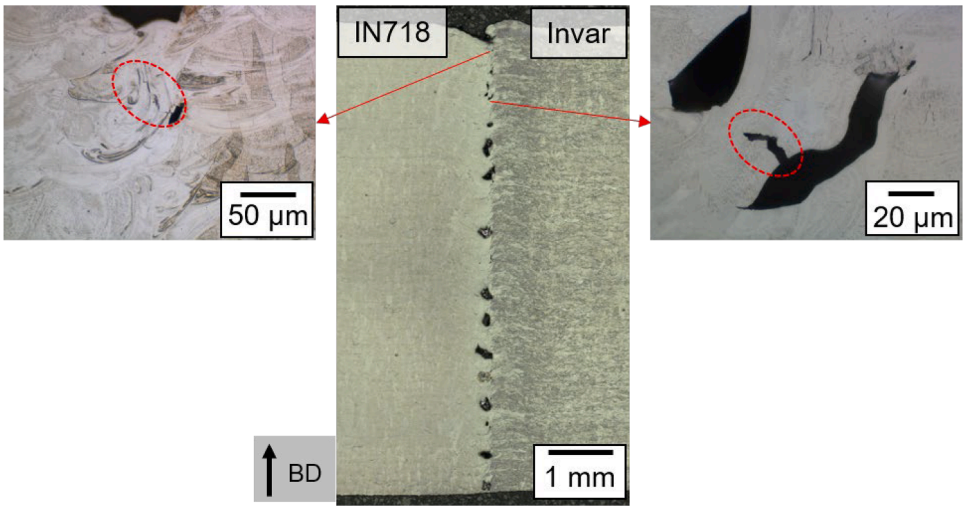


Fig. 9. Cracks found at the materials' interface of sample D67R, printed with double scan strategy followed by a remelt procedure at the interface.

5. Conclusions

In this work, a study on the influence of different laser strategies on the interface of Inconel 718 and Invar printed by multi-material PBF-LB with an Aerosint selective powder deposition recoater was conducted. Optical microscopy and EDS analyses were used for the characterization of the samples. The following conclusions are taken from this investigation:

- The angle increment per layer leads to different material mixing patterns at the interface, that were called jagged patterns. While a guideline for an optimal increment per layer cannot be suggested in terms of material mixture or mechanical properties, the 45° angle increment presents a regular jagged pattern that is repeated every four layers, whereas a 67° angle increment will lead to a more randomized pattern. In order to study the interface and to isolate the scanning direction influence, a regular patterning, such as 45° or even 90° angle increment, is preferred.
- The double scan strategy, i.e. printing one material after the other, significantly reduces material mixing, but leads to porosity at the interface, that could be associated with the following factors, individually or combined: (1) powder denudation at the interface during the printing of the first material, (2) irregular surface of printed parts, that might shield the neighboring powder from the laser beam and might not be as easily wetted by the second printed material and (3) a gap between the powder patterns that is not filled by the melt pool, since the scan vectors stop at the material interface, before reaching the next powder pattern.
- The porosity in the double scan strategy cubes could have caused cracks close to the interface, due to overheating or lack of molten material to fill the porosity from previous layers.
- The remelt strategy at the interface seems to have broadened the mixed zone, but no consistent influence could be identified in this work. Moreover, this strategy was not entirely effective in removing or filling cracks and pores when double scan was applied.
- The single scan strategy is more robust against porosity at the interface in case there is a powder pattern misalignment that creates a gap at the material's interface. Therefore, whenever this strategy is possible, i.e. when the materials have an overlapping process window, it is preferred.

Funding

This research as part of project SeRANIS is funded by dtec.bw – Digitalization and Technology Research Center of the Bundeswehr which we gratefully acknowledge. dtec.bw is funded by the European Union – NextGenerationEU.

CRediT authorship contribution statement

Isabel B. Prestes: Writing – original draft, Visualization, Validation, Methodology, Investigation, Formal analysis, Data curation, Conceptualization. **Eric A. Jägle:** Writing – review & editing, Supervision, Software, Methodology, Funding acquisition, Conceptualization.

Declaration of competing interest

The authors declare the following financial interests/personal relationships which may be considered as potential competing interests:

Isabel Beatriz Prestes reports financial support was provided by dtec.bw (Digitalization and Technology Research Center of the Bundeswehr)-NextGenerationEU. If there are other authors, they declare that they have no known competing financial interests or personal relationships that could have appeared to influence the work reported in this paper.

APPENDIX A. Aerosint recoater functioning

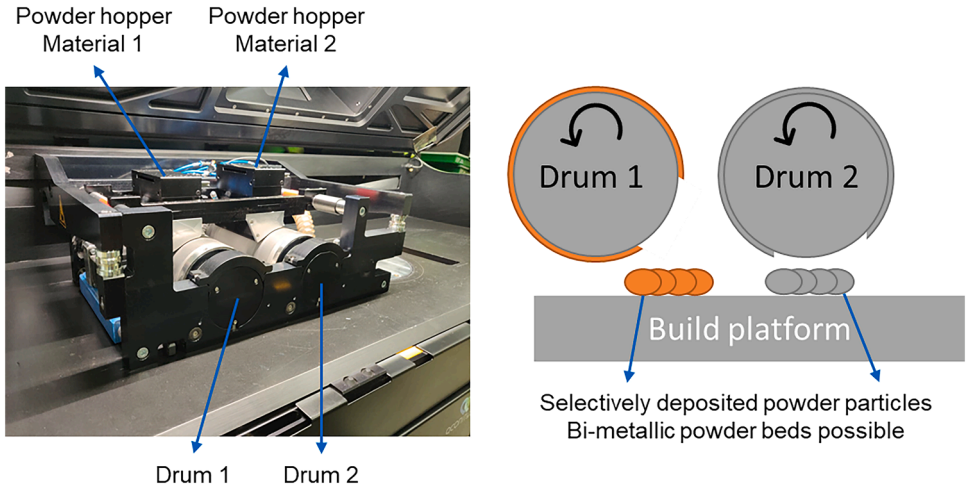


Fig. A.1. Selective powder deposition process performed by the Aeorisnt recoater: powder particles from powder hoppers stick to the surface of two rotating drums, due to a negative pressure inside them. These particles are ejected at the desired position onto the build platform to create a bi-metallic powder bed.

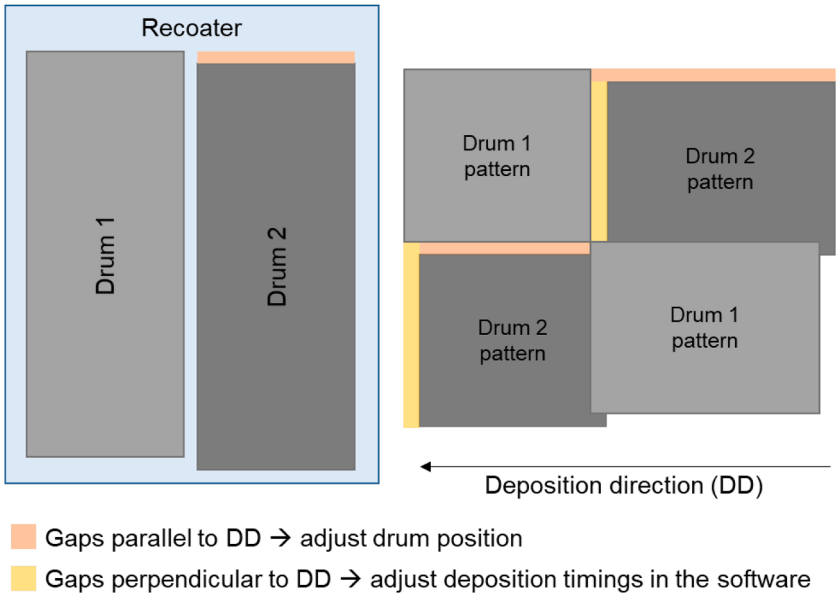


Fig. A.2. Powder alignment procedure: gaps parallel to the deposition direction (orange) can be fixed by manually adjusting the drum position forward or backward, while gaps perpendicular to the deposition direction (yellow) must be fixed by adjusting the deposition timings in the software (e.g., delay the deposition of drum 2 to shift its pattern to the left), as the position of the drums cannot be manually adjusted in the deposition direction.

APPENDIX B. Sample micrographs

Fig. B.1

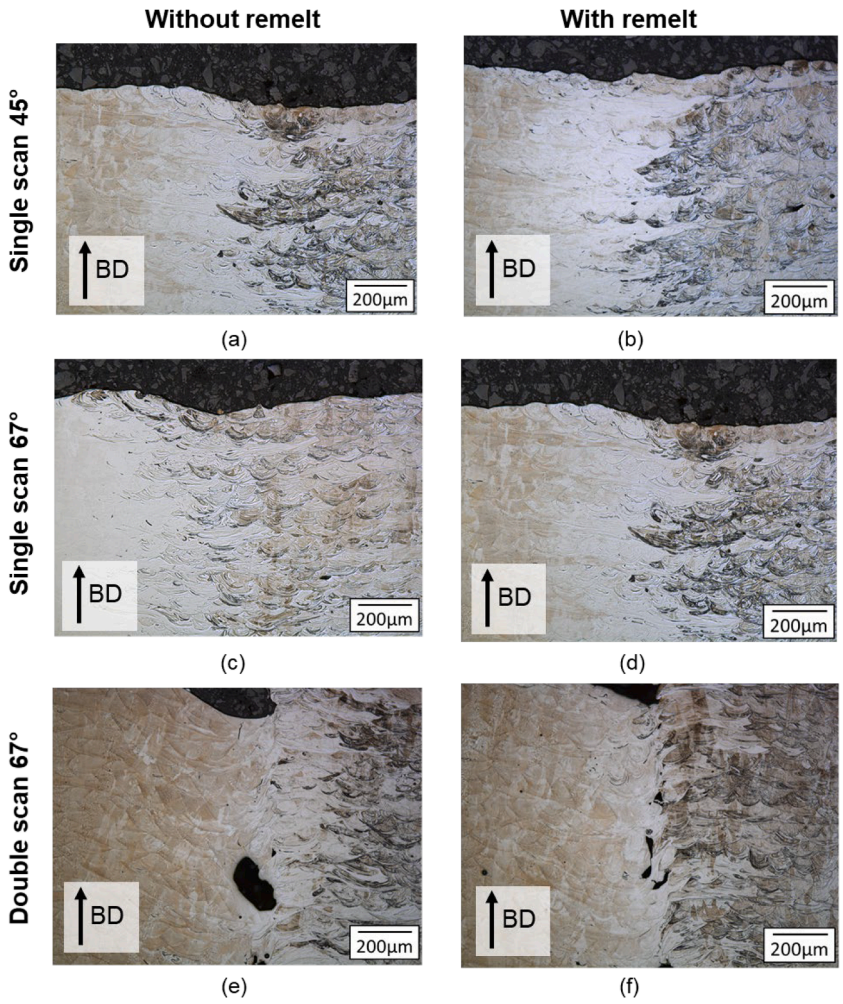


Fig. B.1. Micrographs of the interfaces of the six cuboids analyzed in this work.

Data availability

Data will be made available on request.

References

[1] M. Vaezi, S. Chianrabutra, B. Mellor, S. Yang, Multiple material additive manufacturing – Part 1: a review, Virtual. Phys. Prototyp. 8 (2013) 19–50, https://doi.org/10.1080/17452759.2013.778175.
[2] D. Han, H. Lee, Recent advances in multi-material additive manufacturing: methods and applications, Curr. Opin. Chem. Eng. 28 (2020) 158–166, https://doi.org/10.1016/j.coche.2020.03.004.
[3] L. Ai, X.-L. Gao, Metamaterials with negative Poisson's ratio and non-positive thermal expansion, Compos. Struct. 162 (2017) 70–84, https://doi.org/10.1016/j.compstruct.2016.11.056.
[4] J.S. Raminhos, J.P. Borges, A. Velhinho, Development of polymeric anepectic meshes: auxetic metamaterials with negative thermal expansion, Smart Mater. Struct. 28 (2019) 45010, https://doi.org/10.1088/1361-665X/ab034b.
[5] Y. Ding, M. Akbari, X.-L. Gao, L. Ai, R. Kovacevic, Use of a robotized laser powder-feed metal additive manufacturing system for fabricating metallic metamaterials, T.S. Srivatsan, T.S. Sudarshan, K. Manigandan. Manufacturing Techniques for Materials, CRC Press, 2018, pp. 51–65.
[6] Y. Ding, R. Kovacevic, Feasibility study on 3-D printing of metallic structural materials with robotized laser-based metal additive manufacturing, JOM 68 (2016) 1774–1779, https://doi.org/10.1007/s11837-016-1929-7.
[7] A. Mussatto, Research progress in multi-material laser-powder bed fusion additive manufacturing: a review of the state-of-the-art techniques for depositing multiple powders with spatial selectivity in a single layer, Results. Eng. 16 (2022) 100769, https://doi.org/10.1016/j.rineng.2022.100769.
[8] S.L. Sing, S. Huang, G.D. Goh, G.L. Goh, C.F. Tey, J. Tan, W.Y. Yeong, Emerging metallic systems for additive manufacturing: in-situ alloying and multi-metal processing in laser powder bed fusion, Prog. Mater. Sci. 119 (2021) 100795, https://doi.org/10.1016/j.pmatsci.2021.100795.
[9] B. Neirinck, X. Li, M. Hick, Powder deposition systems used in Powder bed-based multimetal additive manufacturing, Acc. Mater. Res. 2 (2021) 387–393, https://doi.org/10.1021/accountsmr.1c00030.
[10] M. Schneck, M. Horn, M. Schmitt, C. Seidel, G. Schlick, G. Reinhart, Review on additive hybrid- and multi-material-manufacturing of metals by powder bed fusion: state of technology and development potential, Prog Addit Manuf 6 (2021) 881–894, https://doi.org/10.1007/s40964-021-00205-2.
[11] Y. Bai, J. Zhang, C. Zhao, C. Li, H. Wang, Dual interfacial characterization and property in multi-material selective laser melting of 316L stainless steel and C52400 copper alloy, Mater. Charact. 167 (2020) 110489, https://doi.org/10.1016/j.matchar.2020.110489.
[12] K. Sertoglu, 3D Printing industry (3 October 2020).
[13] C. Anstaett, C. Seidel, G. Reinhart (Eds.), Fabrication of 3D multi-material parts using laser-based powder Bed fusion, 28th ed., 2017.
[14] M. Schneck, M. Horn, M. Schindler, C. Seidel, Capability of multi-material laser-based powder bed fusion—Development and analysis of a prototype large bore engine component, Metals. (Basel) 12 (2022) 44, https://doi.org/10.3390/met12010044.
[15] T. Stichel, T. Laumer, T. Baumüller, P. Amend, S. Roth, Powder layer preparation using vibration-controlled capillary steel nozzles for additive manufacturing, Phys. Procedia 56 (2014) 157–166, https://doi.org/10.1016/j.phpro.2014.08.158.
[16] J. Chen, Y. Yang, C. Song, M. Zhang, S. Wu, Wang Di, Interfacial microstructure and mechanical properties of 316L /CuSn10 multi-material bimetallic structure fabricated by selective laser melting, Mater. Sci. Eng, A 752 (2019) 75–85, https://doi.org/10.1016/j.msea.2019.02.097.
[17] P. Regenfuß, R. Ebert, H. Exner, Laser Micro Sintering – a versatile instrument for the generation of microparts, LTJ 4 (2007) 26–31, https://doi.org/10.1002/latj.200790139.
[18] T. Stichel, T. Laumer, P. Amend, S. Roth, Electrostatic multi-material powder deposition for simultaneous laser beam melting (2014).
[19] K. Chen, C. Wang, Q. Hong, S. Wen, Y. Zhou, C. Yan, Y. Shi, Selective laser melting 316L/CuSn10 multi-materials: processing optimization, interfacial characterization and mechanical property, J. Mater. Process. Technol. 283 (2020) 116701, https://doi.org/10.1016/j.jmatprotec.2020.116701.
[20] X. Mei, X. Wang, Y. Peng, H. Gu, G. Zhong, S. Yang, Interfacial characterization and mechanical properties of 316L stainless steel/inconel 718 manufactured by

selective laser melting, Mater. Sci. Eng A 758 (2019) 185–191, https://doi.org/10.1016/j.msea.2019.05.011.
[21] Z.H. Liu, D.Q. Zhang, S.L. Sing, C.K. Chua, L.E. Loh, Interfacial characterization of SLM parts in multi-material processing: metallurgical diffusion between 316L stainless steel and C18400 copper alloy, Mater. Charact. 94 (2014) 116–125, https://doi.org/10.1016/j.matchar.2014.05.001.
[22] X. Li, Z. Pan, L. Smolej, V. Karthik Nadimpalli, M. Moshiri, Towards manufacturing intra-layer multi-material mould tools with vertical interfaces using laser-based powder bed fusion, Mater. Des. 243 (2024) 113056, https://doi.org/10.1016/j.matdes.2024.113056.
[23] V. Errico, P. Posa, A. Fusco, A. Angelastro, S.Luisa Campanelli, Intralayer multi-material structure stainless-steel/nickel-superalloy fabricated via laser-powder bed fusion process, Manuf. Lett. 35 (2023) 11–15, https://doi.org/10.1016/j.mfglet.2022.11.004.
[24] L.N. Carter, C. Martin, P.J. Withers, M.M. Attallah, The influence of the laser scan strategy on grain structure and cracking behaviour in SLM powder-bed fabricated nickel superalloy, J. Alloys. Compd. 615 (2014) 338–347, https://doi.org/10.1016/j.jallcom.2014.06.172.
[25] T. Wegener, F. Brenne, A. Fischer, T. Möller, C. Hauck, S. Auernhammer, T. Niendorf, On the structural integrity of Fe-36Ni Invar alloy processed by selective laser melting, Addit. Manuf. 37 (2021) 101603, https://doi.org/10.1016/j.addma.2020.101603.
[26] C. Guillaume, Invar and its applications, Nature 71 (1904) 134–139, https://doi.org/10.1038/071134a0.
[27] L.J. Swartzendruber, V.P. Itkin, C.B. Alcock, The Fe-Ni (iron-nickel) system, JPE 12 (1991) 288–312, https://doi.org/10.1007/BF02649918.
[28] C.D. Lundin, Dissimilar metal Welds: transition Joints Literature Review, Welding Res. Supplement (1982) 58–63.
[29] T. Hanemann, L.N. Carter, M. Habschied, N.J. Adkins, M.M. Attallah, M. Heilmaier, In-situ alloying of AlSi10Mg+Si using selective Laser Melting to control the coefficient of thermal expansion, J. Alloys. Compd. 795 (2019) 8–18, https://doi.org/10.1016/j.jallcom.2019.04.260.
[30] A.S. Agazhanov, D.A. Samoshkin, Y.M. Kozlovskii, Thermophysical properties of Inconel 718 alloy, J. Phys.: Conf. Ser. 1382 (2019) 12175, https://doi.org/10.1088/1742-6596/1382/1/012175.
[31] R. Lakes, Cellular solids with tunable positive or negative thermal expansion of unbounded magnitude, Appl. Phys. Lett. 90 (2007) 221905, https://doi.org/10.1063/1.2743951.
[32] M.J. Matthews, G. Guss, S.A. Khairallah, A.M. Rubenchik, P.J. Depond, W.E. King, Denudation of metal powder layers in laser powder bed fusion processes, Acta Mater. 114 (2016) 33–42, https://doi.org/10.1016/j.actamat.2016.05.017.
[33] B. Attard, S. Cruchley, C. Beetz, M. Megahed, Y.L. Chiu, M.M. Attallah, Microstructural control during laser powder fusion to create graded microstructure Ni-superalloy components, Addit. Manuf. 36 (2020) 101432, https://doi.org/10.1016/j.addma.2020.101432.
[34] G.H. Cao, T.Y. Sun, C.H. Wang, X. Li, M. Liu, Z.X. Zhang, P.F. Hu, A.M. Russell, R. Schneider, D. Gerthsen, Z.J. Zhou, C.P. Li, G.F. Chen, Investigations of γ′, γ″ and δ precipitates in heat-treated Inconel 718 alloy fabricated by selective laser melting, Mater. Charact. 136 (2018) 398–406, https://doi.org/10.1016/j.matchar.2018.01.006.
[35] E. Hosseini, V.A. Popovich, A review of mechanical properties of additively manufactured Inconel 718, Addit. Manuf. 30 (2019) 100877, https://doi.org/10.1016/j.addma.2019.100877.
[36] W. Huang, Z. Wang, Isothermal solid-State transformations of inconel 718 alloy fabricated by selective laser melting, Adv. Eng. Mater. 23 (2021) 2000982, https://doi.org/10.1002/adem.202000982.
[37] J. Schneider, B. Lund, M. Fullen, Effect of heat treatment variations on the mechanical properties of Inconel 718 selective laser melted specimens, Addit. Manuf. 21 (2018) 248–254, https://doi.org/10.1016/j.addma.2018.03.005.
[38] J. Schröder, T. Mishurova, T. Fritsch, I. Serrano-Munoz, A. Evans, M. Sprengel, M. Klaus, C. Genzel, J. Schneider, G. Bruno, On the influence of heat treatment on microstructure and mechanical behavior of laser powder bed fused Inconel 718, Mater. Sci. Eng. A 805 (2021) 140555, https://doi.org/10.1016/j.msea.2020.140555.
[39] S. Imbrogno, A. Alhuzaim, M.M. Attallah, Influence of the laser source pulsing frequency on the direct laser deposited Inconel 718 thin walls, J. Alloys. Compd. 856 (2021) 158095, https://doi.org/10.1016/j.jallcom.2020.158095.
[40] E. Yasa, J. Deckers, J.-P. Kruth, The investigation of the influence of laser re-melting on density, surface quality and microstructure of selective laser melting parts, Rapid. Prototyp. J. 17 (2011) 312–327, https://doi.org/10.1108/13552541111156450.
[41] E.G. Brodie, A.E. Medvedev, J.E. Frith, M.S. Dargusch, H.L. Fraser, A. Molotnikov, Remelt processing and microstructure of selective laser melted Ti25Ta, J. Alloys. Compd. 820 (2020) 153082, https://doi.org/10.1016/j.jallcom.2019.153082.

Publication {2}

Prediction of the negative thermal expansion behavior of metallic metamaterials printed via bi-material laser-based powder bed fusion

Prestes, I.B., Buchmann, E., Höfer, P., Jägle E.A.

Materials & Design 256 (2025) 114276

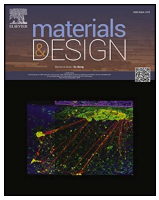
Materials & Design 256 (2025) 114276



Contents lists available at ScienceDirect

Materials & Design

journal homepage: www.elsevier.com/locate/matdes



Prediction of the negative thermal expansion behavior of metallic metamaterials printed via bi-material laser-based powder bed fusion

I.B. Prestes [a,*], E. Buchmann [b], P. Höfer [b], E.A. Jägle [a]

[a] Institute of Materials Science, Universität der Bundeswehr München, Neubiberg, Germany
[b] Institute of Lightweight Engineering, Universität der Bundeswehr München, Neubiberg, Germany

ARTICLE INFO

Keywords:
Negative CTE
Metamaterials
Multi-material PBF-LB
Aerosint recoater
Dilatometry
FEM Simulations

ABSTRACT

Metamaterials designed to present a negative thermal expansion are bi-material lattice structures. The influence of their unit cell geometry on the coefficient of thermal expansion (CTE) has been simulated in the last decades and good agreement with experimentally obtained CTEs of metamaterials fabricated via bi-material additive manufacturing has been found. However, up to now, neither a bi-metallic combination that allows a wide range of CTEs to be tuned, nor a thorough understanding of the metamaterial's behavior, including at cryogenic temperatures, has been presented. In this work, we present simulations and experimentally obtained CTEs of bi-metallic metamaterial unit cells and multi-unit-cell structures. Unit cells with different geometric features are manufactured of Invar and Inconel 718 by laser-based powder bed fusion. Unit cells based on triangles with low angles lead to CTEs of up to -37×10^{-6}/K, but are sensitive to geometric features which influence the hinge stiffness and may significantly increase their CTE, such as strut thickness and offset between base and side. A good match between the simulations and dilatometry measurements was achieved by manufacturing a multi-unit-cell segment of the metamaterial and selecting the corresponding boundary conditions for finite element simulations, allowing the prediction of the expansion behavior of future metamaterials.

1. Introduction

The coefficient of thermal expansion (CTE) is an important material property to be considered in applications where components are subjected to high temperature variations, especially if they require high dimensional accuracy at the same time [1–3]. This condition applies to satellite and aerospace components, such as high-precision space optical systems and telescope mirrors, for example [4–6]. Therefore, metamaterials with controllable CTE have been proposed and studied in the last decades. These metamaterials combine two different materials in a specific lattice structure, usually inspired by auxetic metamaterials, to achieve a desired CTE, which can be tuned from large positive to negative values [1,7–9]. Tunable CTEs can be applied in thermal actuators and a negative thermal expansion (NTE) is of special interest to compensate the thermal expansion of conventional materials [3,10–12].

Possible mechanisms to achieve an NTE are: combining the two materials in bi-layer strips, re-entrant structures, triangle, or tetrahedral structures or even more complex geometries, conceptualized via topology optimization [7,8,13–15]. In any of these, the choice of the composing materials and the geometry of the unit cell of the metamaterial is crucial not only to achieve a desired stiffness, but also a desired CTE. A larger CTE difference between the two materials will lead to a larger NTE [8–10,16].

Many works on simulations of NTE metamaterials have predicted their behavior and optimized their geometries [2,7,10,15,17–23]. However, only in the past decade, these concepts were experimentally validated by assessing the thermal expansion of bi-material structures fabricated either by conventional methods, such as gluing [24], laser spot welding [25], bolting [11], interference fitting [26] or snap fitting [27] to combine the materials, or by multi-material additive manufacturing (AM) [12,14,16,28–33]. Most of the works on printed NTE metamaterials were done in polymer AM processes [12,14,16,28–30]. The bi-polymeric metamaterials printed by Wang et al. [14] and the unit cells printed by Wei et al. [30] have shown a good agreement with their respective simulations. In the recent years, multi-material AM processes based on metals became unavailable [34], allowing NTE structures to be built: (1) with higher stiffness than the ones with polymer materials, enlarging the applications range and (2) with smaller feature size than the ones fabricated by conventional manufacturing – e.g. bolting material rods together.

* Corresponding author.
E-mail address: isabel.prestes@unibw.de (I.B. Prestes).

https://doi.org/10.1016/j.matdes.2025.114276
Received 28 February 2025; Received in revised form 24 April 2025; Accepted 19 June 2025
Available online 20 June 2025
0264-1275/© 2025 The Author(s). Published by Elsevier Ltd. This is an open access article under the CC BY license (http://creativecommons.org/licenses/by/4.0/).

Although metallic structures would be more suitable for applications that require a higher stiffness than polymers, bi-metallic AM for printing metamaterials with tunable CTE has not been widely investigated. Ding et al. [31] printed different metallic metamaterials made of Invar and stainless steel using laser-based directed energy deposition (DED), but did not evaluate their CTE. Parsons [33] printed alternating layers of aluminum and titanium by means of ultrasonic AM (UAM) and metamaterials were cut from them by electrical discharge machining (EDM). A negative CTE was achieved and has shown good correlation with simulations, but only one metamaterial geometry with this property was investigated. Bambach and Tucker [32] printed metamaterials made of 316L and CuCrZr with bi-material laser-based powder bed fusion (PBF-LB/M) process, which allows finer and more accurate structures to be built in comparison with the DED process and would not be restricted to bi-metallic alternating layers as in the UAM process. However, this material combination did not allow negative CTEs to be achieved, led to cracks at the bi-material interface and there were mismatches between simulated and measured CTE. Moreover, the CTE of the metamaterials in these works was observed only in temperature ranges starting from room temperature and therefore not considering negative temperatures, which would be important for space applications.

Up to now, no reported literature has shown a printed metallic NTE structure that has: (1) presented a good match between simulations and dilatometer measurements, (2) measured their CTE at cryogenic temperatures, which would be useful for applications in aerospace industry and (3) chosen a combination of materials that allow a wide range of CTE to be tuned. In this work, metallic NTE metamaterials made of Invar and Inconel 718 were manufactured via bi-material PBF-LB/M. Different unit cell geometries and metamaterial sections were investigated to achieve a good correlation with the simulated CTE, thus approaching a reliable prediction of the metamaterials' CTE.

2. Materials and methods

2.1. Design of the metamaterials

In this work, metamaterial structures that present a negative CTE in one direction were modelled, simulated, printed and had their CTE measured in a dilatometer. The negative CTE was achieved by combining Invar and Inconel 718 in a structure based on triangle shapes, as exemplified in Fig. 1. The increase in temperature makes the base of the triangle, which is made of Inconel 718, expand more than its sides, made of Invar. This changes the angles in the triangle, making the contact between the two materials a compliant hinge.[1] This induces a shrinkage in the triangle's height and, thus, leads to a negative CTE in the Y-direction. By stacking these triangles together on top of and next to each other, as shown in Fig. 1, an NTE metamaterial is built.

The material combination of Invar and Inconel 718 was chosen due to: (1) the large difference of their CTE values, which is essential to obtain NTE metamaterials [16] and (2) their metallurgical compatibility, which allows them to be printed together in a bi-metallic PBF-LB process without defects, such as cracks and pores, at their interfaces [35]. The measured CTEs of the materials used in this work will be presented in section 3.1 and a more detailed explanation of the manufacturing process is written in section 2.4.

2.2. Modelling

The metamaterials were modelled in the CAD software Rhino 7 SR37 and specific geometric features, presented in Fig. 2a, were modified to create different unit cell geometries, such as the angle θ of the triangle, thickness t of the struts in the XY-plane and the offset o between the triangle's base and its sides. Initially, many unit cell geometries were modelled for FEM simulations (cf. section 2.3), in order to understand the influence of these geometric features on the metamaterials' CTE. For that, a full parameter study was done by varying thickness and offset in 2 levels and angle in 5 levels, as detailed in Table 1. The base b was kept constant at 20 mm for all of them. Based on the study's results, some unit cells were selected to be printed and are detailed in Table 2 and represented graphically in Fig. 2b. The modelling of these structures was first done in 2D and then they were extruded 6 mm in Z-direction to be simulated and printed.

The structures in Fig. 2a and b represent unit cells of a larger metamaterial, as shown in Fig. 2c for one particular example. Due to geometry constraints imposed by the manufacturing process and the dilatometer measuring system, which will be explained in section 2.4 and section 2.5, measurement of the CTE of a metamaterial with many unit cells would not be feasible. Therefore, segments of the metamaterial, as shown schematically in Fig. 2c, were selected for printing the structures described in Table 2. These segments will be henceforth called *X-unit cell* and *triangle-unit cell*. In the case of structure C, which presented a good agreement with the simulations, these two types of unit cells were also arranged into larger structures, by combining them into a 2x1 matrix or a 2x2 matrix of unit cells, also illustrated in Fig. 2c.

In order to indicate which type of unit cell is being analyzed and discussed in this paper, suffixes will be added to the name of the structures accordingly. The suffix "*-X*" and "*-T*" represent X unit cell and triangle unit cell, respectively. Structure A-X, for example, is a unit cell with the geometric features of structure A, described in Table 2, modelled as a X unit cell.

2.3. Simulations

The structures were simulated in the thermomechanical Finite Element Model implemented in the "Static Structural Module" of Ansys Workbench 2023 R2. The material properties of Invar and Inconel 718 from the software database were not modified, except for their CTE, which was replaced by the measured CTE values as function of temperature of the printed bulk materials.

The X- and triangle-unit cells were simulated either by applying periodic boundary conditions, which repeat the unit cell infinitely in the Y-direction, or without constraints, which allows the unit cell to bulge freely (both conditions are shown schematically in Fig. 3a). In the latter case, the bulging direction switches at 20 °C (where the unit cells are assumed to be in idealized geometry): for temperatures below 20 °C, X-unit cells present a convex bulging, whereas above 20 °C, this bulging condition switches to concave. The opposite happens to the triangle unit cell, which switches from concave to convex bulging at 20 °C. This phenomenon was observed in simulations and confirmed experimentally, via digital image correlation (DIC), as shown in Fig. 3b and c, respectively. This bulging occurs because of an elastic effect. Both materials alone present a positive CTE, meaning that they will contract at temperatures lower than a reference temperature and expand at temperatures higher than this reference temperature. However, since Inconel 718 has a much larger CTE than Invar, its contractions and expansions are much more prominent than Invar's. Therefore, at low temperatures, the triangle's base (made of Inconel 718) tends to shrink more than its sides (made of Invar) and the opposite happens at high temperatures.

In a metamaterial, the unit cells would be surrounded by many others, hence having their bulging restricted, which is the situation aimed to be simulated by the periodic boundary condition. Therefore, these simulations will henceforth be called *metamaterial simulations*. However, due to the dimensional constraints of the dilatometer measuring system, single unit cells were printed and analyzed despite the bulging phenomenon which is not representative for metamaterials. The corresponding simulations without periodic boundary conditions

[1] The joints are compliant since the struts are quite thin and thus the material deforms elastically. The word "hinge" is not meant to imply two interlocking structures.

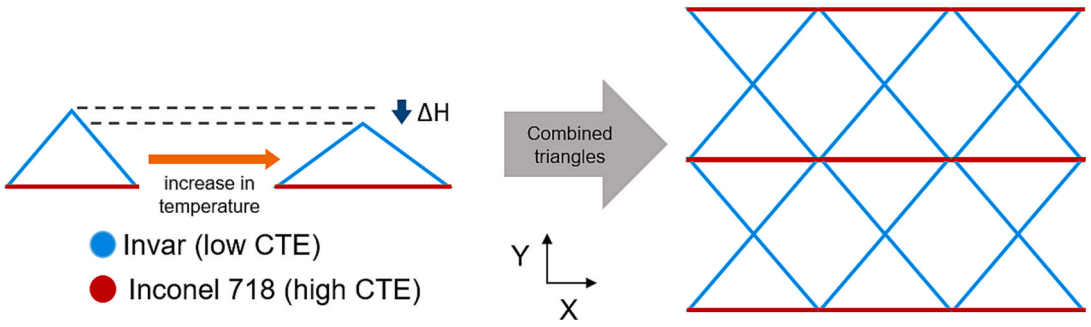


Fig. 1. Schematic of the mechanism to achieve a negative CTE in Y-direction. The increase in temperature leads to a larger expansion of the triangle's base, which is composed by the material with higher CTE (Inconel 718), rotating the triangle's sides made of a material with lower CTE (Invar) and inducing a reduction in the triangle's height, thus a shrinkage, in Y-direction. The combination of multiple triangles in X- and Y-direction creates an NTE metamaterial.

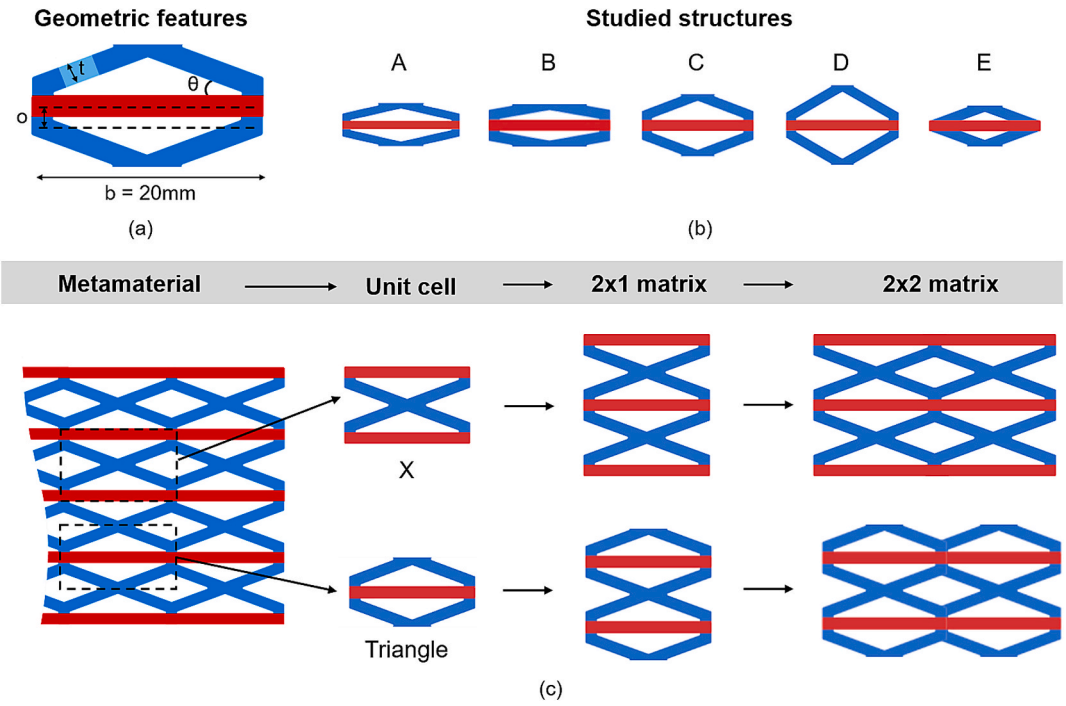


Fig. 2. Description of the structures studied in this work: (a) geometric features of the metamaterial structures that were varied: angle θ of the triangle, thickness *t* of the trusses and offset *o* between the triangle's base and sides; (b) representation of structures A to E, detailed in Table 2; and (c) selection of two different unit cells of a larger metamaterial: X- and triangle-unit cells, which can be combined into a 2x1 matrix or a 2x2 matrix of unit cells for the dilatometer measurements.

Table 1
Levels of the three factors simulated in the parameter study.

Level	Factor Angle θ [°]	Thickness t [mm]	Offset o [mm]
1	10	1.5	0
2	20	2	2
3	30	–	–
4	40	–	–
5	50	–	–

Table 2
Geometric features of the structures studied in this work.

Structure	Angle θ [°]	Thickness t [mm]	Offset o [mm]	L_0 X unit cell [mm]	L_0 Triangle unit cell [mm]
A	10	1.5	2	9.02	7.52
B	10	2	2	9.52	7.52
C	20	2	2	13.40	11.40
D	30	2	2	17.60	15.60
E	20	2	0	9.40	7.40

will henceforth be called *unit cell simulations*.

All parts in both simulations were subjected to a linear temperature variation from −100 °C to 260 °C. At the end of the simulation, the length variation ΔL of the unit cells in temperature intervals of 12 °C was extracted and the CTE was calculated by the Equation (1). Examples of the ΔL and CTE curves obtained from the simulations are shown in Fig. 3d. The switch in bulging direction at 20 °C in the unit cell simulation is captured as a kink in the ΔL curve, i.e. a change in the length variation rate, and as a "jump" in the CTE curve.

$$CTE = \frac{1}{L_0} * \frac{dL}{dT} \quad (1)$$

In the metamaterial simulations, ΔL was taken by subtracting the displacement between the top and bottom surfaces of the unit cells,

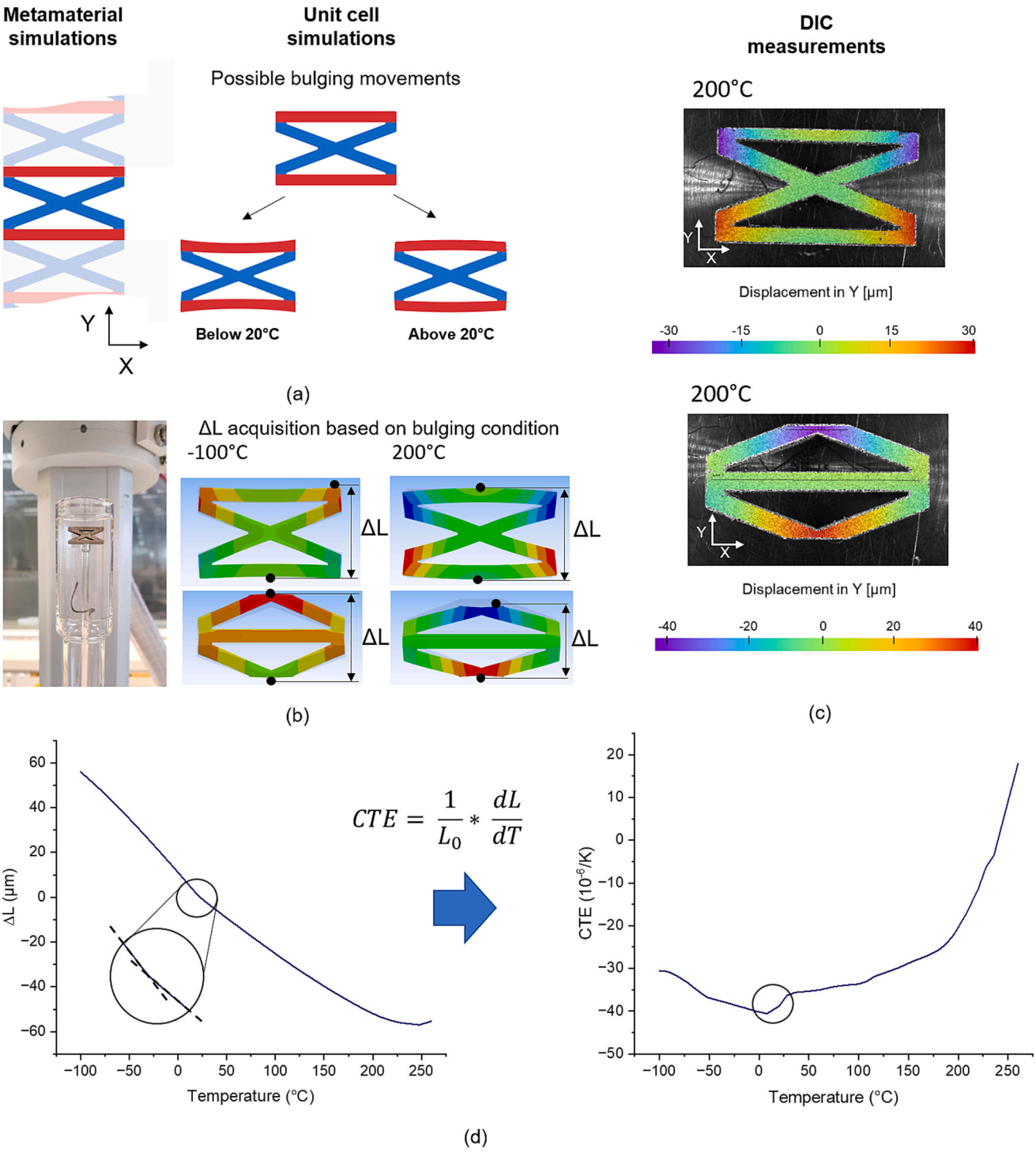


Fig. 3. (a) Different types of condition for the simulations: metamaterial simulation, with periodic boundary conditions, in which the unit cell is repeated infinitely in Y-direction, and unit cell simulation, done without periodic boundary conditions, allowing the unit cell to bulge freely. (b) Acquisition of the ΔL from the simulations based on the dilatometer setup and bulging direction; (c) Evidence of the bulging effect captured in DIC: C-X (top) showing concave bulging and C-T (bottom) showing convex bulging at 200 °C; (d) Example of ΔL curve obtained by the simulations and the CTE curve obtained by its derivative (in this case, from structure C-T): the switch in bulging direction is captured as a kink in the ΔL curve at 20 °C, which creates a "jump" in the CTE curve.

while in the unit cell simulations, ΔL was measured in a way that would best represent the dilatometer measurements. The printed unit cells' top surface was entirely in contact with the dilatometer's measuring system, but their bottom surface was in contact only to the dilatometer's push-rod. Therefore, the simulated ΔL in this work was always measured by subtracting the displacement of the topmost node to the bottom center node, as shown in Fig. 3b for both unit cells, so it could be compared to the measured data.

2.4. Bi-material additive manufacturing

The structures in this work were manufactured via bi-material laser powder bed fusion (PBF-LB/M), performed in an Aconity MIDI + machine equipped with a selective powder deposition recoater developed

by Schaeffler Aerosint (Fig. 4a). The recoater allows the deposition of two different materials in the same deposited layer, thus enabling a 3D-multi-material process. As an example, with visually easily distinguishable powders, in Fig. 4b, printed parts in a CuCrZr and Invar powder bed are shown. In Fig. 4c, bi-metallic printed parts using the material combination of this work (Inconel 718 and Invar) are shown. Each powder is deposited by a patterning drum, that, controlled by a computer, ejects particles onto the powder bed according to the desired pixel-by-pixel powder pattern of each layer. The pixel size is 0.5x0.5 mm^2, which defines the recoater resolution and restricts the minimum feature size to be printed to ca. 1 mm. For this reason, the metamaterials (i.e. structures composed of three or more unit cells in either direction), could not be shrunk as much as needed to fit in the dilatometer measuring system, which has a maximum diameter of 30 mm.

The Invar and Inconel 718 powders used in the process were provided by Linde, were gas atomized and had a particle size range of 15–45 μm. The parts were printed under argon using a stripe hatching strategy with 5 mm wide stripes. The PBF-LB/M parameters were kept the same for both materials, allowing the use of a single scan strategy (i.e. both materials are printed simultaneously, without interrupting the laser path at the interface), which avoids formation of cracks and pores at the materials' interface, as we have observed in our previous study [35]. The previously optimized PBF-LB/M parameters were: laser power of 180 W; scanning speed of 940 mm/s; angle increment per layer of 67°; hatch spacing and laser spot size of 80 μ m; and a layer thickness of 40 μ m. The single material samples printed in this work were printed with the same PBF-LB/M parameters, but in the usual single material PBF-LB/M setup, i.e. without the multi-material recoater.

After the AM process, the samples were cut from the base plate by electrical discharge machining. The metamaterial 2x2 matrices, that are shown in Fig. 4c, had their size reduced to 64 % to fit into the dilatometer measuring system.

2.5. Dilatometry

The dilatometry measurements of this work were performed in a vertical pushrod dilatometer model L75 by Linseis, equipped with a low temperature system that can be heated as well as cooled by liquid nitrogen. The dilatometer can be operated with several measuring systems (i.e. sample measurement chambers), including one for samples with a diameter up to 30 mm, which allowed the measurement of the unit cells and metamaterials of 2x1 and 2x2 matrices (cf. Fig. 2c). The length of the printed samples (L_0 in Equation (1)) was measured with a caliper prior to the thermal cycle.

The samples were first heated up to 250 °C followed by two cooling cycles and two heating cycles that ranged from −100 °C to 250 °C, with cooling and heating rates of 2.5 °C/min. The repetition of the cooling and heating cycles was done to check repeatability of the results and guarantee that the dilatometer was operating in a steady-state mode. The samples were measured under helium atmosphere with a gas flow of 10 cm^3/min. Prior to the measurements of the structures, a correction measurement was performed with a quartz reference sample under the same thermal cycle.

The structures in this work were placed into the dilatometer as shown in Fig. 3b: with the dilatometer pushrod placed directly at the sample's base (with a contact force of 400mN) and the sample's top directly in contact with the measuring system. Due to its geometry, that would not allow the push rod to be placed at its center, the triangle 2x2 matrix was measured with an additional quartz base plate beneath it.

In this work, not only bi-material samples were measured, but also single material samples. At first, single material cylinders of printed Inconel 718 and Invar had their CTEs measured (using a standard measurement system for small specimens) to use them as input for the simulations. Later, some single material unit cells were measured to check if the dilatation signal acquired using the large measuring system was in accordance with what had been measured in the standard measuring system.

3. Results

3.1. Dilatometry of single materials

The measured CTEs of as-printed Inconel 718 and Invar specimens are presented in Fig. 5a and b, respectively. The CTE curves of the cylindrical samples and the single-material structures E-X are very similar, which assures the reliability of the data acquired by the larger measuring system.

The slightly negative CTE measured in the Invar samples may be due to residual stresses from the AM process [36]. An Invar sample that was stress relieved at 850 °C for 1 h showed positive CTE values close to zero (not shown here). However, since the bi-material structures in this paper were measured as-printed, the measured CTE values as a function of temperature (Fig. 5) are used for the subsequent thermo-mechanical FEM simulations.

3.2. Parameter study simulations

In Fig. 6, the results of the parameter study of the unit cells in the two different FEM simulation boundary conditions are shown: in Fig. 6a, the unit cell simulation and in Fig. 6b, the metamaterial simulation. The CTE values plotted correspond to the simulated CTE at 50 °C. While the CTE values differ significantly by changing the offset and the thickness at low angles θ, they tend to converge at angles above 40°. Similarly, at low angles, the unit cell simulation yields lower CTE values than the metamaterial simulation, but, again, at larger angles, these values become comparable. The structures A to E that were printed are highlighted in

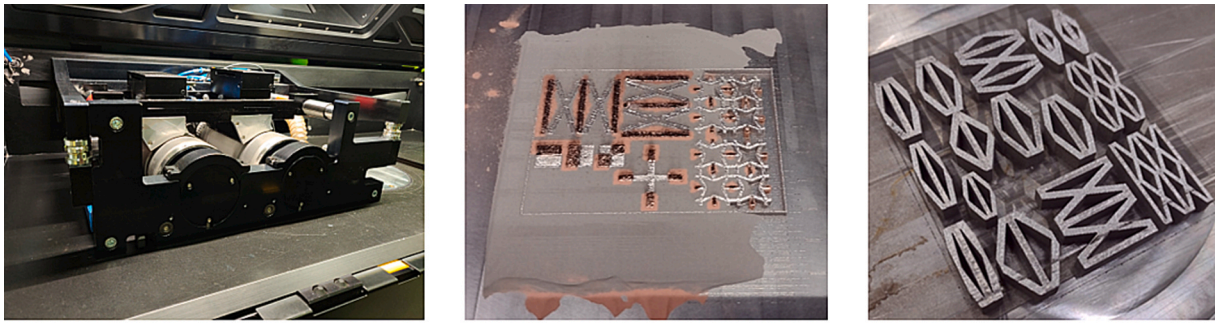


Fig. 4. (a) Selective powder deposition recoater developed by Schaefller Aerosint, with two patterning drums; (b) Example of build job printed with two different materials, showing a part of the powder bed with two different powders deposited in the same layer; and (c) Picture of a build job performed for this work with the Invar + Inconel 718 combination.

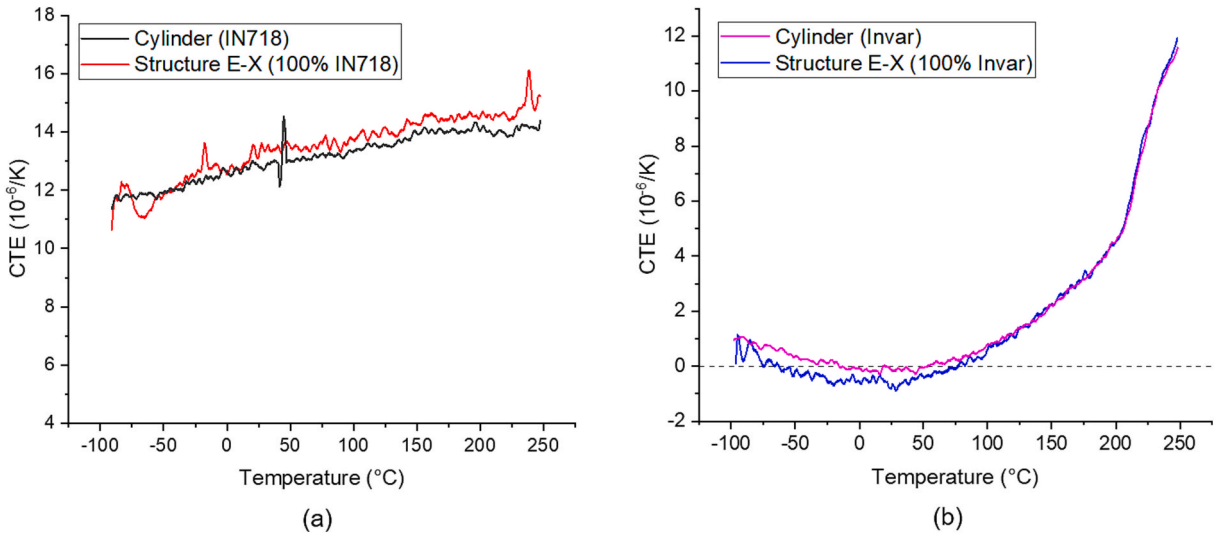


Fig. 5. CTE of as-printed single material cylinders and structures E-X made of: (a) IN718 and (b) Invar.

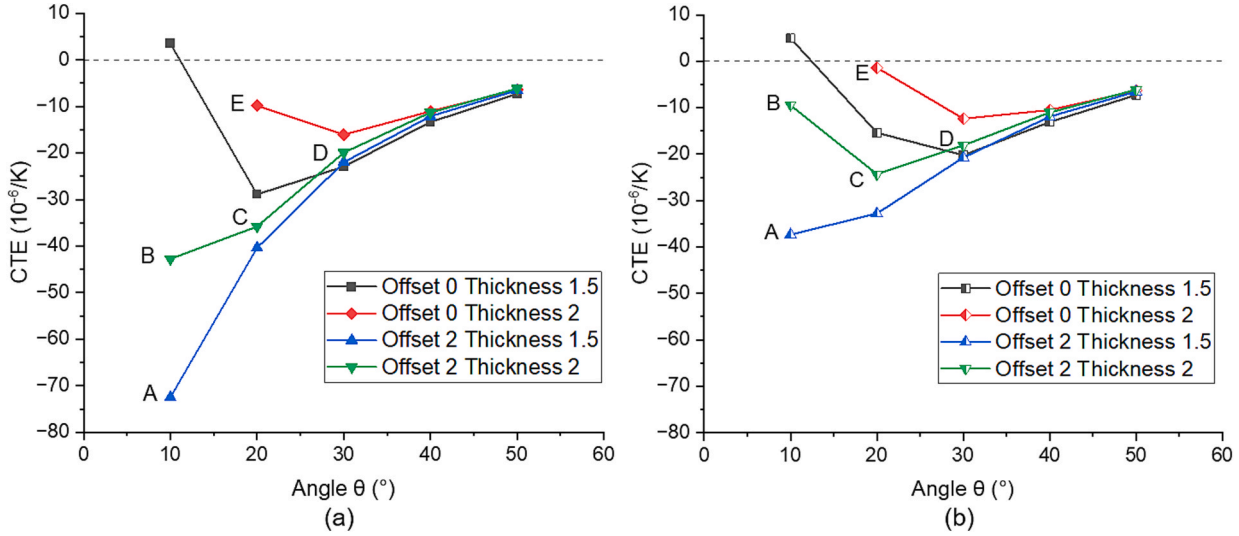


Fig. 6. Simulated CTE of triangle unit cells at 50 °C with: (a) unit cell simulation and (b) metamaterial simulation. The structures A to E, that were printed, are labeled in both graphs.

the plot. They were chosen to represent various geometries that span a large range of negative CTEs, different angles, thicknesses, and offsets.

3.3. Structures A to E

3.3.1. Simulations

In Fig. 7a and b, the CTE of the structures A-X to E-X simulated according to the unit cell and metamaterial conditions are shown, respectively. As represented in Fig. 3d, the "jumps" in the CTE curve of the unit cell simulations (Fig. 7a) come from kinks in the length variation curve, caused by the bulging effect of the unit cells, which changes its direction at the temperature of 20 °C. As the bulging effect gets restricted when applying the metamaterial simulation's periodic boundary conditions, the CTE curves of the structures become smooth, as can be seen in Fig. 7b. The CTE curves of the unit cell simulation and the metamaterial simulation differ not only in shape, but also in values. Structure B-X, for example, should present a positive CTE for the entire temperature range in the unit cell simulation, but presents a negative CTE in the metamaterial simulation. Structure E-X, on the other hand, presents one of the lowest and negative CTE from −100 °C to 20 °C in the unit cell simulation, but presents a slightly positive CTE in the metamaterial simulation.

A similar behavior is identified when simulating the triangle unit cells, whose CTE curves of unit cell and metamaterial simulations are presented in Fig. 7c and d, respectively. Except for the jumps at 20 °C, the shape of the CTE curves of the triangle structures do not change much from unit cell simulations to metamaterial simulations, but the CTE values are considerably lower when the structures are simulated using the unit cell condition. Moreover, a less pronounced bulging effect is observed in the triangle unit cells in comparison to the X-unit cells discussed before, which is evidenced by the shorter CTE jumps in Fig. 7d.

Although an identical behavior would have been expected for both type of unit cells in the metamaterial simulations, i.e. Fig. 7b and d, the CTE of the triangle unit cells are lower. This can be explained by their lower Inconel 718 content: the triangle unit cells are composed of a single beam made of Inconel 718, while the X unit cells are composed by 2 beams of this material, which increases the overall CTE.

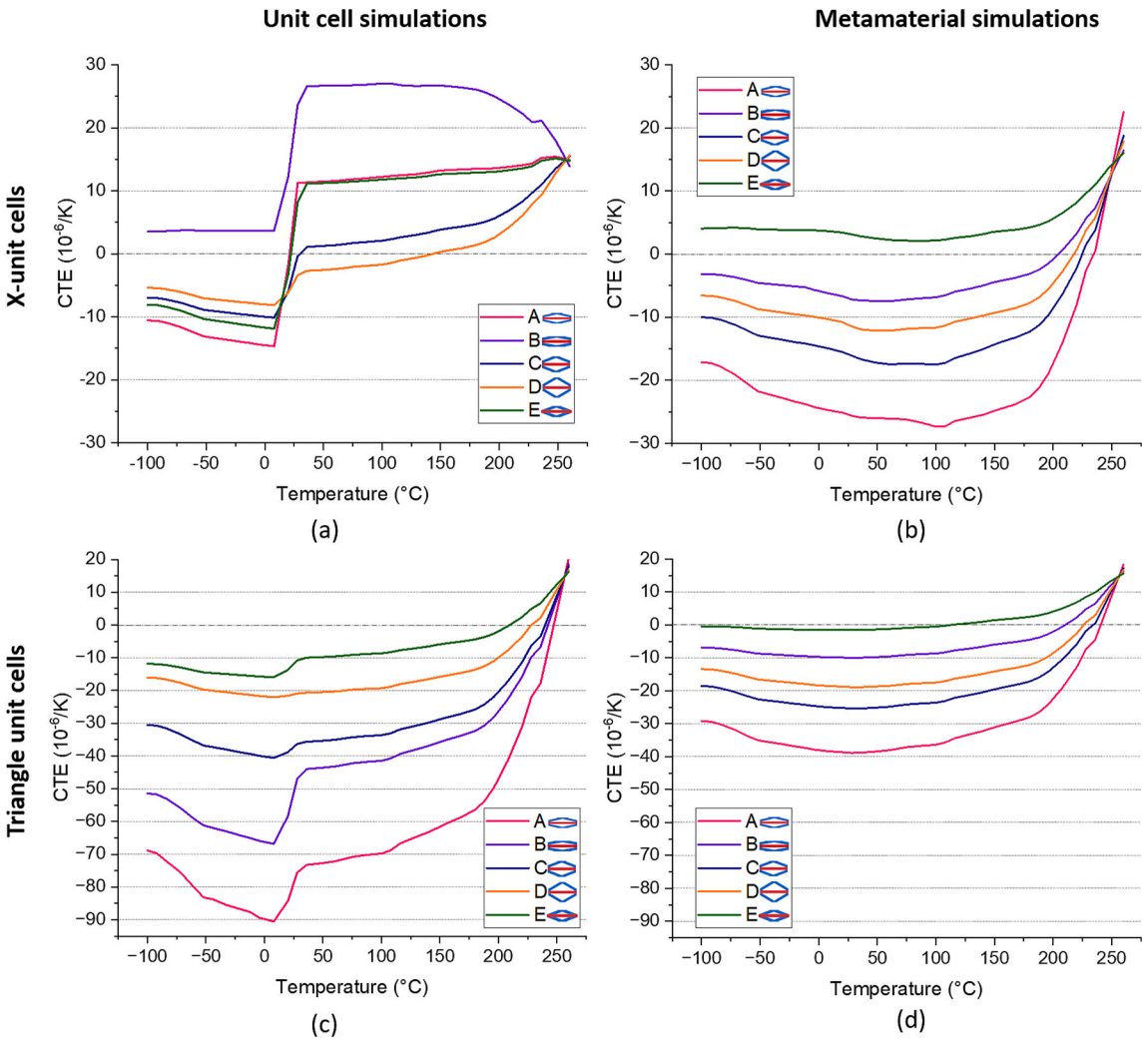


Fig. 7. Simulation results: (a) CTE of the X-unit cells according to the unit cell boundary conditions, with a "jump" in the curve, where the bulging direction switches; (b) CTE of these structures according to the metamaterial boundary conditions, without any "jump" in the CTE curve; (b) CTE curve of the triangle unit cells according to the unit cell simulation, with "jumps" in the curve; and (d) according to the metamaterial simulation, without any "jumps".

3.3.2. *X unit cells*

The measured CTE of the X-unit cells are shown in Fig. 8a, together with the unit cell simulation results, in dashed lines. The measured CTE curves present jumps along the temperature cycle, except for structure D-X. These jumps were expected at 20 °C due to the bulging effect, as it was predicted in the simulations. However, in the measured data, these jumps appeared more than once in some cases and not exactly at the temperature of 20 °C. Although the kinks in the ΔL curve and, consequently, the jumps in the CTE, were repeatable at the same temperature and in the same intensity along a measurement cycle, they were not reproducible after the sample was taken out and put back again into the dilatometer. The kinks in the ΔL curve of the structure E-X are highlighted by the pointed lines 1,2 and 3 in Fig. 8b and their respective jumps are indicated by the black line and the arrows 1, 2 and 3 in Fig. 8c. However, the purple line in Fig. 8c, which represents a different measurement cycle, s not present the same jumps. Presumably, they are the result of the large specimens being in a stick–slip contact with the dilatometer pushrod and back wall. Nevertheless, at temperatures higher and lower than the jumps in CTE (e.g. above 125 °C and below −50 °C), the measurements show relatively good agreement with the simulations.

3.3.3. *Triangle unit cells*

The CTE curves of the triangle unit cells are presented in Fig. 9 and can be compared with the simulations in dashed lines. In general, the measured CTE curves present a good match with the simulations and the CTE jumps, when present, appear only once at the temperature of 20 °C due to the change in the bulging direction, as calculated by the simulations (Fig. 3). Clearly triangle unit cells are better suited for determining the CTE of such structures because they minimize the bulging effect.

3.3.4. *Metamaterials*

The CTE of the metamaterial matrices are plotted in Fig. 10a, together with the CTE curves of their unit cells, C-T and C-X, respectively. The structure C-T with a 64 % size reduction is also plotted for comparison, since the matrices 2x2 were reduced as well to fit the dilatometer's measurement system. The size reduction did not considerably affect the CTE of the C-T structure, so it is possible to compare the results of the reduced 2x2 matrices with the 2x1 matrix and the unit cell.

The CTE curves as result of FEM simulations of C-T and C-X using the metamaterial and unit cell boundary conditions are plotted in dashed lines. To allow for an easier comparison between measured and simulated CTE values, in Fig. 10b, the data from Fig. 10a at the temperature of 50 °C is plotted as a predicted vs. observed values graph. The straight line indicates a perfect match between simulation and measurement, while the points represent the measured CTE values at this temperature for each of the printed structures, which are color-coded the same way as

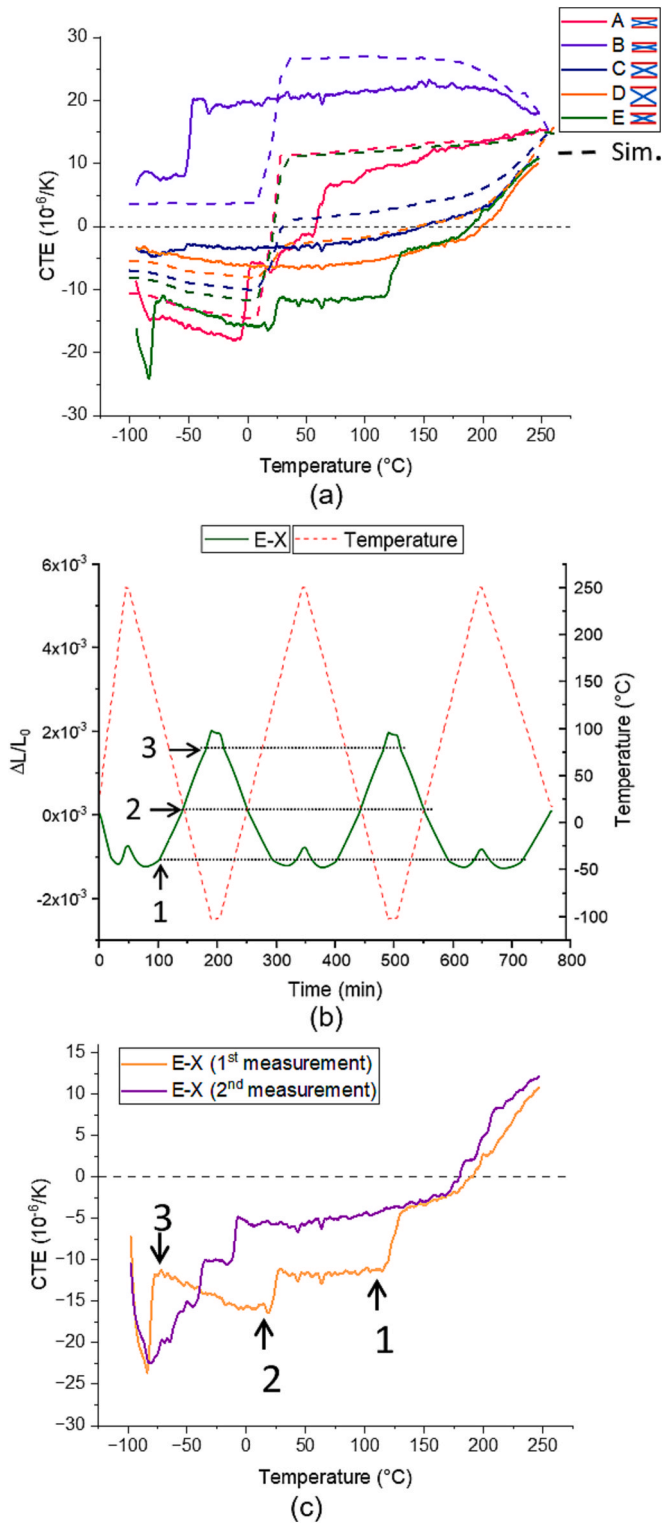


Fig. 8. Dilatometry results of the X-unit cell structures: (a) measured CTE of the A- to E-X structures, compared with their simulations, in same color, but in dashed lines; (b) $\Delta L/L_0$ curve of structure E-X along the entire cycle, with the pointed lines 1, 2 and 3 showing kinks that were reproducible at the same temperatures and (c) CTE curves of structure E-X measured in different days; the kinks 1,2 and 3 of the $\Delta L/L_0$ curve appear as jumps in the black CTE curve.

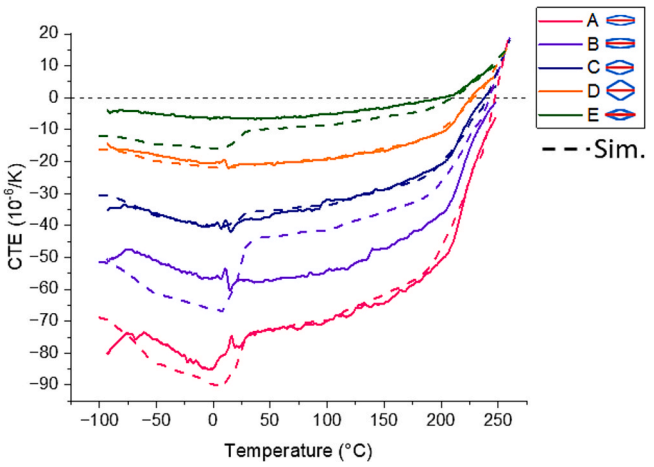


Fig. 9. Dilatometry results of the triangle-unit cell structures, compared with their simulations, in same color, but in dashed lines.

in Fig. 10a. The temperature of 50 °C was arbitrarily chosen, as it is not within the range where a CTE jump could happen.

The experimentally measured behavior of the matrices is more similar to the metamaterial simulation both in values, as their measured CTE curves approach the simulated one, and in shape of the curve, as no CTE jumps were observed in the matrices. The measured values for the unit cells are more similar to the unit cell simulations, however, there are differences between the triangle and X unit cells. This discrepancy will be discussed in the next section.

4. Discussions

The results in this work show that a good agreement between simulated and measured CTE of metamaterials or their unit cells can be achieved by choosing a representative segment of the metamaterial and by considering possible bulging effects of single unit cells, that would not have been predicted by the simulation of metamaterials with several unit cells. Therefore, a correct selection of the metamaterial segment and its simulation's boundary conditions are of extreme relevance to predict the NTE behavior of these structures.

4.1. Influence of the geometric features on the CTE

In this subsection, the results obtained from the parameter study simulations of triangle unit cells (section 3.2) are discussed. The results of the printed triangle unit cells are given only as examples that corroborate with the observations made in this part of the study.

The parameter study has demonstrated that the varied geometric features (listed in Table 1) affect the CTE of metamaterials and unit cells. The thickness and the presence of an offset play a role at angles smaller than 30°, whereas at larger angles, they do not significantly alter the CTE, with the CTE being almost exclusively influenced by the angle itself.

Very low CTE values are only achieved if the triangle mechanism described in Fig. 1 is not impaired, i.e. if the top vertex of the triangle can get closer to its base by the inward rotation of the triangle's sides or side vertices. Therefore, vertices between the base and the sides of the triangle play the important role of a compliant hinge. Simple calculations were done with the basic triangle geometry composed of 1D lines, connected with vertices that can rotate freely, as depicted in Fig. 1. The linear thermal expansion of the composing materials at 50 °C were considered to calculate the CTE of this theoretical triangle at this temperature. The results in Fig. 11 show that the lower the angle, the lower should be the CTE of the triangle. Similar to the simulated 3D triangles (Fig. 6), the curve of angle vs. CTE also displays an asymptotic behavior

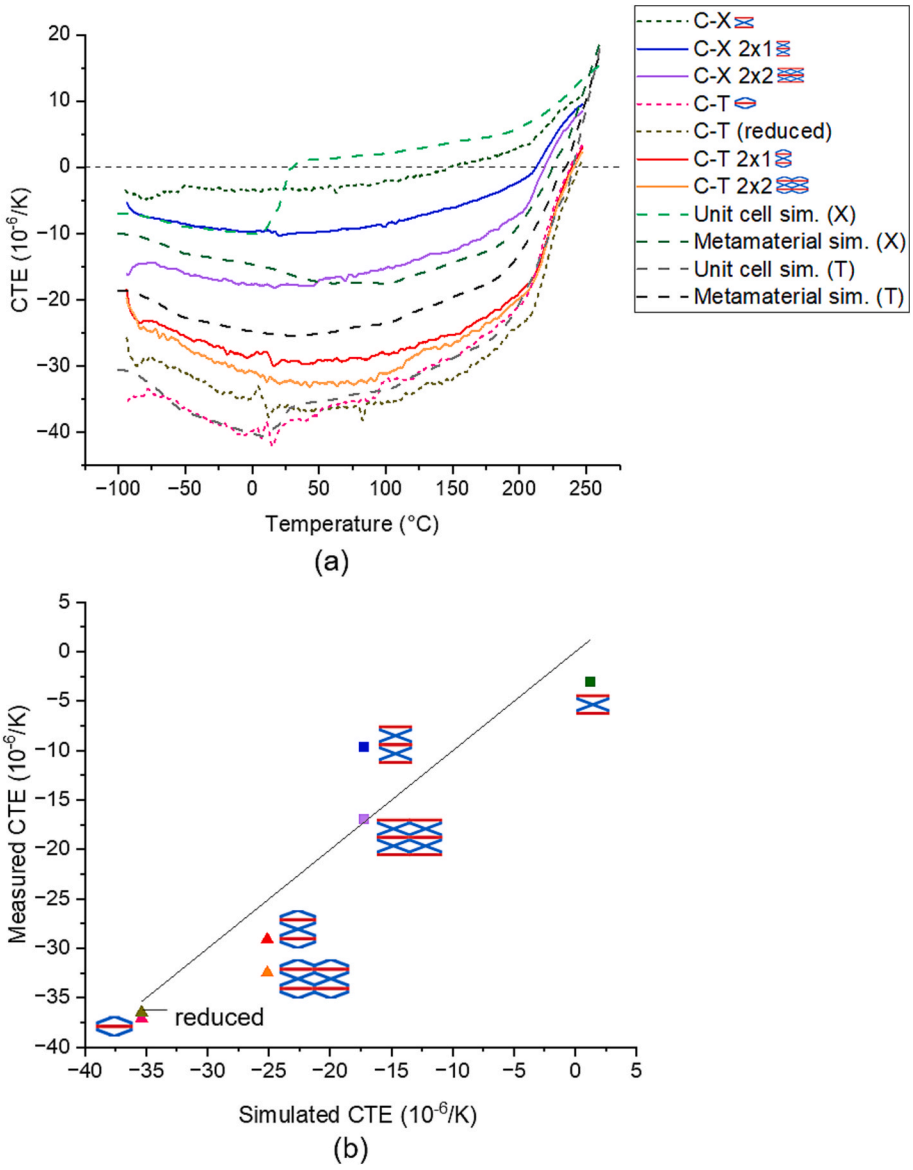


Fig. 10. (a) Measured CTE of the metamaterial matrices of the structure C plotted together with the measured CTE of their respective unit cells, in short-dashed lines, and their metamaterial and unit cell simulations (for triangle and X unit cells), in dashed lines. (b) Simulated vs. measured CTE at 50 °C: the straight line indicates a perfect match between simulation and measurement; the points represent the measured value for each of the printed structures, color-coded with the same colors as in (a).

at high angles. However, at very low angles, the CTEs of the 3D triangles tend to increase (Fig. 6), unlike the calculations for the simple 1D triangles. This happens because the hinge mechanism of the triangles simulated and printed in this work is affected by the amount of material around it. As the hinge becomes more massive, the hinge stiffness increases.

By reducing the strut thickness or increasing the offset, the hinge becomes less stiff and allows a greater rotation of the triangle sides. To demonstrate it, FEM simulations were done with 4 different unit cell geometries with same angle (20°), but different thickness and different offset. Instead of heating the unit cells, loads of 10 MPa were applied on their top and bottom surfaces. In Fig. 12a, their relative length variation is plotted against the applied load. In Fig. 12b, the hinge stiffness of these unit cells is plotted against their CTE at the temperature of 50 °C. For this plot, the hinge stiffness was obtained from the slope of their respective curves in Fig. 12a. The red point in Fig. 12b, with zero stiffness, represents the data from the simple calculations done with the triangle geometry composed of 1D lines (Fig. 11), which would have a fully compliant hinge. Again, these plots show that the lower the hinge stiffness, i.e. the higher its compliance, the lower is the CTE achieved.

Examples of triangle unit cells with the same angle, but different offsets are unit cells C-T and E-T; and same angle, but different thicknesses are A-T and B-T (all of them illustrated in Fig. 2b). In the case of the unit cell E-T, because of the lack of an offset, the triangle's sides have a large contact area with the triangle's base and the hinge mechanism is significantly hindered in comparison with the unit cell C-T. To a lesser extent, the same happens when the strut thickness is increased, as it can be seen comparing the unit cells A-T and B-T. Despite the movement restriction caused by the hinge constraint, the triangle mechanism is not completely impaired in the unit cells E-T and B-T and still allows these structures to present a negative CTE, but not as low as their counterparts with an offset or with smaller thickness.

This behavior was evidenced again in the simulations done for the full temperature range and in the printed unit cells (see Fig. 9). The unit cell A with thinner struts presented a considerably lower CTE than the unit cell B with thicker struts, showing good accordance to what was

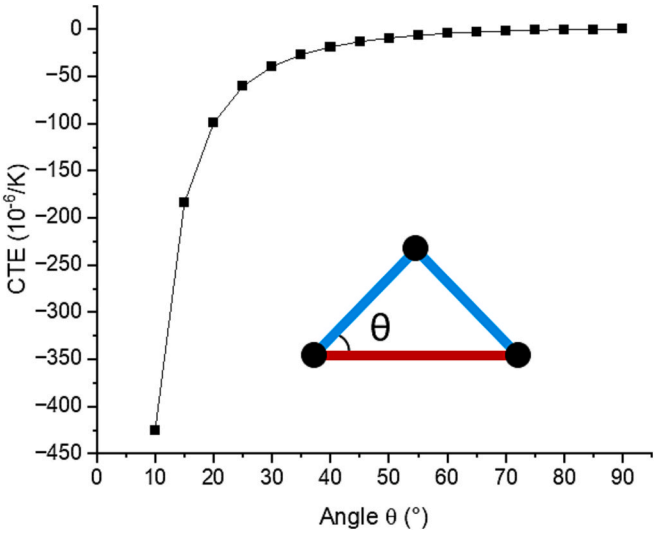


Fig. 11. Theoretical CTE of a bi-material triangle composed of 1D lines at 50 °C.

predicted by the simulations. The same can be stated for the unit cells C and E, which have same angle (20°) and thickness (2 mm), but different offsets (2 mm and 0 mm, respectively). The presence of the offset in the unit cell C allowed it to achieve lower CTE values than E.

However, for angles $\theta \geq 40°$, the offset and thickness play less of a role in the structure's CTE, because the hinge mechanism at these angles is not severely affected by the addition of bulk material to it. This is supported by the convergence of the four curves in Fig. 6a and b into similar CTE values, despite the different thickness and offset values considered in this work.

4.2. X unit cells vs. Triangle unit cells

In this subsection, the two types of unit cells are compared, both in terms of predicted (Fig. 7) and measured CTEs (Fig. 8and Fig. 9). The objective is to explain why the triangle unit cells presented a better agreement with their simulations than the X-unit cells.

Although the CTE curve predicted by the metamaterial simulations of the X and triangle unit cells are similar in shape and do not differ much in values, the simulated and measured CTE curves of the unit cells alone are quite different (see Fig. 7). The switch in the bulging mode at 20 °C has led to CTE jumps at this temperature in their simulations. This effect happens to both unit cell geometries, but for the X unit cells it is more intense. However, as it was presented in Fig. 8a, the CTE jumps in the measured X unit cells neither necessarily appear at 20 °C nor do they happen only once or in the intensity predicted by the simulations. Additionally, as presented in Fig. 8b and c, respectively, the jumps are reproducible in the same measurement cycle, but not in different measurements of the same sample. There are two factors that could be responsible for this: (1) the measurements are susceptible to the way the samples are placed in the dilatometer, i.e. if the samples are not placed at their exact center point onto the pushrod, it can slightly tilt during the thermal cycle causing jumps because of the tilting and not only because of the bulging; and (2) the top and bottom surfaces of the simulated unit cells are plane and parallel to each other, whereas the PBF-LB process leads to irregular surfaces and slightly warped parts due to thermal stresses, which are conditions that could intensify the tilting of the sample.

On the other hand, the triangle unit cells presented their CTE jumps at the predicted 20 °C, even after re-inserting the specimens into the dilatometer, and no additional jumps were observed (Fig. 9). Although some triangle unit cells did not present the predicted CTE jump, like structures B- and E-T, in general this geometry leads to more reliable

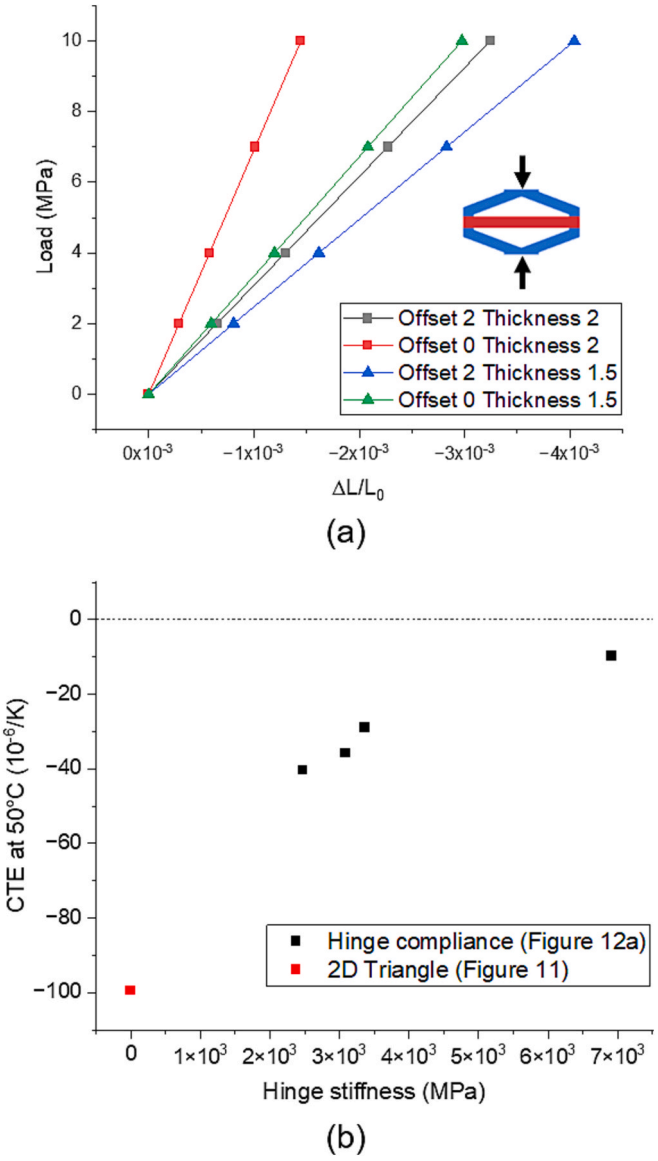


Fig. 12. (a) Hinge compliance comparison between unit cells with the same angle (20°): by reducing the strut thickness or increasing the offset, the hinge becomes less stiff and allows a greater rotation of the triangle sides. (b) The slope of the curves in (a) are taken as the hinge stiffness in the X-axis and are plotted against the simulated CTE at 50 °C. The point with zero hinge stiffness represents the triangle with 20° angle from the 2D triangle calculations shown in Fig. 11. The higher the hinge stiffness, the less negative is the CTE.

results between simulations and measurements. For this reason, the following topics of the discussion will focus mainly on triangle unit cells.

4.3. Metamaterial vs. Unit cells

In this subsection, first, the results obtained from the unit cell and metamaterial simulations (Fig. 6 and Fig. 7) are discussed. Then, the metamaterial matrices 2x1 and 2x2 (Fig. 2c) are compared to their respective unit cells C-X or C-T (Fig. 10a). The objective is to explain why different results are expected from unit cells when they are surrounded by neighboring unit cells and how it is successfully evidenced by the CTE measurement of the metamaterial matrices. As a reminder, samples with more than 4 unit cells could not be printed due to: (1) restricted sample size of the dilatometer measuring system and (2) minimum feature size imposed by the resolution of the multi-material recoater – a metamaterial with many unit cells could not be

significantly reduced to fit into the dilatometer, because the thickness of the unit cells would be too small to guarantee the correct material deposition by the multi-material recoater.

The magnitude of the CTE jumps reflects the intensity of the bulging effect of the unit cells. When comparing the CTE curves of the structures B, C and D in Fig. 7c, which have increasing θ, but constant offset and thickness, it is observed that the larger the angle, the less pronounced is the bulging effect, thus leading to smaller CTE jumps. Smaller angles intensify the triangle mechanism, due to the increased hinge compliance evidenced in Fig. 6a. This increases the rotation of the triangle sides and, since no other unit cell is around the structure, its top and bottom surfaces bulge.

The bulging allows lower CTEs to be achieved, as it can be seen comparing the CTE values of the parameter study simulations with unit cell and metamaterial boundary conditions (Fig. 6a and b, respectively). As soon as the bulging is restricted by the neighboring unit cells in a metamaterial configuration, which increases the hinge stiffness, the shrinkage potential of these structures is reduced significantly and a similar effect to the impairment of the triangle mechanism is observed: below a certain angle, the CTE starts increasing again.

By observing structure C, which was later printed in single unit cells and in 2x1 and 2x2 matrices, its bulging gets restricted by neighboring unit cells, indicated by the absence of the CTE jump and the higher CTE values in the FEM simulations done with metamaterial boundary conditions (see Fig. 7c and d). This behavior was evidenced in the dilatometry measurements of the 2x1 and 2x2 unit cell matrices (Fig. 10a). The C-X and the C-T unit cells present quite different CTE values, but by adding surrounding unit cells to them, the CTE curves get closer to each other and approach the predicted curve by the metamaterial simulations. The bulging effect gets suppressed and no CTE jumps are observed.

4.4. Simulated vs. Measured CTE

In this subsection, it is discussed what is necessary for a simulation to achieve a good prediction of the thermal expansion behavior of printed structures and what needs to be considered in the printed structure for this to happen. The discussions in 4.2 and 4.3 are brought together and summarized.

The simulations were an important tool that helped correlate the CTE "jumps" with the bulging movement of the unit cell. The thermal expansion behavior of the X-unit cells was probably well predicted by the simulations, but their geometry is not suitable to be measured in the dilatometer, as it could be sensitive to the sample positioning. Therefore, it is also important to choose an appropriate segment of the metamaterial to allow a good predictability, which was achieved by selecting the triangle unit cells.

The good match between the simulated and measured CTE of the triangle unit cells, shown in Fig. 9, indicate that the boundary conditions applied in the unit cell simulations lead to a reliable prediction of their CTE. Grouping up to 4 unit cells together in the 2x1 and 2x2 matrices made the measured CTE to get closer to the CTE curve predicted by the metamaterial simulations. This indicates that unit cells alone do not present the same behavior as the metamaterial they compose, differently from what Wei et al. [30] observed.

Presumably, the unit cell matrices measured in our work did not exactly match the predicted behavior by the metamaterial simulations due to the sample size restriction imposed by the dilatometer, limiting the number of unit cells that fit into it. Conversely, the restrictions of the multi-material recoating system in the PBF-LB machine limit the minimum feature size of the lattices to be printed. We believe that a closer match to the metamaterial simulations would have been achieved if a larger matrix, i.e. more than 2x2 unit cells, could have been measured.

Nonetheless, the behavior of the metamaterials and their unit cells is now well understood and by applying the correct boundary conditions, any NTE metamaterial can be reliably simulated and have their behavior predicted. This allows an appropriate geometry to be selected prior to printing that could presumably be extrapolated in the future to more complex NTE structures, such as re-entrant [16,17] and topology optimized structures [13] proposed in the literature.

5. Conclusions

In this work, NTE metamaterials composed by Invar and Inconel 718 were successfully fabricated via metallic bi-material PBF-LB/M. By modifying geometric features, such as thickness, angle and offset between the triangle's base and sides, the metamaterials built with this material combination may present CTEs ranging from $-37x10^{-6}$ K^{-1} to $+5x10^{-6}$ K^{-1}, according to the FEM simulations applying metamaterial boundary conditions. Unit cells alone could reach even lower CTEs, down to $-90x10^{-6}$ K^{-1}, due to bulging of the top and bottom surfaces. The behavior of both metamaterials and unit cells were simulated and measured for a wide temperature range, including negative temperatures. A reliable prediction of the metamaterial's CTE along the whole temperature range is dependent on the boundary conditions considered during the simulation and the selection of a representative segment of the metamaterial.

The following key learnings are taken from this work:

- Factors such as surface quality, warping of the structures due to AM thermal stresses and placement of the sample into the dilatometer could have an influence on the sample's measured CTE of the samples. The selection of a geometry of the metamaterial that is less affected by these is important to achieve a better agreement with the simulations. In this work, the triangle unit cells have been shown to be more robust against these external effects than the X-unit cell.
- To achieve negative CTEs, the hinge of the triangle structures, i.e. their side vertices, should be kept as compliant as possible by using thinner struts or adding an offset between the base and the sides of the triangle.
- Single unit cells behave differently from lattice structures in this type of NTE metamaterials, since the presence of surrounding unit cells impede the bulging of the triangles' struts. This phenomenon is particularly relevant for triangles with low angles, where bulging is more prone to happen, due to an increased rotation of the triangles' sides.

In summary, highly negative CTEs are possible to be achieved in one direction by utilizing the material combination presented in this work, which is useful to compensate the positive thermal expansion behavior of other materials in components that require a high dimensional stability. The good match of the FEM simulated and measured CTE of the unit cells as well as the fact that the measured CTE approaches the simulated CTE of the metamaterials as more unit cells are added, show that FEM simulations are an important design tool to predict the CTE of the printed structures. Our results enable future work on tuning the triangle's geometry to achieve a desired negative CTE and to print more complex metallic metamaterials that could achieve an isotropic negative CTE.

CRediT authorship contribution statement

I.B. Prestes: Writing – original draft, Visualization, Validation, Software, Methodology, Investigation, Formal analysis, Data curation, Conceptualization. **E. Buchmann:** Writing – review & editing, Conceptualization. **P. Höfer:** Writing – review & editing, Funding acquisition. **E.A. Jägle:** Writing – review & editing, Supervision, Methodology, Funding acquisition, Conceptualization.

Funding

This research as part of project SeRANIS is funded by dtec.bw –

Digitalization and Technology Research Center of the Bundeswehr which we gratefully acknowledge. dtec.bw is funded by the European Union – NextGenerationEU.

Declaration of competing interest

The authors declare the following financial interests/personal relationships which may be considered as potential competing interests: Isabel Beatriz Prestes reports financial support was provided by dtec.bw (Digitalization and Technology Research Center of the Bundeswehr)-NextGenerationEU. If there are other authors, they declare that they have no known competing financial interests or personal relationships that could have appeared to influence the work reported in this paper.

Data availability

Data will be made available on request.

References

[1] R. Lakes, Cellular solids with tunable positive or negative thermal expansion of unbounded magnitude, Appl. Phys. Lett. 90 (2007) 221905, https://doi.org/10.1063/1.2743951.
[2] G. Jefferson, T.A. Parthasarathy, R.J. Kerans, Tailorable thermal expansion hybrid structures, Int. J. Solids Struct. 46 (2009) 2372–2387, https://doi.org/10.1016/j.ijsolstr.2009.01.023.
[3] H. Xu, A. Farag, D. Pasini, Multilevel hierarchy in bi-material lattices with high specific stiffness and unbounded thermal expansion, Acta Mater. 134 (2017) 155–166, https://doi.org/10.1016/j.actamat.2017.05.059.
[4] M.M. Toropova, C.A. Steeves, Adaptive bimaterial lattices to mitigate thermal expansion mismatch stresses in satellite structures, Acta Astronaut. 113 (2015) 132–141, https://doi.org/10.1016/j.actaastro.2015.03.022.
[5] K. Wei, Y. Peng, K. Wang, S. Duan, X. Yang, W. Wen, Three dimensional lightweight lattice structures with large positive, zero and negative thermal expansion, Compos. Struct. 188 (2018) 287–296, https://doi.org/10.1016/j.compstruct.2018.01.030.
[6] X. Guo, X. Ni, J. Li, H. Zhang, F. Zhang, H. Yu, J. Wu, Y. Bai, H. Lei, Y. Huang, J. A. Rogers, Y. Zhang, Designing Mechanical Metamaterials with Kirigami-inspired, Hierarchical Constructions for Giant positive and negative thermal expansion, Adv. Mater. 33 (2021) e2004919, https://doi.org/10.1002/adma.202004919.
[7] C.A. Steeves, S.L. dos Santos e Lucato, M. He, E. Antinucci, J.W. Hutchinson, A. G. Evans, Concepts for structurally robust materials that combine low thermal expansion with high stiffness, J. Mech. Phys. Solids 55 (2007) 1803–1822, https://doi.org/10.1016/j.jmps.2007.02.009.
[8] H. Xu, A. Farag, D. Pasini, Routes to program thermal expansion in three-dimensional lattice metamaterials built from tetrahedral building blocks, J. Mech. Phys. Solids 117 (2018) 54–87, https://doi.org/10.1016/j.jmps.2018.04.012.
[9] Q. Zhang, Y. Sun, A series of auxetic metamaterials with negative thermal expansion based on L-shaped microstructures, Thin-Walled Struct. 197 (2024) 111596, https://doi.org/10.1016/j.tws.2024.111596.
[10] T.-C. Lim, Negative thermal expansion structures constructed from positive thermal expansion trusses, J. Mater. Sci. 47 (2012) 368–373, https://doi.org/10.1007/s10853-011-5806-z.
[11] K. Wei, Y. Peng, W. Wen, Y. Pei, D. Fang, Tailorable thermal expansion of Lightweight and Robust Dual-Constituent Triangular Lattice Material, J. Appl. Mech. 84 (2017) 101006, https://doi.org/10.1115/1.4037589.
[12] L. Wu, B. Li, J. Zhou, Isotropic negative thermal expansion Metamaterials, ACS Appl. Mater. Interfaces 8 (2016) 17721–17727, https://doi.org/10.1021/acsami.6b05717.
[13] O. Sigmund, S. Torquato, Composites with extremal thermal expansion coefficients, Appl. Phys. Lett. 69 (1996) 3203–3205, https://doi.org/10.1063/1.117961.
[14] Q. Wang, J.A. Jackson, Q. Ge, J.B. Hopkins, C.M. Spadaccini, N.X. Fang, Lightweight Mechanical Metamaterials with Tunable negative thermal expansion, Phys. Rev. Lett. 117 (2016) 175901, https://doi.org/10.1103/PhysRevLett.117.175901.
[15] J. Lehman, R.S. Lakes, Stiff, strong, zero thermal expansion lattices via material hierarchy, Compos. Struct. 107 (2014) 654–663, https://doi.org/10.1016/j.compstruct.2013.08.028.
[16] X. Li, W. Gao, Y. Zhou, Y. Lu, Novel 2D metamaterials with negative Poisson's ratio and negative thermal expansion, Extreme Mech. Lett. 30 (2019) 100498.
[17] L. Ai, X.-L. Gao, Three-dimensional metamaterials with a negative Poisson's ratio and a non-positive coefficient of thermal expansion, Int. J. Mech. Sci. 135 (2018) 101–113, https://doi.org/10.1016/j.ijmecsci.2017.10.042.
[18] M.-M. Chen, M.-H. Fu, L.-H. Lan, S.V. Sheshenin, A novel 3D structure with tunable Poisson's ratio and tailorable coefficient of thermal expansion based on a tri-material triangle unit, Compos. Struct. 253 (2020) 112803, https://doi.org/10.1016/j.compstruct.2020.112803.
[19] R. Lakes, Cellular solid structures with unbounded thermal expansion, J. Mater. Sci. Lett. 15 (1996) 475–477.
[20] E. Buchmann, F. Hadwiger, C. Petroll, C. Zauner, A. Horoschenkoff, P. Höfer, A,, in: Unit Cell with Tailorable Negative Thermal Expansion Based on a Bolted Additively Manufactured Auxetic Mechanical Metamaterial Structure: Development and Investigation, Springer, Berlin Heidelberg, Berlin, Heidelberg, 2023, pp. 198–211.
[21] E. Buchmann, I. Prestes, B. Musil, P. Höfer, in: Design and Investigation of a Thermoelastic Actuator with Tailored Unidirectional Thermal Expansion and Stiffness Using Mechanical Metamaterials and Joule Heating Activation, Springer International Publishing, Cham, 2023, pp. 1–14.
[22] T.-C. Lim, Negative thermal expansion in transversely isotropic space frame trusses, Physica Status Solidi (b) 250 (2013) 2062–2069, https://doi.org/10.1002/pssb.201384234.
[23] J.N. Grima, P.S. Farrugia, R. Gatt, V. Zammit, A system with adjustable positive or negative thermal expansion, Proc. R. Soc. A. 463 (2007) 1585–1596, https://doi.org/10.1098/rspa.2007.1841.
[24] C.S. Ha, E. Hestekin, J. Li, M.E. Plesha, R.S. Lakes, Controllable thermal expansion of large magnitude in chiral negative Poisson's ratio lattices, Physica Status Solidi (b) 252 (2015) 1431–1434, https://doi.org/10.1002/pssb.201552158.
[25] E. Gdoutos, A.A. Shapiro, C. Daraio, Thin and Thermally Stable Periodic Metastructures, Exp. Mech. 53 (2013) 1735–1742, https://doi.org/10.1007/s11340-013-9748-z.
[26] K. Wei, H. Chen, Y. Pei, D. Fang, Planar lattices with tailorable coefficient of thermal expansion and high stiffness based on dual-material triangle unit, J. Mech. Phys. Solids 86 (2016) 173–191, https://doi.org/10.1016/j.jmps.2015.10.004.
[27] H. Xu, D. Pasini, Structurally Efficient Three-dimensional Metamaterials with Controllable thermal expansion, Sci. Rep. 6 (2016) 34924, https://doi.org/10.1038/srep34924.
[28] J.S. Raminhos, J.P. Borges, A. Velhinho, Development of polymeric anepectic meshes: auxetic metamaterials with negative thermal expansion, Smart Mater. Struct. 28 (2019) 45010, https://doi.org/10.1088/1361-665X/ab034b.
[29] J. Qu, M. Kadic, A. Naber, M. Wegener, Micro-Structured Two-Component 3D Metamaterials with negative Thermal-expansion Coefficient from positive Constituents, Sci. Rep. 7 (2017) 40643, https://doi.org/10.1038/srep40643.
[30] K. Wei, X. Xiao, J. Chen, Y. Wu, M. Li, Z. Wang, Additively manufactured bi-material metamaterial to program a wide range of thermal expansion, Mater. Des. 198 (2021) 109343, https://doi.org/10.1016/j.matdes.2020.109343.
[31] Y. Ding, M. Akbari, X.-L. Gao, L. Ai, R. Kovacevic, Use of a Robotized Laser Powder-Feed Metal Additive Manufacturing System for Fabricating Metallic Metamaterials, in: T.S. Srivatsan, T.S. Sudarshan, K. Manigandan (Eds.), Manufacturing Techniques for Materials, CRC Press, 2018, pp. 51–65.
[32] M. Bambach, M.R. Tucker, Laser powder bed fusion of planar bi-metallic thermally auxetic lattice structures, CIRP Ann. 73 (2024) 141–144, https://doi.org/10.1016/j.cirp.2024.04.023.
[33] E.M. Parsons, Lightweight cellular metal composites with zero and tunable thermal expansion enabled by ultrasonic additive manufacturing: Modeling, manufacturing, and testing, Compos. Struct. 223 (2019) 110656, https://doi.org/10.1016/j.compstruct.2019.02.031.
[34] D. Han, H. Lee, Recent advances in multi-material additive manufacturing: methods and applications, Curr. Opin. Chem. Eng. 28 (2020) 158–166, https://doi.org/10.1016/j.coche.2020.03.004.
[35] I.B. Prestes, E.A. Jägle, Influence of the laser strategy on bi-metallic interfaces printed via multi-material laser-based powder bed fusion, Addit. Manuf. Lett. 13 (2025) 100274, https://doi.org/10.1016/j.addlet.2025.100274.
[36] N.J. Harrison, I. Todd, K. Mumtaz, Thermal expansion coefficients in Invar processed by selective laser melting, J. Mater. Sci. 52 (2017) 10517–10525, https://doi.org/10.1007/s10853-017-1169-4.

Publication {3}

Towards space application of a mechanical metamaterial fabricated via bi-metallic additive manufacturing to guarantee dimensional accuracy

Prestes, I.B., Rottler, J., Jägle E.A.

Manuscript – Submitted to Smart Materials and Structures

Towards space application of a mechanical metamaterial fabricated via bi-metallic additive manufacturing to guarantee dimensional accuracy

Authors

I.B. Prestes*[1], J. Rottler[2], E.A. Jägle[1]

Affiliation

[1]Institute of Materials Science, Universität der Bundeswehr München, Neubiberg, Germany

[2]Institute of Mechanics, Universität der Bundeswehr München, Neubiberg, Germany

***Corresponding author**. E-mail address: isabel.prestes@unibw.de

Abstract

Dimensional accuracy and structural stability are critical for space applications such as optical benches. This study investigates metamaterials with a tunable coefficient of thermal expansion (CTE) to achieve athermalization in satellite structures without compromising their mechanical integrity. The metamaterial consists of triangular unit cells made of Invar and Inconel 718, fabricated via bi-material laser-based powder bed fusion (PBF-LB). Dimensional accuracy should be achieved by both passive and active stabilization strategies. Experimental measurements using dilatometry and digital image correlation show good agreement with finite element method (FEM) simulations of the metamaterial's CTE. CTE values can be tuned from -20×10^{-6}/K to $+31 \times 10^{-6}$/K by changing the unit cell geometry, switching material assignments, and combining different unit cells. Compared with metamaterials with only positive- or negative-CTE unit cells, a more stable CTE can be obtained by combining negative- and positive-CTE unit cells. Adding a trapezoidal geometry for active heating does not affect the CTE. Mechanical tensile tests suggest a strong bi-material bond, with failure occurring in the weaker material – Invar. Although FEM simulations predict interfacial stresses exceeding Invar's ultimate tensile strength under temperature changes, no damage or plastic deformation was observed after 500 cycles across a 270°C span. These findings confirm the metamaterial's reliability and provide a basis for developing more advanced tunable CTE structures for space applications.

Keywords: Tunable CTE, Metamaterials, Simulation, Multi-material Additive Manufacturing, Schaeffler Aerosint recoater

Highlights

- Metallic metamaterials with tunable CTE fabricated via multi-material PBF-LB.
- Metamaterial with negative CTE printed for a satellite experiment.
- FEM simulations predict the thermal expansion behavior of printed metamaterials.
- Metamaterials present structural integrity suitable for satellite application.
- Metamaterial CTE values can be tuned from -20 to $+31 \times 10^{-6}$/K.

1. Introduction

Since the launch of the first dedicated earth observation program in the 1970s, there has been a continuous drive to improve the resolution of images captured by satellite instruments, which is closely linked to their structural stability and dimensional accuracy [1]. Achieving these requirements is particularly challenging due to the thermomechanical stresses that satellite structures endure, including thermal cycling and launch vibrations. Moreover, thermal distortions caused by the in-orbit temperature variations would degrade image resolution and, in non-imagery applications, overall signal detection. For this reason, materials used in space optics must have sufficient mechanical strength to withstand the launch procedure, while also exhibiting high thermal stability, usually characterized by a near-zero coefficient of thermal expansion (CTE). However, these two properties are often inherently conflicting, making the material selection for these applications a critical aspect for space optics design [1–5].

To address this challenge, the design of metamaterials with tunable CTE has been the research topic of many studies (see [6] for an overview). These engineered materials are composed of at least two different materials, with a large CTE difference among them, arranged in a specific lattice structure. Depending on the material selection, their CTEs can be tuned from negative to highly positive CTE, including near-zero CTE [6–9]. Although the latter would be the most intuitive fit for space optics applications, other CTE ranges can be potentially applied to satellite components. For instance, Holz et al. [10] designed an optical bench with negative CTE composite tubes made of aluminum, steel, and titanium collars, that cancel the positive CTE of the other components, resulting in an overall near-zero CTE structure. Some authors also cite the possibility of using highly positive CTE metamaterials to work as actuators in space applications [11–13].

Since the late 1990s, starting with Lakes' cellular solid structure with bi-material strips [14], numerous structural designs for tunable CTE metamaterials have been proposed, with different mechanisms to achieve the desired property, including other bi-material strips [11,15,16], triangular or tetrahedral [8,9,17–23], re-entrant [7,24–26], chiral or anti-chiral [16,27,28], and topology optimized structures [12,29]. However, the fabrication of these was limited for many years due to the lack of a suitable manufacturing technology for them. In the first attempts, bi-material structures were manufactured by conventional joining techniques, such as pin-joining [22], laser spot welding [8], gluing [27], bolting [30], interference fitting [13] or snap fitting [31]. While these methods enabled the CTE of the metamaterials to be experimentally assessed, they introduce geometric constraints and increase the complexity of the satellite structure design and modeling [1].

The fabrication of tunable CTE metamaterials without additional joining techniques became realistic with the advent of multi-material additive manufacturing (MMAM) [32,33]. The initial works in this topic were done in polymer MMAM and presented a good correlation with simulated CTE, but these would not present the required stiffness for satellite applications [7,15,25,26,34]. More recently, works in metal MMAM were done [35–39], showing the potential of using this technology to build tunable CTE metamaterials for satellite components, as they would present a higher stiffness and thermal conductivity than polymers. Among the existing literature, our previous work [39] is the only one that printed (sections of) bi-metallic metamaterials that (1) can be tuned across a wide range of CTEs, including negative values; (2) presented a defect-free interface [40]; and (3) assessed their CTE in cryogenic

temperatures, which simulate the space environment. However, due to the limited number of unit cells printed together in that study, the entire metamaterial's CTE had not been experimentally confirmed.

Metamaterials and AM are increasingly being adopted for space applications, especially in small satellite missions, which often serve as test platforms to increase the technology readiness level of innovative components. For this reason, a satellite experiment applying a metamaterial, derived from the structures studied in [39], [41] and [42], was proposed for the SeRANIS mission led by the University of the Bundeswehr Munich [42,43].

The aim of this paper is to further investigate the metamaterials introduced in [39,41,42], but from a space application perspective, which has not been shown for bi-metallic MMAM structures up to now. Besides the assessment of the metamaterials' CTE, their structural integrity is evaluated, and the role of additional geometric features to enable active thermal stabilization is explored. Furthermore, highly positive CTE metamaterials are designed, manufactured, and measured, broadening the scope of potential applications in satellite components.

2. Materials and methods

2.1. Description of the metamaterial for the satellite experiment

The experiment, in which the metamaterial studied in this paper will be mounted, is part of a satellite mission conducted by the University of the Bundeswehr Munich, which aims to develop and test new space application technologies [43]. In this particular experiment, a structure's dimensional stability is achieved by integrating a mechanical metamaterial with a negative thermal expansion behavior into it. This can be achieved by passive and active stabilization [41]: the first consists of maintaining the structures' dimensions due to the thermal properties of the metamaterial itself; the latter consists of actively heating certain parts of the metamaterial to stimulate its negative thermal expansion behavior. In both cases, the negative CTE of the metamaterial should compensate for the positive CTE of the components around it to keep the whole structure's dimensional stability. A more detailed description of the experiment as a whole can be found in [42]. The experiment is planned to be mounted on a part of the satellite without any external or additional temperature stabilization, thus exposing it to the harshest in-orbit temperature conditions. Therefore, the temperature range expected for the satellite experiment is from approximately -120°C to +150°C, consistent with values found in the literature (e.g., from -150°C to +150°C in [31]).

The metamaterial designed for this experiment consists of double-triangular-shaped unit cells made of two different materials. The triangle mechanism is presented in the schematic in Figure 1a: the base of the triangle is made of a material with a higher CTE than the material for the triangle's sides. When the temperature is increased, the base of the triangle will expand more than its sides, leading to a shrinkage in the triangle's height, thus leading to a negative CTE in the Y-axis. The unit cell of the metamaterial, which follows this principle, is shown in the schematic in Figure 1b. In this work, the material with higher CTE is Inconel 718, and the material with lower CTE is Invar. The thickness of the struts is 2 mm, the base of the triangle is 25 mm, the angle θ of the triangle is 20°, and an offset of 2 mm between the triangle's base and its sides was added to reduce the hinge stiffness and allow the metamaterial to bend more freely, as it was concluded in our previous works [39,41]. The metamaterial in this work,

presented in Figure 1c, combines these unit cells into a 4x2 matrix. At both ends of the metamaterial, two blocks of Inconel 718 with mounting holes were printed together with the metamaterial to allow its fixture into the experiment's structure. Moreover, trapezoidal structures made of Inconel 718 were printed on top of the struts made of the same material (i.e., the triangle's base), onto which heating elements are intended to be glued for the aforementioned active stabilization of the experiment's structure [41]. The active heating component and its contribution to the athermalization are the subject of forthcoming publications. In this paper, only the base metamaterial structure will be considered.

The material combination of Inconel 718 and Invar was chosen due to: (1) the large difference between their CTE, which is essential to build negative thermal expansion (NTE) structures [7,8], and (2) their metallurgical compatibility, allowing these two materials to be printed together in multi-material PBF-LB without leading to defects, such as cracks and pores, at their interface [40].

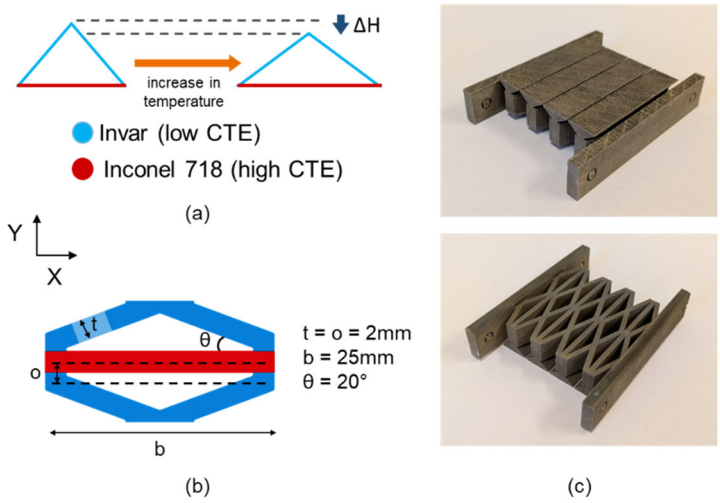


Figure 1 – (a) Triangle mechanism responsible for achieving negative CTEs: an increase in temperature causes a larger expansion of the triangle's base, which is composed of a material with higher CTE (Inconel 718), bending the triangle's sides, which are made of a material with lower CTE (Invar), leading to a shrinkage in the Y-direction. (b) Details of the triangular unit cell used for building the metamaterial. [42] (c) Pictures of the top and bottom of the printed bi-metallic metamaterial for the satellite experiment.

2.2. Bi-metallic Additive Manufacturing of the metamaterial

To fully understand the behavior of the metamaterial for the satellite experiment described in 2.1, additional structures were printed for this paper, which are presented as drawings in Figure 2c. These include single unit cells (with and without the trapezoid for later attachment of active heating elements) and 10x5, 4x1, and 2x1 matrices of unit cells, which had the same geometry as in the metamaterial for the satellite experiment (Figure 1b), but had their dimensions scaled down to fit their respective measurement devices (cf. section 2.4) for analyses.

All of the metamaterial structures in this work were manufactured via bi-metallic laser-based powder bed fusion (PBF-LB), performed in an Aconity3D MIDI+ machine equipped with a selective powder deposition recoater developed by Schaeffler Aerosint (Figure 2a). The recoater allows two different metallic powders to be deposited within the same layer. The deposition of each powder is done by patterning drums that eject particles located in the

activated voxel for the deposition of the layer. The size of a single voxel of 0.5x0.5 mm² defines the resolution of the material deposition. In Figure 2b, an example of a bi-metallic build job for this paper is shown, in which the 10x5 matrix was printed.

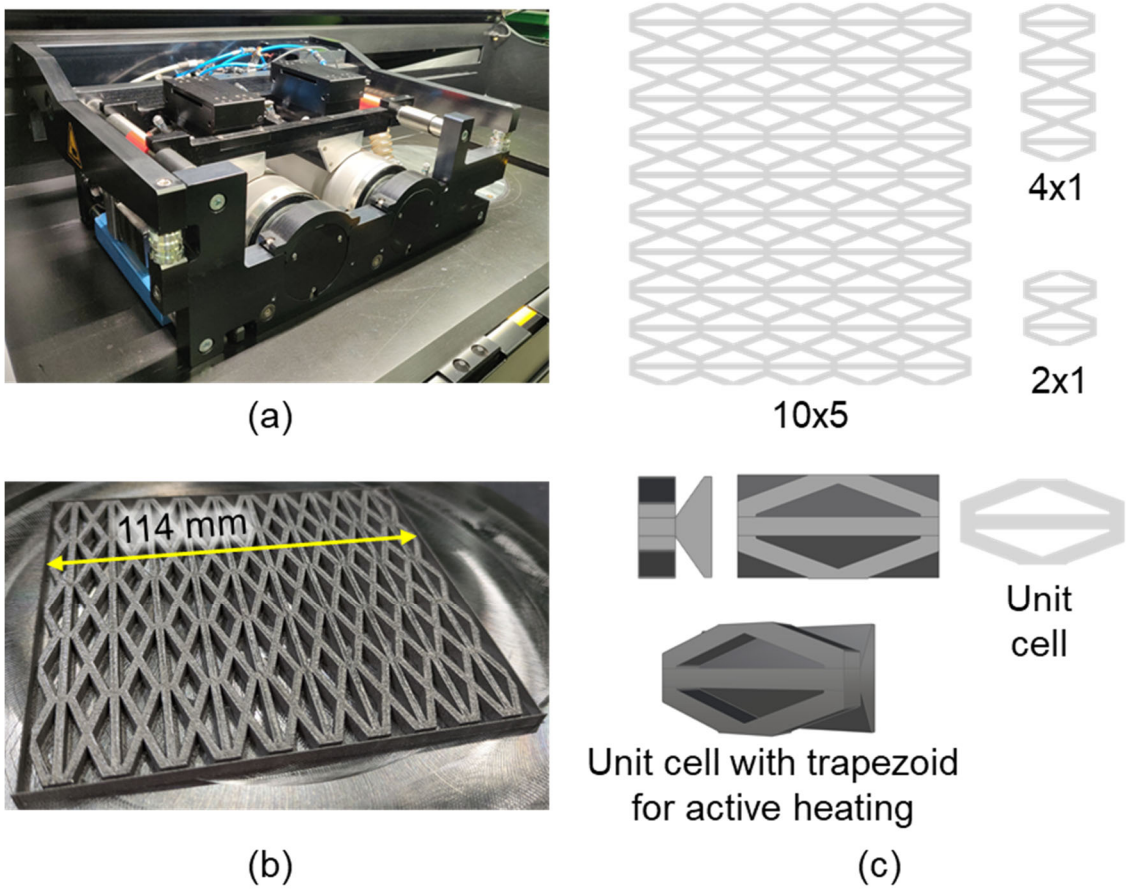


Figure 2 – Bi-metallic PBF-LB process: (a) Aerosint Schaeffler bi-material recoater; (b) example of a finished build job; and (c) drawing of the structures that were printed by this process for this work, besides the metamaterial presented in Figure 1c.

The metallic powders used in this work were provided by Praxair, were gas atomized, and had particle sizes ranging from 15 to 45 μm. The parts were printed under argon process atmosphere, and the PBF-LB parameters were the same for both materials, allowing the use of a single scan strategy (i.e., both materials are printed simultaneously, without interrupting the laser path at the interface) and thus avoiding porosity at their interface. Stripe hatching scans with a stripe width of 5 mm were applied to print the specimens to reduce thermal stresses and avoid warping. The PBF-LB parameters were: laser power of 180 W; scanning speed of 940 mm/s; angle increment per layer of 67°; hatch spacing and laser spot size of 80 μm; and a layer thickness of 40 μm. These parameters have led to dense parts and sound interfaces in our previous study [40].

After the printing process, the parts were cut from the base plate by electrical discharge machining (EDM). The experiment's metamaterial (Figure 1c) had, additionally, the holes on its side blocks drilled and the top surface of trapezoidal structures milled to remove the as-printed surface roughness for later gluing of the heating elements.

2.3. Simulations of the metamaterial

The metamaterial was simulated in the static structural module of Ansys Workbench version 2023 R2. The software database for Invar and Inconel 718 properties remained unchanged, except for their CTE, which were replaced by the measured CTE values of the as-printed materials [39].

Two different material assignments were considered in the simulations to achieve either a negative or a highly positive CTE. In the first condition, the base of the triangle (red region in Figure 1b) was made of Inconel 718, with higher CTE, while the sides (blue regions) were made of Invar, with lower CTE. In the second condition, the material assignments were reversed: Invar was used for the triangle's base and Inconel for its sides. By doing this, an "inverted triangle" mechanism leads to a highly positive CTE – one that exceeds the CTEs of the constituent materials, instead of a negative CTE.

Besides the unit cell geometry of the experiment described in 2.1, other triangle angles (represented by θ in Figure 1b) from 10° to 80° were simulated in order to understand how it would affect the CTE of the metamaterial. All unit cells were simulated by applying a periodic boundary condition in both X- and Y-directions (cf. axes in Figure 1). This aims to simulate these unit cells as if they were surrounded by many others, as in a metamaterial. The base and the sides of the triangle unit cell have a shared topology, meaning that they share elemental nodes at their interfaces and are considered bonded to each other. The simulations were conducted using a linear-elastic material model with second-order tetrahedral elements (SOLID187), which were locally refined at the unit cell hinges. Each model consisted of approximately 40,000 elements. Displacements and von Mises stresses were evaluated, and convergence was achieved in all cases.

The unit cells in the simulation were subjected to a linear temperature variation from -100°C to 260°C. At the end of the simulation, the length variation ΔL of the unit cells in temperature intervals of 10°C was extracted, and the CTE was calculated by Equation (1), where L20°C is the initial unit cell length at room temperature and L_i and T_i are, respectively, the length and the temperature of a point of measurement. The length variation was taken by subtracting the displacement between the top and the bottom surfaces of the unit cell.

$$CTE = \frac{1}{L_{20°C}} * \frac{(L_i - L_{20°C})}{(T_i - 20°C)} \quad (1)$$

2.4. Thermal expansion measurements

2.4.1. Dilatometry

The dilatometry measurements of this work were performed in a vertical dilatometer model L75 by Linseis, equipped with a low-temperature furnace. The installed measuring system in the

dilatometer allows samples with a diameter up to 30 mm to be measured. The samples were measured with a silica plate with a diameter of 6 mm on top of them[1].

The samples were measured under a helium atmosphere with a gas flow of 10 cm³/min in a thermal cycle that ranged from -100°C to 250°C, with cooling and heating rates of 2.5°C/min. The thermal cycle was composed of two cooling and heating curves in order to check the repeatability of the results and guarantee that the dilatometer was operating in a steady-state mode.

The CTE curves from the dilatometer measurements were calculated by Equation (1). To reduce the data noise close to room temperature, a Savitzky-Golay smoothing filter was applied to the resulting curve. The filter applied a moving average in a window of 40°C, which did not significantly affect the shape and values of the CTE curves outside the room temperature range, as can be observed in Figure A.1 in the Appendix.

2.4.2. Digital Image Correlation

The thermal expansion of the 10x5 matrix, which could not fit into the dilatometer, and the unit cell with negative CTE were measured using digital image correlation (DIC). A two-dimensional displacement analysis was performed with a Q-400-2D Limess camera in combination with the software Istra D 4.4.6 from Dantec Dynamics. The camera was fixed on an adjustable-height column attached to a platform and faced the sample from a distance of approximately 14.5 mm. The sample was placed onto a heating platform, to which a thermocouple was attached, and was heated from room temperature to different temperatures, from 60°C to 200°C, in 20°C increments. The samples were left unfixed on the heating platform to allow unrestricted thermal expansion and contraction. Before capturing the DIC images, the temperature homogeneity of the sample was verified by an InfraTec thermal camera, Image R type 8300hp. A schematic of the experimental setup is presented in Figure 3.

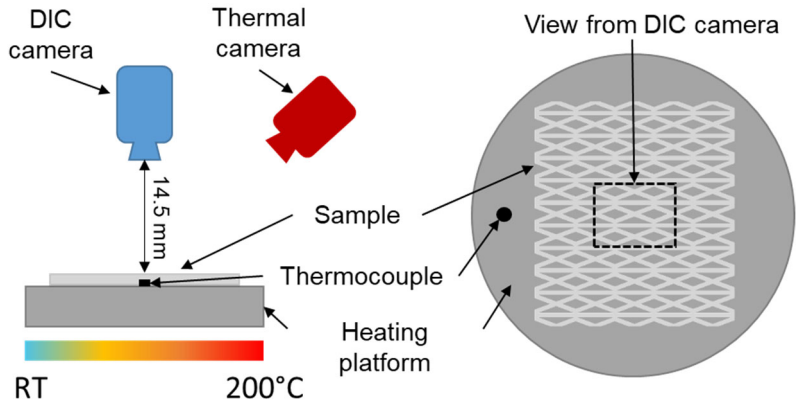


Figure 3 – Experimental setup of the DIC measurements.

[1] In comparison with the top plate of the dilatometer's measuring system, the ø6 mm silica plate reduces the area of contact with the top surface of the unit cells. In our previous study [39], a bulging effect was observed on the top and bottom surfaces of printed single unit cells, i.e. when no other unit cells were printed around them. This bulging has led to "jumps" in the CTE curves. To work around this issue in this paper, the silica plate is used to act like a "single-point contact" on the top surface and thus the bulging effect is not captured.

2.5. Structural integrity tests

2.5.1. Mechanical properties assessment

In order to check the mechanical integrity of the interface between the two metals, tensile tests were performed in single- and bi-material specimens. Blocks of 11x35x6 mm³ were printed, and tensile specimens parallel to the base plate were cut from them by EDM, as shown in the schematic in Figure 4a. Due to size restrictions of the AM process, non-standard specimens were designed, with their dimensions given in Figure 4b.

The specimens were fixed into a servo-hydraulic testing machine from Schenck with a static loading capacity of 10 kN controlled by the Doli Test&Motion software version 5.5.3.0. The elongation values were taken from the machine crosshead, since no extensometer was attached to the specimens. In Figure 4c, the experimental setup is shown.

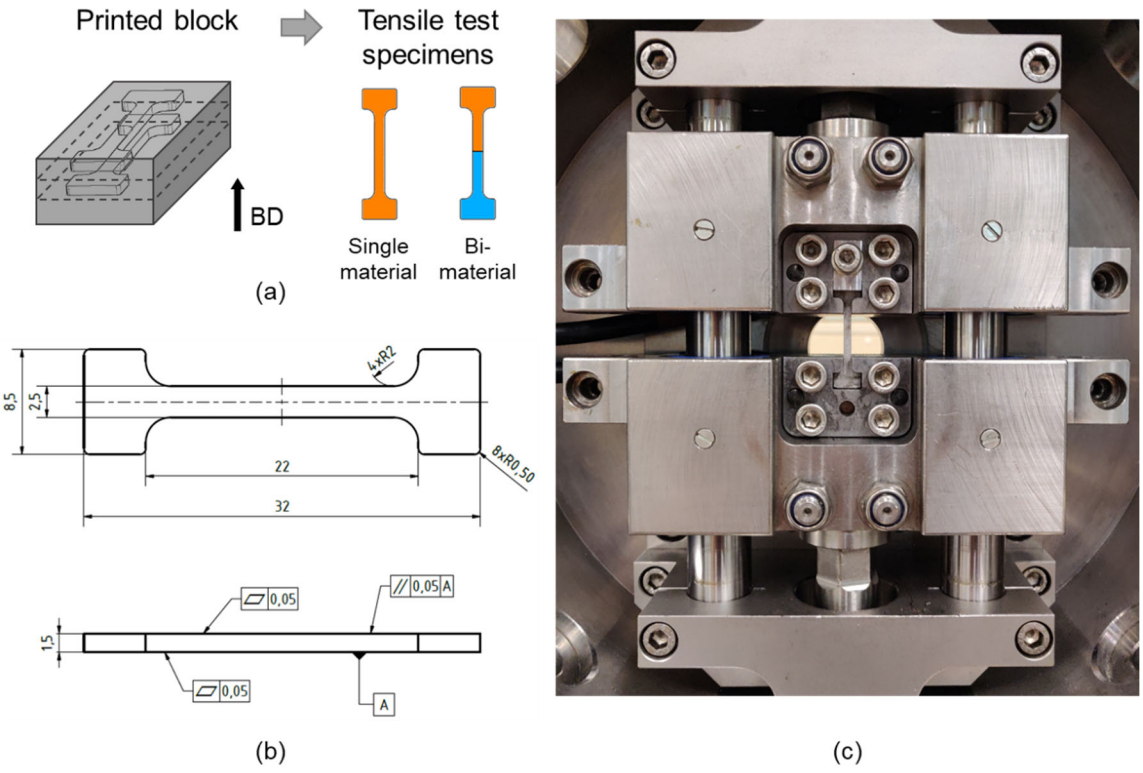


Figure 4 – Tensile test details: (a) schematic of the specimen manufacture by EDM from the printed blocks (the material interface of the bi-material specimens is perpendicular to the strain direction and located at the half of gauge length); (b) geometry of the non-standard specimens; (c) tensile test setup.

The Young's modulus of the printed materials was defined by measuring the ultrasonic velocity of longitudinal and shear waves in the bulk material at room temperature. For these measurements, two cubes (10x10x10 mm³) of each material were printed, had their top and bottom surfaces polished, and their density measured by the Archimedes method. The ultrasound echoes were acquired by Schenck ultrasonic transducers model tri CF-SW (shear waves) and model harisonic ABM-0504 (longitudinal waves), both working at a frequency of 5 MHz. The echoes were assessed in a ScanMaster's software version 3.5o. The method to calculate the Young's modulus from these measurements is described in [44].

2.5.2. Thermal cycling

Since the metamaterial will be subjected to many thermal cycles as the satellite orbits the Earth, it is useful to observe if these could lead to a failure of the metamaterial due to thermomechanical fatigue. Therefore, printed unit cells were thermal cycled in a Voetsch VT3 7006 S2 furnace that cyclically transports the samples from a hot chamber to a cold chamber. The hot chamber temperature was set to 200°C while the cold chamber was set to -70°C, meaning a temperature span of 270°C, which is the same maximum temperature span predicted during the satellite experiment (from -120°C to +150°C).

One cycle takes 8 minutes in each of the chambers, and this cycle was repeated 500 times. After these cycles, the unit cells were observed under an optical microscope to check if there were any cracks or visible plastic deformation at the hinge of the triangle, where the highest stresses are achieved, due to the movement of the triangle structure and the CTE mismatch between the materials.

3. Results

3.1. Simulated and measured thermal expansion

In Figure 5a, the simulated CTEs at 50°C of unit cells with different θ angles are plotted. In the legend, positive and negative CTE refer to the material assignment given in the simulation: to achieve a negative CTE, materials were assigned as shown in Figure 1b – blue material as Invar and red material as Inconel 718 –, whereas to achieve a positive CTE, the material assignment was reversed. The measured CTE at 50°C of the as-printed Inconel 718 and Invar are, respectively, 13.18×10^{-6}/K and 0.05×10^{-6}/K, and these values are plotted as horizontal dashed lines for comparison.

The positive and negative CTE plots are mirrored, and both achieve their maximum value (i.e., the most positive and the most negative CTE) at a θ angle of 20°. At 15° and 10°, the hinge movement of the triangular unit cell gets impaired due to an increasing hinge stiffness, as it was observed in a previous study of ours [39]. As the angle increases, the triangle mechanism becomes less effective and is completely negligible at 80°, in which the CTE is comparable to one of the composing materials.

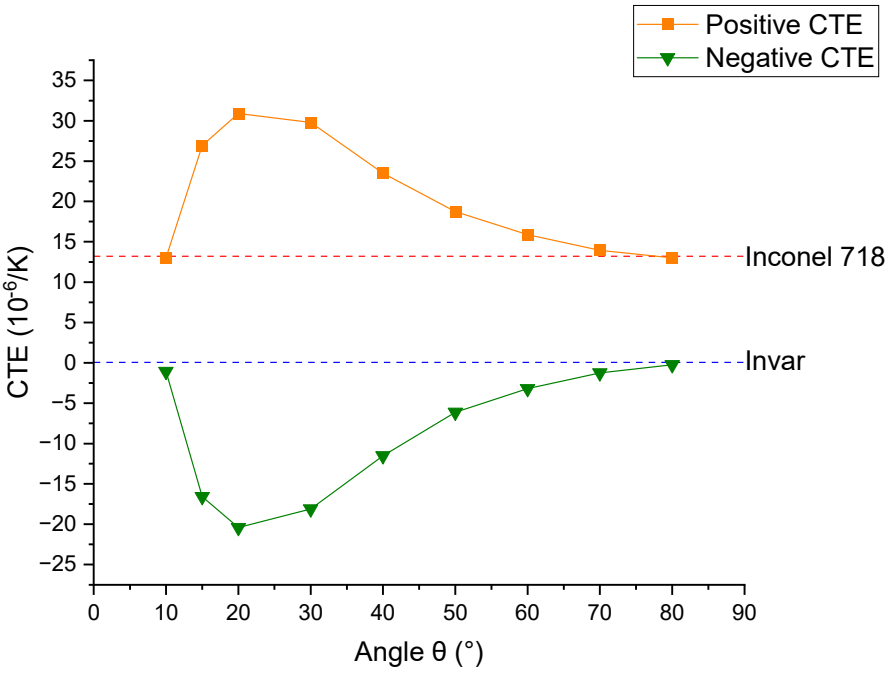
The CTE curves from -100°C to +250°C of the unit cell with a 20° angle, which is the one used to build the metamaterial of this work, are shown in Figure 1b. Although only a negative-CTE metamaterial was printed for the satellite experiment, positive CTE unit cells were also simulated and printed, as they could be useful for other satellite applications. Unit cells with and without the trapezoidal structure for the active heating were considered, as this extra geometry might affect the resulting CTE of the metamaterial.

In Figure 5b, not only the simulated CTE (in dashed lines) but also the measured CTE of the unit cells are plotted. According to the simulations, the addition of the trapezoid for active heating does not significantly influence the CTE, slightly increasing it for the positive-CTE unit cell and reducing it for the negative-CTE unit cell. In contrast, when comparing the measured CTEs, the CTE of the negative-CTE unit cell slightly increased with the addition of the trapezoid, while the positive-CTE unit cells (with and without the trapezoid) presented a very similar behavior.

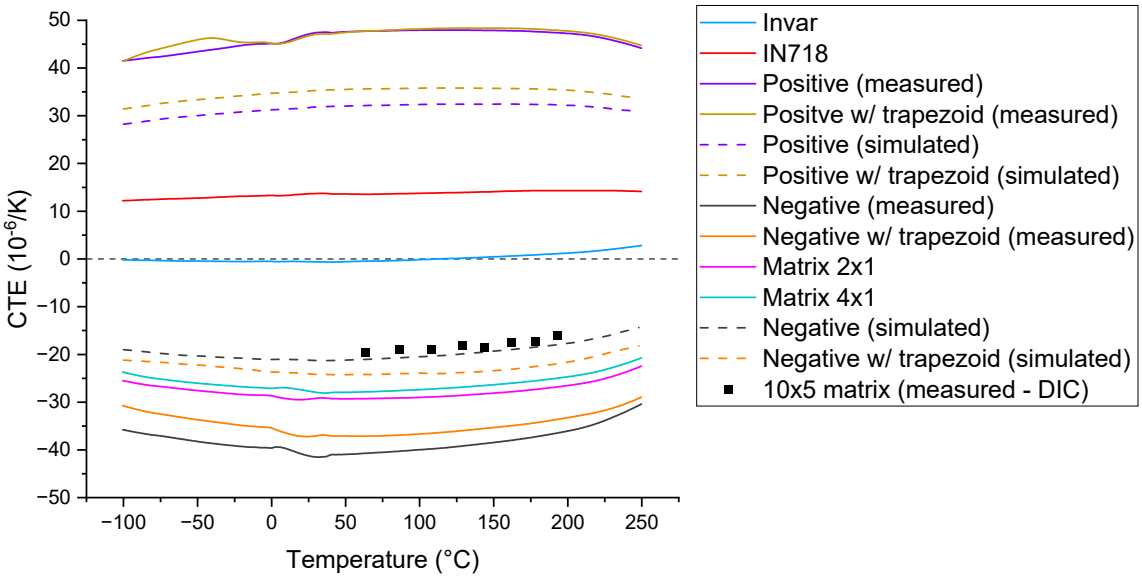
Regardless of the addition of the trapezoid geometry, the negative-CTE unit cells showed a lower CTE than in the FEM simulations, whereas the positive-CTE unit cells showed a higher CTE. This behavior was already observed in our previous study [39] and is associated with a bulging movement of the top and bottom surfaces of the unit cells when they are not surrounded by neighboring ones. In the negative-CTE condition, for example, the top and bottom surfaces bulge inwards at temperatures higher than 20°C (see Figure C.1 and Figure C.2 in the Appendix). This movement allows lower CTEs to be measured, as it intensifies the shrinkage of the unit cell. An opposite effect is observed in the positive-CTE condition, with the top and bottom surfaces bulging outwards (see Figure C.1 and Figure C.2 in Appendix). Once unit cells are added on top and bottom of the single unit cells, the bulging cannot happen and the measured CTE gets closer to the simulated CTE, as evidenced by the CTE curves of the 2x1 and 4x1 matrices (cf. geometry in Figure 2c) in Figure 5b.

Above approximately 200°C, the CTE increases for the negative-CTE unit cell (inversely, it decreases for the positive-CTE unit cell). This behavior is explained by the intrinsic increase of Invar's CTE at this temperature, which reduces the CTE difference between the composing materials, a key factor to achieve a negative CTE [7,8]. Below 200°C, a shallow parabola-shaped CTE curve similar to Invar's CTE is observed. The positive-CTE unit cells exhibit a mirrored behavior along the measured and simulated temperature range. Therefore, both positive- and negative-CTE structures present a CTE that is not constant along the measured temperature range. In an attempt to achieve a stable and constant CTE, positive- and negative-CTE unit cells were combined on top of each other. Unit cell angles were chosen based on the plots of Figure 1a to achieve a CTE of $+20 \times 10^{-6}$/K for positive-CTE and -20×10^{-6}/K for negative-CTE. These unit cells were designed together, simulated, and printed. The measured CTE of the combined unit cells is presented in Figure 6 together with its simulated curve and the simulated CTE curves of each unit cell separately, referred as CTE -20 and CTE +20.

Although the CTE at 50°C for these two unit cells of the same in magnitude, but they have opposite signs, the length of the unit cells and, thus, their length variation at this temperature is different in magnitude (see Equation (1)). For this reason, a CTE of $+4.8 \times 10^{-6}$/K would be expected at 50°C for the combination of the two unit cells. In Figure 6, the combined unit cells exhibit an increase in the CTE above 200°C, but the slope is less steep compared to the negative-CTE unit cell. Moreover, the parabola-shaped curve of the combined system is shallower than that of the individual unit cells, resulting in a more stable CTE over a wide temperature range.



(a)



(b)

Figure 5 – (a) Simulated CTE at 50°C of unit cells with different θ angles for material assignments that lead to either positive-CTE or negative-CTE. (b) Simulated and measured CTE curves from -100°C to 250°C for the metamaterial and for unit cells with θ angle of 20° with and without the trapezoidal structure for active heating.

To quantify these trends, a quadratic polynomial function was fitted to the curves across the full measured and simulated range. The absolute values of the coefficient a in the quadratic functions ($a*x^2 + b*x + c$) are presented in Table 1. A smaller coefficient a indicates a shallower curvature and thus a more stable CTE curve. The combined unit cells show a better performance than both negative- and positive-CTE unit cells in terms of stability. The combined unit cells also present a more stable CTE than Invar, approaching the flattened curve profile

observed for Inconel 718. The graph of Figure 6, together with the quadratic function fits, is available in Figure B.1 in the Appendix.

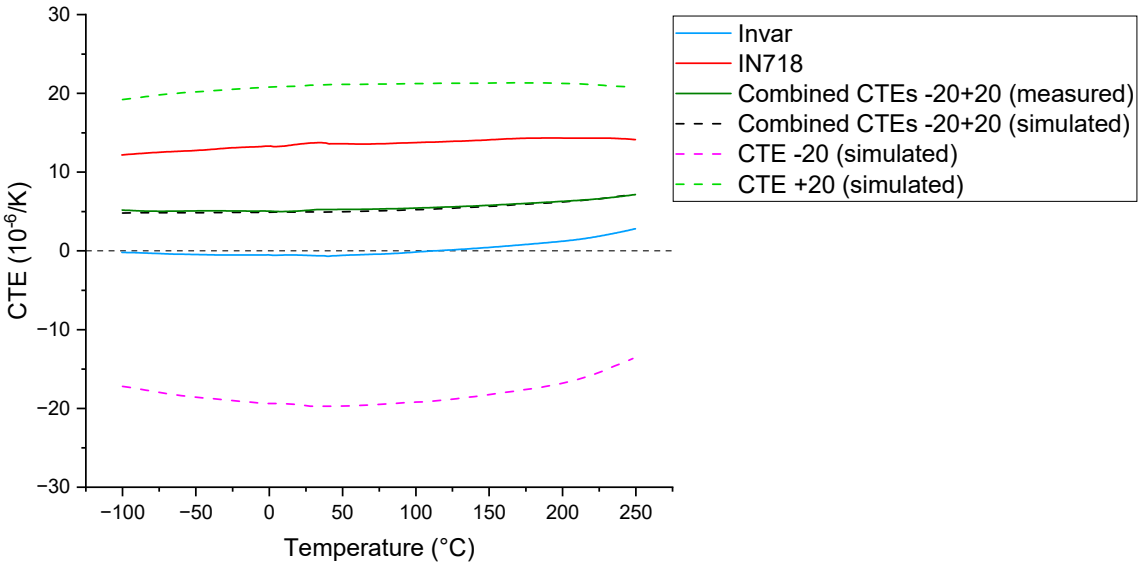


Figure 6 – Simulated and measured CTE of the combined unit cells. The simulated CTE of the negative- and positive-CTE unit cells alone are shown in dashed lines, and the measured CTE of the as-built Inconel 718 and Invar are shown in dotted lines.

Table 1 – Absolute value of coefficient *a* in quadratic functions fitted to the curves in Figure 6. The quadratic function ($a*x^2+b*x+c$) was fitted in the whole temperature range. A smaller coefficient *a* in the quadratic function indicates a shallower CTE curve, i.e. a more stable curve along the measured range.

	Combined CTEs	**CTE -20**	**CTE +20**	**Invar**	**IN718**
Coefficient a [1/K³] (Quadratic function)	$2.47x10^{-5}$	$13.0x10^{-5}$	$3.73x10^{-5}$	$5.20x10^{-5}$	$1.46x10^{-5}$

3.2. DIC measurements

The bulging effect on top and bottom surfaces of single unit cells, explained in section 3.1, could be captured in the DIC measurements (Figure C.1 and Figure C.2 in the Appendix). Because there are no other neighboring unit cells, the single unit cells are allowed to bulge unconstrained [39]. The addition of neighboring unit cells inhibits this bulging effect and brings the measured CTE closer to the simulated CTE, as was observed in Figure 5b with the CTE curves of the 2x1 and 4x1 matrices. However, since these matrices replicate the unit cell in only one direction and over a limited number of repetitions, their CTEs were still noticeably different from the metamaterial's simulated CTE. To evaluate whether the FEM simulations could reliably predict the CTE of the NTE metamaterial, the CTE of the 10x5 matrix was measured by DIC. In Figure 7, an example of a displacement image taken by the DIC camera is shown. The displacements in the Y-axis are relative to the reference image at room

temperature. The displacement of point 1 in Figure 7 is subtracted by the displacement of point 2 and the resulting value replaced the nominator $(L_i - L_{20°C})$ in Equation (1). $L_{20°C}$ in Equation (1) was replaced by the length of two unit cells; and T_i, by the temperature measured by the thermocouple attached to the heating platform (see Figure 3).

The CTE measured at each temperature set on the heating plate is plotted as scatter points together with other simulated and measured CTE curves in Figure 6b. The expansion behavior of the 10x5 matrix was very well predicted by the FEM simulations (black dashed line in Figure 6b).

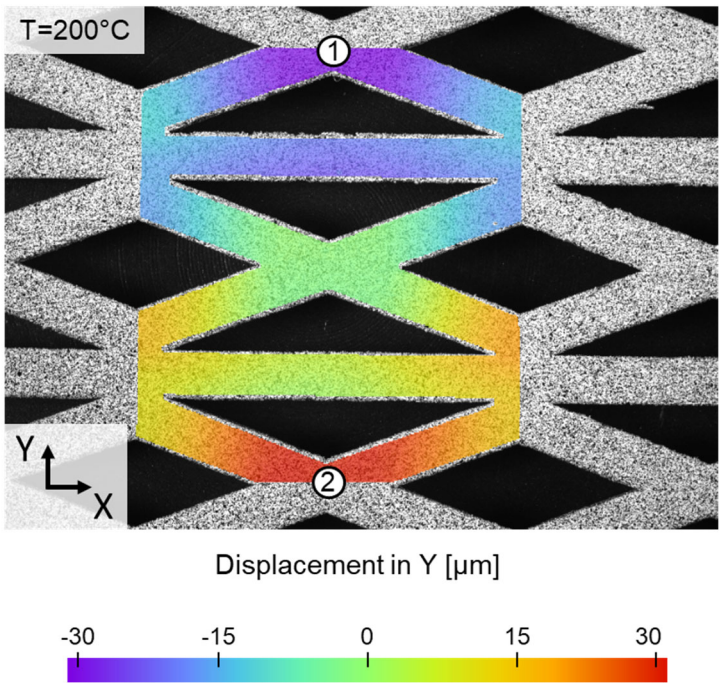


Figure 7 – DIC measurement of the 10x5 matrix: image of the displacement in the Y-axis at 200°C relative to the image at room temperature. Points 1 and 2 represent the positions, where displacement values were taken from to calculate the length variation at each temperature. This length variation replaced the nominator in Equation (1) to calculate the metamaterial's CTE.

3.3. Tensile tests

The stress-strain curves of the as-printed single material and bi-material samples are plotted in Figure 8, with the blue curves representing the Inconel 718 samples, green representing Invar, and purple representing the bi-material (BM in the graph's legend). The yield strength (YS), ultimate tensile strength (UTS), and elongation extracted from these curves are presented in

Table 2, together with the Young's moduli of the single materials measured by ultrasonic analysis. The tested bi-material samples are shown on the right-hand side in Figure 8, and the perpendicular purple lines indicate where the materials' interface was in the bi-material specimens. In these images, the Invar half of the specimens is in the top, above the yellow line, and the Inconel 718 half is at the bottom.

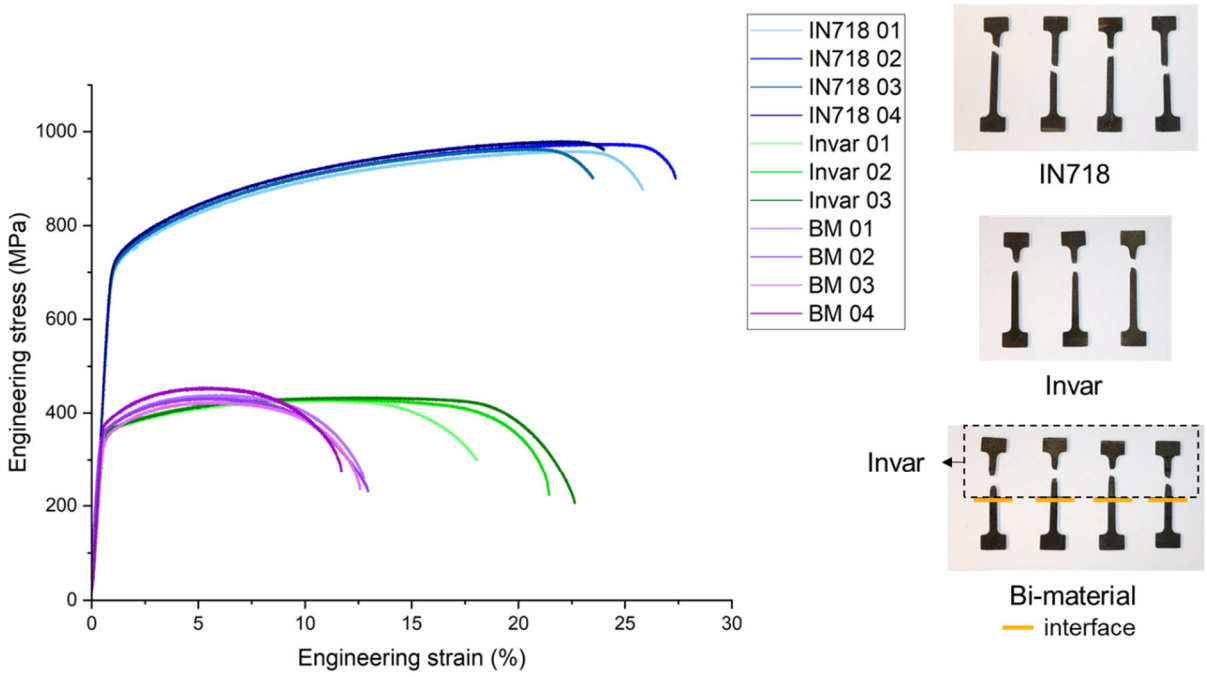


Figure 8 – Engineering stress-strain curves of the as-printed specimens: Inconel 718 in blue, Invar in green, and bi-material in purple. The fractured specimens are shown on the right-hand side, with the material's interface indicated by the yellow lines.

Table 2 – Mechanical properties of the as-printed materials.

	E (GPa)	**YS (MPa)**	**UTS (MPa)**	**Elongation (%)**
Invar	140 ± 3	361 ± 3	432 ± 3	20 ± 2
IN718	204 ± 4	715 ± 4	971 ± 10	25 ± 1
Bi-material	-	366 ± 14	439 ± 13	12 ± 1

3.4. Thermal fatigue tests

Due to their notch geometry and the CTE mismatch between the constituent materials, the hinges of the triangle unit cells are regions of stress concentration. Nevertheless, none of the printed samples failed during the tests performed in this work. The hinges of the thermally cycled unit cells were observed under an optical microscope, and no cracks or plastic deformation were seen. Plastic deformation is also unlikely to have happened during the dilatometer cycles, since the displacement curves of the unit cells in the cooling and heating cycles were reproducible (see Figure D.1 in the Appendix) and the size of the samples remained the same.

4. Discussion

The results of this work indicate that the CTE of the metamaterial can be reliably predicted by the FEM simulations, and that the metamaterial printed via bi-metallic PBF-LB presents an acceptable structural integrity for space applications. These arguments will be further discussed in the next subsections, including the possibility of applying the metamaterial as a dimensional stabilizer for potential space applications.

4.1. Predictability of the metamaterial's CTE

Single unit cells behave differently from a metamaterial, since there are no other unit cells around them. In the unit cells studied in this work, this lack of neighboring unit cells led to a bulge on the top and bottom surfaces of the unit cells, observed in the simulations and DIC analysis in Figure C.1 and C.2. This causes a reduction in the CTE of the negative-CTE structures and an increase in the CTE of the positive-CTE structures, as observed in Figure 5b. In the same plot, the addition of unit cells in one direction, i.e., from a single unit cell to a 2x1 matrix and then to a 4x1 matrix, made the measured CTE approach the simulated CTE. Similar conclusions have already been made in our previous study [39], in which the behavior of single unit cells could be predicted by simulation, and the addition of more unit cells to the structure approached the simulated CTE of a metamaterial. However, a structure that presented a good match with the simulated metamaterial CTE, i.e., when periodic boundary conditions are applied, had not yet been observed until this current study.

The measured CTE of the 10x5 matrix (Figure 7), which had several unit cells in both directions, showed a good match with the simulated CTE. This has proven that the FEM simulations can reliably predict the behavior of the bi-metallic metamaterial studied in this work. This will help not only to understand the measured displacements of the satellite experiment but also assist in developing a control algorithm to adjust the temperature of the heating elements glued onto the metamaterial to achieve a specific CTE [41,42].

Another interesting approach suggested in this study to achieve a targeted CTE is to combine unit cells with different angles and material assignments, which has presented not only a good match with the simulated CTE, but also a more stable CTE along the measured temperature range, in comparison with only positive- or only negative-CTE unit cells (Figure 6). Moreover, the combination of positive- and negative-CTE unit cells allows CTEs ranging between Invar and Inconel 718 (dashed lines in Figure 5a) to be tuned.

Finally, the addition of the trapezoid geometry for the active heating does not seem to have influenced the CTE of the unit cells significantly. In comparison with the other studied geometries for active heating in [41], the trapezoid has the least effect on the negative thermal expansion behavior of the metamaterial. In this study, the measured curves overlap each other for the positive-CTE unit cell and are very similar for the negative-CTE unit cell. In practice, during the satellite experiment, the actuator would be heated by radiation heat transfer of the solar rays as well as conduction heat transfer by the activation of the heating element glued on top of the trapezoid geometry [42]. These conditions are not the same as those imposed by the dilatometer or the heating plate, in which the temperature was homogeneous throughout the entire structure. Further analyses will be required to observe the expansion behavior of the actuator when the heat is provided by the heating elements only. Despite that contrast in the heating conditions, the NTE behavior of the metamaterial at different temperatures is now well

understood, supporting the simulation of the entire satellite experiment and future CTE measurement results made in orbit.

4.2. Structural integrity of the metamaterial

The mechanical properties of the single material specimens in this study presented a good agreement with the values found in the literature for both as-printed Invar and Inconel 718, presented in Table 3. The Young's moduli of these metals are compatible with values found in their specifications, meaning that the elastic behavior is not significantly affected by their manufacturing method [45,46]. The mechanical properties of the as-printed Inconel 718 are similar to those found in the literature by Hosseini and Popovich [47] and show a lower elongation than the specimens from Schneider et al. [48]. On the other hand, as-printed Invar presented similar values of YS and UTS to the works of Wei et al. [49] and Yakout et al. [50], but a considerably lower elongation, which, according to them, was expected to be over 40% for dense parts. However, in the review work of Huang et al. [51], it was shown that a wide range of elongation values have been found for Invar fabricated via PBF-LB in the literature, including values similar to, but still slightly higher than the ones found in this work. Part of this wide range of results may be explained by the anisotropy of Invar evidenced by Qiu et al. [52], in which specimens taken perpendicular to the build direction and the columnar grains (which is the case of this work) present a lower elongation and a more brittle fracture than the specimens parallel to the build direction.

The bi-material specimens showed similar YS and UTS values to Invar, which was the material that failed during the tensile tests. If the initial length of the specimen used to calculate the engineering strain is divided by half, which is the initial Invar length in the specimen, the elongation would be doubled, i.e., 24%, which is again close to the single-material elongation, although it is slightly larger. The recalculated stress-strain curves of the bi-material specimens considering only half of the specimen's gauge length are plotted in Figure E.1 in the Appendix. No plastic deformation is expected in the Inconel 718 part, since its YS is higher than the bi-material specimens' UTS, but the interface between the materials, which has been measured in a previous study to be as large as 1 mm [40], could have been plastically deformed and contributed to this larger elongation.

Table 3 – Mechanical properties of as-printed Inconel 718 and Invar found in the literature.

	Inconel 718		**Invar**	
	This study	**Literature**	**This study**	**Literature**
E (GPa)	204 ± 4	208[46]	140 ± 3	140[45]
YS (MPa)	715 ± 4	670[47] 700[48]	361 ± 3	393[49] 316 - 353[50]
UTS (MPa)	971 ± 10	1010[47] 995[48]	432 ± 3	470[49] 408 - 425[50] 427 – 539[51]
Elongation (%)	25 ± 1	21[47] 33[48]	20 ± 2	46[49] 10 – 62[50] 25 – 47[51]

Due to the novelty of the bi-metallic PBF-LB process and the unknown mechanical behavior of the parts manufactured by it, mechanical tests are crucial to guarantee that the structure is qualified for a satellite experiment. The interface between the two materials is a region of concern, as previous studies in dissimilar material printing have shown that brittle intermetallic phases or even cracks might be created when the materials are mixed [33,38]. The presence of these would be detrimental to the mechanical integrity of the actuator and could lead to failure during the satellite experiment. The material combination used in this work was specifically selected due to the metallurgical compatibility between these materials and the low probability of creating intermetallic phases.

Besides the fact that no cracks were found at the interface between Inconel 718 and Invar in our previous study [40], the mechanical tensile tests performed in this current work have shown that the interface is not the weakest point of the bi-metallic part. Similar results were found by Wen et al. [53], who performed tensile tests in bi-metallic Inconel 718 + 316L stainless steel specimens. In their work, the failure happened at the 316L side, meaning that the bond between the materials has a good structural integrity.

In our work, the failure of the tensile test specimens happened at the Invar side, which is weaker than Inconel 718. This means that, as long as the stresses do not exceed Invar's YS, no plastic deformation should occur in the actuator, and that the material mixture at the interface should not present a risk for its structural integrity.

Concerning thermal fatigue of the metamaterial, although the hinge of the unit cells is a stress concentration region, due to its geometry and the CTE mismatch between the constituent materials, no cracks or apparent plastic deformation were observed in this region after cycling them 500 times, even in detailed inspection in an SEM at high magnification. Additionally, the displacement curves measured in the dilatometer heating and cooling cycles were reproducible, which indicates that plastic deformation is unlikely to have happened.

In addition to CTE values, FEM simulations also contain information about the stress state of the metamaterial. Stresses are generally low, in the elastic regime of both materials, except at very localized regions close to their interface, in the hinge region. Due to singularity effects and CTE mismatch, peak stresses above the YS of both materials were observed in the FEM simulations. However, the notch of the transition area between the two materials was represented in the model using simple assumptions, e.g. sharp interface between each material, when in fact, there is an interface zone where the materials are mixed due to the PBF-LB process that can be as broad as 1 mm, which could attenuate the CTE mismatch or even strengthen the Invar portion that would be subjected to high stress loads. Therefore, the local stresses at the hinge region predicted by the FEM simulations were not considered realistic in this study. Consequently, employing a more sophisticated modeling approach would enhance the precision of the local stress analysis. Furthermore, the overall behavior of the unit cells demonstrated strong agreement with experimental validation, reinforcing the reliability of the global simulation results.

4.3. Metamaterials to compensate for thermal expansion

This work suggests a possible path to achieving dimensional stability by compensating for the expansion of conventional materials with engineered metamaterials. In Figure 9, the measured CTE of an aluminum alloy, which is a material often used for space applications, is plotted

together with the simulated CTE of the metamaterial. As the DIC of the 10x5 matrix has shown good correlation with the simulation results, these can be used to predict the actuator behavior. The CTE values of aluminum and the metamaterial are similar in magnitude but have opposite signs. However, as observed in the results of the combined positive-CTE and negative-CTE unit cell (Figure 6), an opposite CTE sign is not enough to guarantee a zero-CTE of the overall structure, since it will only dictate the length change of a structure based on its initial length. Therefore, the experiment design (cf. Figure 12 in [42]) considers this aspect.

Compared with metamaterials with only positive- or negative-CTE unit cells, the combination of positive-CTE and negative-CTE unit cells resulted in a more stable CTE curve, evidenced by the shallower curvature of its fitted quadratic function (cf. Table 1). Moreover, the CTE of $+4.8 \times 10^{-6}$/K achieved by the unit cell combination studied in this work lies in a range of CTEs that would not be achievable with only negative- or only positive-CTE unit cells, i.e., between the CTEs of Invar and Inconel 718 (cf. Figure 5). This approach allows the CTE of future metamaterials to be tuned to any specific desired value from -20×10^{-6}/K to $+31 \times 10^{-6}$/K, which are the peak CTE values considering, respectively, a negative-CTE and a positive-CTE unit cell with a θ angle of 20°.

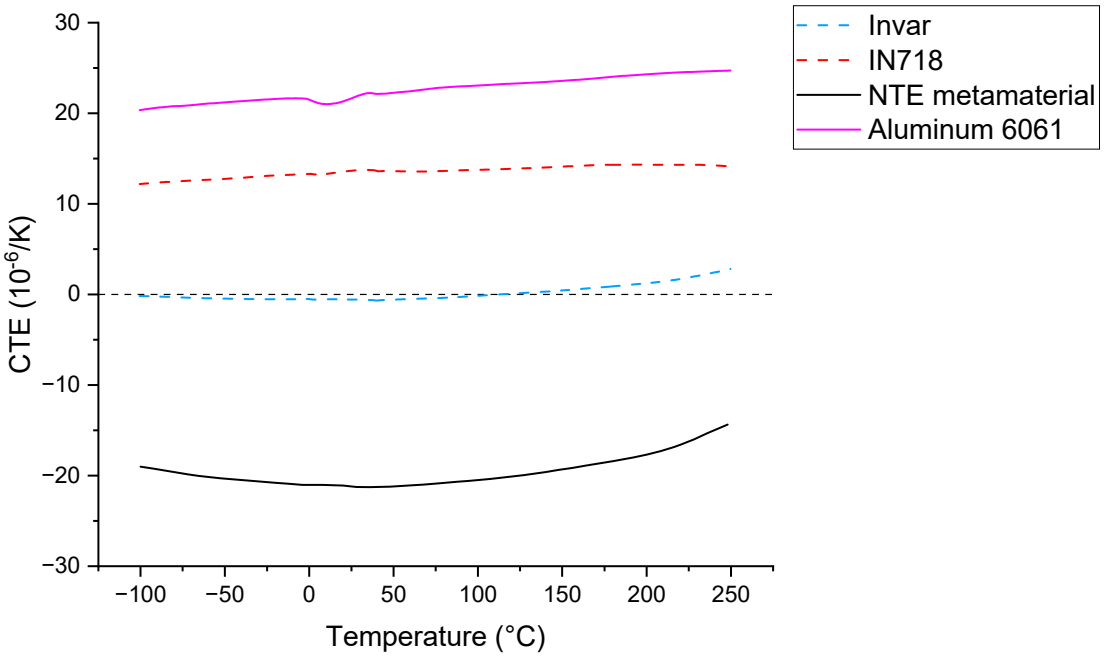


Figure 9 – Comparison of the CTE curves of the NTE metamaterial made of Invar and Inconel 718 printed for the satellite experiment and a conventionally manufactured aluminum block.

In Figure 9, the aluminum alloy 6061 and Inconel 718 exhibit relatively linear and stable CTEs, whereas Invar presents an increase in its CTE above 200°C – likely corresponding to the Curie temperature of the as-printed Invar in this study. This behavior is expected, as the low CTE of Invar is explained by a ferromagnetic phenomenon, which is no longer effective above the Curie temperature [51]. For this reason, the metamaterial in this work also presents an increase in the CTE at temperatures above 200°C. The combination of unit cells has helped to achieve

a more stable CTE (cf. Figure 6), with a less steep increase above 200°C, which would be beneficial for future applications concerning thermal expansion compensation that operate within this temperature range. Nonetheless, for the intended application in a satellite experiment, with an expected operating temperature ranging between -120°C and +150°C, the CTE curve of the metamaterial is sufficiently stable.

Finally, the thermal expansion compensation is possible in only one direction with the metamaterial geometries presented in this work. However, this research enables the understanding of the NTE behavior of these metamaterials and constitutes a proof of concept for their application in a satellite experiment. In the future, more complex metamaterials that present an NTE in two directions can be considered. Isotropic NTE metamaterials, i.e., with an NTE in three directions, are not printable by metallic PBF-LB machines within the current state of the art.

5. Conclusions

In this study, a bi-metallic metamaterial fabricated via a novel manufacturing process is proposed as a solution to achieve dimensional accuracy in space applications. By presenting a negative thermal expansion behavior, the metamaterial compensates for the thermal expansion of neighboring components when subjected to temperature variations and, thus, leads to an overall zero-CTE.

The metamaterial was investigated not only concerning its thermal expansion behavior, but also in terms of structural integrity for space applications. For the structural integrity check, tensile tests on specimens and thermal fatigue tests on the printed metamaterials were conducted. For a thorough understanding of the metamaterial thermal expansion behavior, single unit cells and multi-unit cells matrices were investigated by FEM simulations, dilatometry, and DIC. The proposed metamaterial is intended to be applied in a satellite experiment, with both active and passive dimensional stabilization. For the active stabilization, an extra trapezoid geometry was added to the base of the triangular unit cell to allow the attachment of heating elements. The influence of this geometry on the metamaterial's CTE was also considered in this work.

The following key conclusions are taken from this work:

- A negative CTE – as low as -20×10^{-6}/K – or a highly positive one – up to $+31 \times 10^{-6}$/K – can be achieved by switching the material assignment within the triangular geometry. However, simply changing the triangle's angle does not allow for tuning the CTE within the range defined by the parent materials' intrinsic CTEs. To address this limitation, a combination of unit cells with opposite CTE signs has shown strong agreement with simulation results and enables tuning the effective CTE beyond the range achievable by a single type of unit cell. Additionally, this approach leads to a more stable CTE across the tested temperature range, which may be advantageous for applications requiring thermal expansion compensation in materials with similarly stable CTEs.
- The addition of the trapezoid geometry on top of the triangle's base had little to no effect on the metamaterial's CTE, meaning that the behavior of the metamaterial printed for the satellite experiment should have a similar behavior to the structures simulated without the trapezoids.

- The FEM simulations with periodic boundary conditions can reliably predict the thermal expansion behavior of the printed metamaterial. Therefore, any metamaterial can be designed and simulated before printing to achieve a desired CTE. Moreover, the knowledge of the expansion and contraction of the metamaterial at each temperature is crucial to: (1) understand the displacements that will be measured in the satellite experiment and (2) develop a control algorithm to adjust the temperature of the heating elements glued onto the metamaterial to achieve a specific displacement.
- The metamaterial did not fail the thermal fatigue tests, which simulated the temperature span during orbit. Moreover, the tensile tests indicate that a sound interface is achieved with the bi-metallic PBF-LB process, because the failure of the specimens occurred instead in the weakest material (Invar). Therefore, the interface does not pose a risk for an in-orbit failure.

Although the metamaterial presented in this current work allows compensation for the thermal expansion in only one direction, as the NTE is observed only perpendicular to the triangle's base (cf. Figure 1), it is an initial step for developing geometrically more complex metamaterials that could present an isotropic NTE. The structural integrity tests and thermal expansion measurements have demonstrated the potential applicability of these metamaterials in the space industry.

Acknowledgements

This research as part of project SeRANIS is funded by dtec.bw – Digitalization and Technology Research Center of the Bundeswehr which we gratefully acknowledge. dtec.bw is funded by the European Union – NextGenerationEU. The authors would like to acknowledge the Institute of Mechanics of the University of the Bundeswehr Munich for the use of the furnace used for the thermal fatigue tests in this study.

CRediT authorship contribution statement

Isabel Beatriz Prestes: Conceptualization, Data curation, Formal analysis, Investigation, Methodology, Validation, Visualization, Writing – original draft; **Johannes Rottler**: Methodology, Validation, Writing – review & editing; **Eric Aimé Jägle**: Conceptualization, Methodology, Funding acquisition, Supervision, Writing – review & editing.

Declaration of competing interest

The authors declare that they have no known competing financial interests or personal relationships that could have appeared to influence the work reported in this paper.

APPENDIX A – Dilatometer CTE curves after smoothing filter

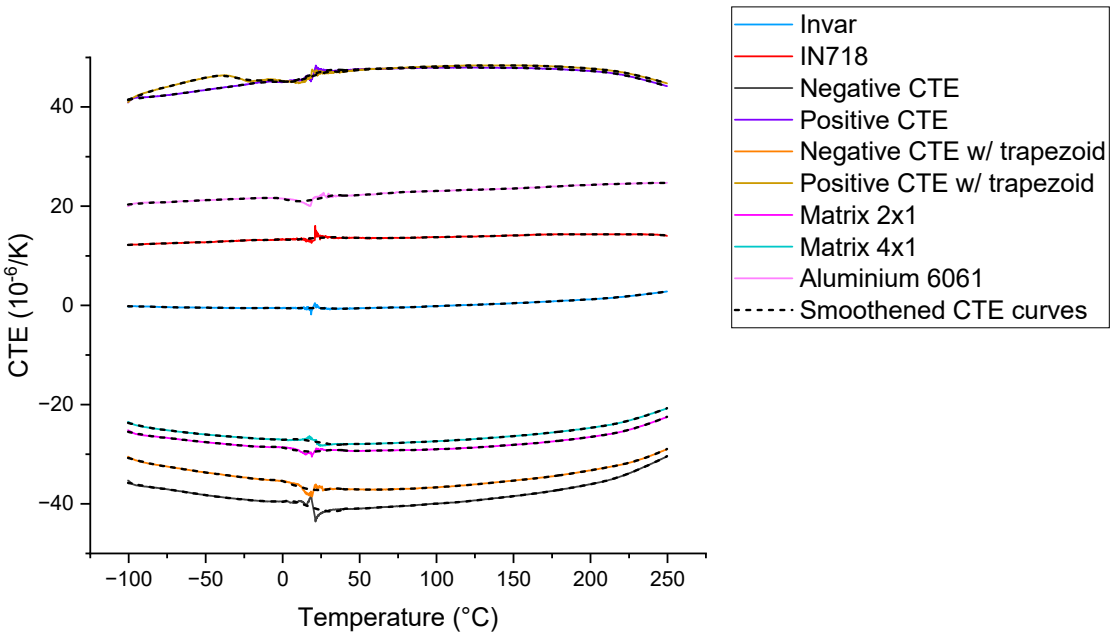


Figure A.1 – Comparison of the raw CTE curves obtained from the dilatometer and the smoothened CTE curves by a Savitzky-Golay smoothing filter – dashed lines. The smoothing filter consists of a moving average of 200 points of measurement.

APPENDIX B – Quadratic function fits

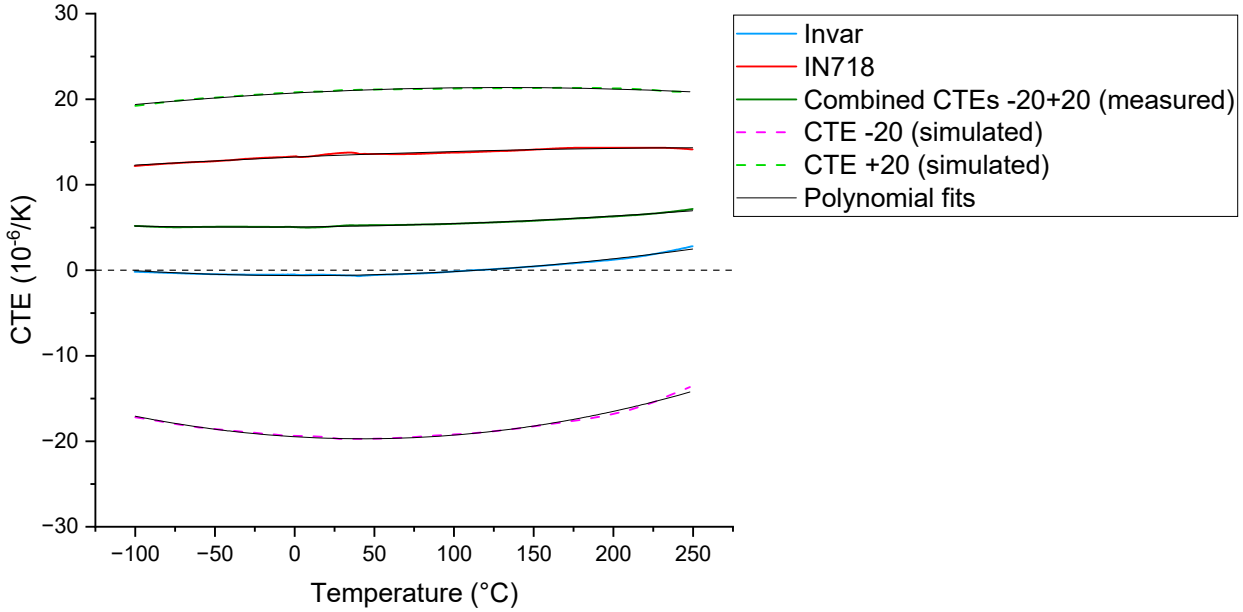


Figure B.1 – Quadratic function fits (solid black lines) on the CTE curves presented in Figure 6.

APPENDIX C – Single unit cell bulging effect

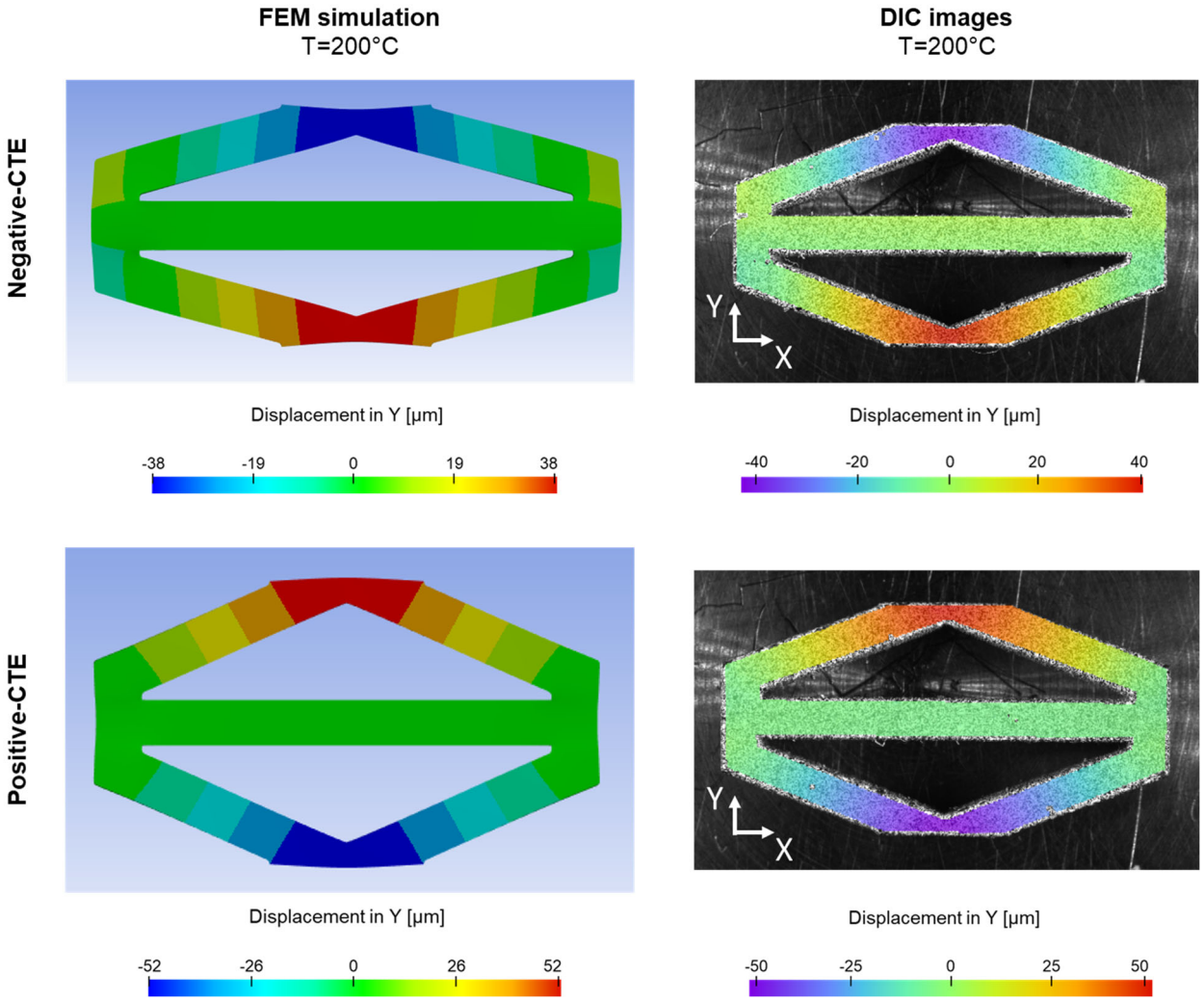


Figure C.1 – Comparison of the simulation (left-hand side) of the bulging movement of single unit cells – i.e. without periodic boundary conditions – with the DIC images (right-hand side) at 200°C: the negative-CTE condition leads to an inward bulging of the top and bottom surfaces, whereas the positive-CTE condition leads to an outward bulging. The results of the DIC are comparable with the simulated displacement in Y-direction.

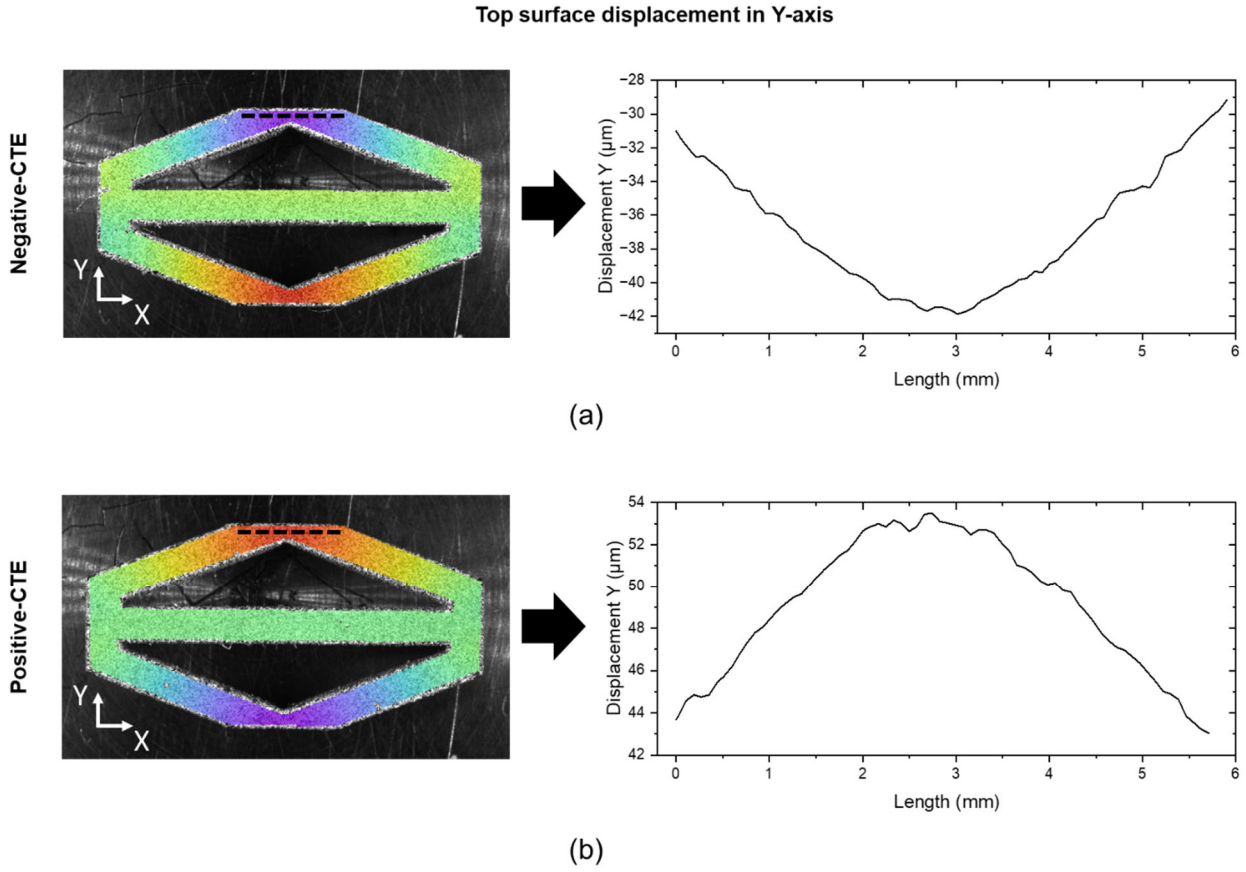


Figure C.2 – Top surface displacement of the (a) negative- and (b) positive-CTE unit cells at 200°C measured by means of DIC, capturing the bulging effect predicted by the simulations when there are no neighboring unit cells around them.

APPENDIX D – Displacement curves in heating and cooling cycles of the dilatometer

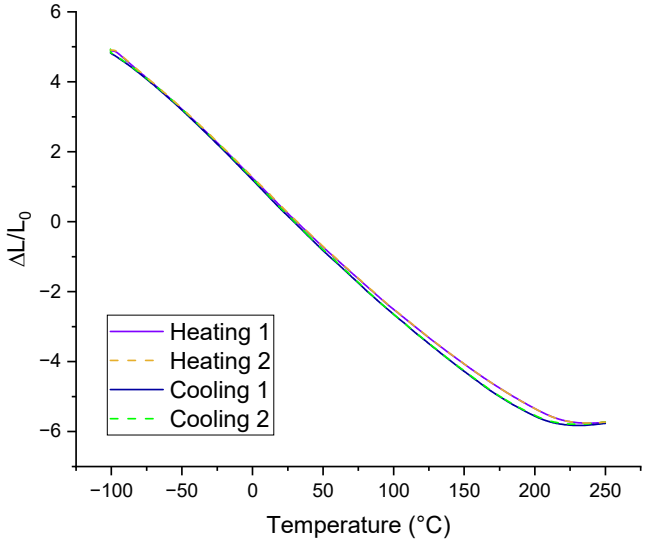


Figure D.1 - Displacement curves of a single unit cell with negative CTE during the heating and cooling cycles of the dilatometer. The curves of heating cycles overlap, as well as the curves of the cooling cycles, meaning that a plastic deformation is unlikely to have happened.

APPENDIX E - Stress-strain curve of bi-material specimens calculated with half of the gauge length

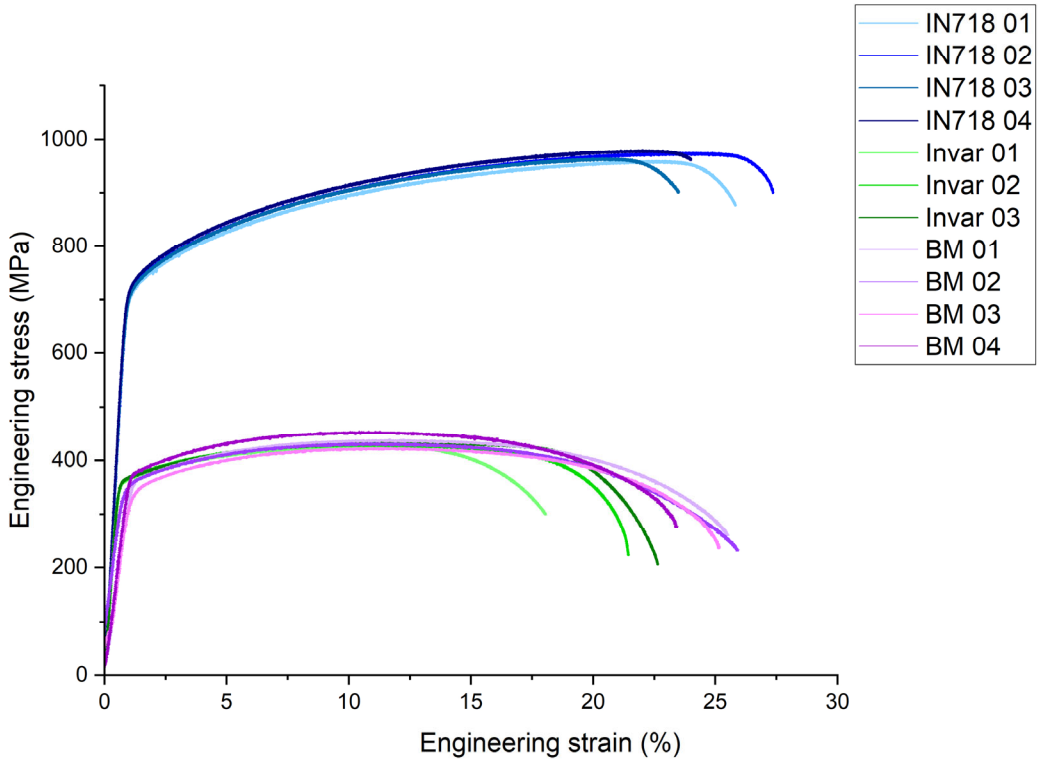


Figure E.1 – Recalculated stress-strain curve of the bi-material specimens considering only half of the gauge length (i.e. Invar's length). The curves become more similar to the pure Invar's stress-strain curves.

References

[1] R. Edeson, G.S. Aglietti, A. Tatnall, Conventional stable structures for space optics: The state of the art, Acta Astronautica 66 (2010) 13–32. https://doi.org/10.1016/j.actaastro.2009.06.015.

[2] N. Pottish, Designing for dimensional stability in space, 2005. https://www.compositesworld.com/articles/designing-for-dimensional-stability-in-space (accessed May 16th, 2025).

[3] B. Yu, Z. Xu, R. Mu, A. Wang, H. Zhao, Design of Large-Scale Space Lattice Structure with Near-Zero Thermal Expansion Metamaterials, Aerospace 10 (2023) 294. https://doi.org/10.3390/aerospace10030294.

[4] V. Villalba, H. Kuiper, E. Gill, Review on thermal and mechanical challenges in the development of deployable space optics, J. Astron. Telesc. Instrum. Syst. 6 (2020) 1. https://doi.org/10.1117/1.JATIS.6.1.010902.

[5] X. Tang, D. Chen, L. Xin, Z. Sun, Z. Zhao, Z. Yan, X. Tian, X. Li, A DIC method for thermal micro-deformation measurement of satellite high stability composite structure in simulated

space environment, Optics and Lasers in Engineering 169 (2023) 107722. https://doi.org/10.1016/j.optlaseng.2023.107722.
[6] Q. Zhang, Y. Sun, Novel metamaterial structures with negative thermal expansion and tunable mechanical properties, International Journal of Mechanical Sciences 261 (2024) 108692. https://doi.org/10.1016/j.ijmecsci.2023.108692.
[7] X. Li, L. Gao, W. Zhou, Y. Wang, Y. Lu, Novel 2D metamaterials with negative Poisson's ratio and negative thermal expansion, Extreme Mechanics Letters 30 (2019) 100498. https://doi.org/10.1016/j.eml.2019.100498.
[8] E. Gdoutos, A.A. Shapiro, C. Daraio, Thin and Thermally Stable Periodic Metastructures, Exp Mech 53 (2013) 1735–1742. https://doi.org/10.1007/s11340-013-9748-z.
[9] K. Wei, Y. Peng, K. Wang, S. Duan, X. Yang, W. Wen, Three dimensional lightweight lattice structures with large positive, zero and negative thermal expansion, Composite Structures 188 (2018) 287–296. https://doi.org/10.1016/j.compstruct.2018.01.030.
[10] Jill M. Holz, Cengiz Kunt, Chris Lashley, Douglas B. McGuffey (Ed.), Development of a lightweight near-zero CTE optical bench for the Wide-Field Camera 3 instrument, 2003.
[11] R. Lakes, 2007. Cellular solids with tunable positive or negative thermal expansion of unbounded magnitude. Applied Physics Letters 90, 221905. https://doi.org/10.1063/1.2743951.
[12] O. Sigmund, S. Torquato, Composites with extremal thermal expansion coefficients, Applied Physics Letters 69 (1996) 3203–3205. https://doi.org/10.1063/1.117961.
[13] K. Wei, H. Chen, Y. Pei, D. Fang, Planar lattices with tailorable coefficient of thermal expansion and high stiffness based on dual-material triangle unit, Journal of the Mechanics and Physics of Solids 86 (2016) 173–191. https://doi.org/10.1016/j.jmps.2015.10.004.
[14] R. Lakes, Cellular solid structures with unbounded thermal expansion, J Mater Sci Lett (Journal of Materials Science Letters) 15 (1996) 475–477. https://doi.org/10.1007/BF00275406.
[15] J. Qu, M. Kadic, A. Naber, M. Wegener, Micro-Structured Two-Component 3D Metamaterials with Negative Thermal-Expansion Coefficient from Positive Constituents, Sci. Rep. 7 (2017) 40643. https://doi.org/10.1038/srep40643.
[16] L. Wu, B. Li, J. Zhou, Isotropic Negative Thermal Expansion Metamaterials, ACS Appl. Mater. Interfaces 8 (2016) 17721–17727. https://doi.org/10.1021/acsami.6b05717.
[17] M.-M. Chen, M.-H. Fu, L.-H. Lan, S.V. Sheshenin, A novel 3D structure with tunable Poisson's ratio and tailorable coefficient of thermal expansion based on a tri-material triangle unit, Composite Structures 253 (2020) 112803. https://doi.org/10.1016/j.compstruct.2020.112803.
[18] J.N. Grima, D. Attard, R. Gatt, Truss-type systems exhibiting negative compressibility, Physica Status Solidi (b) 245 (2008) 2405–2414. https://doi.org/10.1002/pssb.200880267.
[19] G. Jefferson, T.A. Parthasarathy, R.J. Kerans, Tailorable thermal expansion hybrid structures, International Journal of Solids and Structures 46 (2009) 2372–2387. https://doi.org/10.1016/j.ijsolstr.2009.01.023.
[20] J. Lehman, R. Lakes, Stiff, strong zero thermal expansion lattices via the Poisson effect, J. Mater. Res. 28 (2013) 2499–2508. https://doi.org/10.1557/jmr.2013.154.
[21] T.-C. Lim, Negative thermal expansion in transversely isotropic space frame trusses, Physica Status Solidi (b) 250 (2013) 2062–2069. https://doi.org/10.1002/pssb.201384234.
[22] C.A. Steeves, S.L. dos Santos e Lucato, M. He, E. Antinucci, J.W. Hutchinson, A.G. Evans, Concepts for structurally robust materials that combine low thermal expansion with high stiffness, Journal of the Mechanics and Physics of Solids 55 (2007) 1803–1822. https://doi.org/10.1016/j.jmps.2007.02.009.

[23] H. Xu, A. Farag, D. Pasini, Routes to program thermal expansion in three-dimensional lattice metamaterials built from tetrahedral building blocks, Journal of the Mechanics and Physics of Solids 117 (2018) 54–87. https://doi.org/10.1016/j.jmps.2018.04.012.
[24] L. Ai, X.-L. Gao, Three-dimensional metamaterials with a negative Poisson's ratio and a non-positive coefficient of thermal expansion, International Journal of Mechanical Sciences 135 (2018) 101–113. https://doi.org/10.1016/j.ijmecsci.2017.10.042.
[25] J.S. Raminhos, J.P. Borges, A. Velhinho, Development of polymeric anepectic meshes: auxetic metamaterials with negative thermal expansion, Smart Mater. Struct. 28 (2019) 45010. https://doi.org/10.1088/1361-665X/ab034b.
[26] Q. Wang, J.A. Jackson, Q. Ge, J.B. Hopkins, C.M. Spadaccini, N.X. Fang, Lightweight Mechanical Metamaterials with Tunable Negative Thermal Expansion, Phys. Rev. Lett. 117 (2016) 175901. https://doi.org/10.1103/PhysRevLett.117.175901.
[27] C.S. Ha, E. Hestekin, J. Li, M.E. Plesha, R.S. Lakes, Controllable thermal expansion of large magnitude in chiral negative Poisson's ratio lattices, Physica Status Solidi (b) 252 (2015) 1431–1434. https://doi.org/10.1002/pssb.201552158.
[28] X. Ren, R. Das, P. Tran, T.D. Ngo, Y.M. Xie, Auxetic metamaterials and structures: a review, Smart Mater. Struct. 27 (2018) 23001. https://doi.org/10.1088/1361-665X/aaa61c.
[29] Z. Xia, W. Zhao, Y. Wang, P. Li, M. Xiao, L. Gao, Multi-material isogeometric topology optimization for thermoelastic metamaterials, International Journal of Heat and Mass Transfer 245 (2025) 126995. https://doi.org/10.1016/j.ijheatmasstransfer.2025.126995.
[30] K. Wei, Y. Peng, W. Wen, Y. Pei, D. Fang, 2017. Tailorable Thermal Expansion of Lightweight and Robust Dual-Constituent Triangular Lattice Material. Journal of Applied Mechanics 84, 101006. https://doi.org/10.1115/1.4037589.
[31] H. Xu, D. Pasini, Structurally Efficient Three-dimensional Metamaterials with Controllable Thermal Expansion, Sci. Rep. 6 (2016) 34924. https://doi.org/10.1038/srep34924.
[32] A. Nazir, O. Gokcekaya, K. Md Masum Billah, O. Ertugrul, J. Jiang, J. Sun, S. Hussain, Multi-material additive manufacturing: A systematic review of design, properties, applications, challenges, and 3D printing of materials and cellular metamaterials, Materials & Design 226 (2023) 111661. https://doi.org/10.1016/j.matdes.2023.111661.
[33] I.H. ZainElabdeen, L. Ismail, O.F. Mohamed, K.A. Khan, A. Schiffer, Recent advancements in hybrid additive manufacturing of similar and dissimilar metals via laser powder bed fusion, Materials Science and Engineering: A 909 (2024) 146833. https://doi.org/10.1016/j.msea.2024.146833.
[34] K. Wei, X. Xiao, J. Chen, Y. Wu, M. Li, Z. Wang, Additively manufactured bi-material metamaterial to program a wide range of thermal expansion, Materials & Design 198 (2021) 109343. https://doi.org/10.1016/j.matdes.2020.109343.
[35] E.M. Parsons, Lightweight cellular metal composites with zero and tunable thermal expansion enabled by ultrasonic additive manufacturing: Modeling, manufacturing, and testing, Composite Structures 223 (2019) 110656. https://doi.org/10.1016/j.compstruct.2019.02.031.
[36] Y. Ding, M. Akbari, X.-L. Gao, L. Ai, R. Kovacevic, Use of a Robotized Laser Powder-Feed Metal Additive Manufacturing System for Fabricating Metallic Metamaterials, in: T.S. Srivatsan, T.S. Sudarshan, K. Manigandan (Eds.), Manufacturing Techniques for Materials, CRC Press, 2018, pp. 51–65.
[37] M. Bambach, M.R. Tucker, Laser powder bed fusion of planar bi-metallic thermally auxetic lattice structures, CIRP Annals 73 (2024) 141–144. https://doi.org/10.1016/j.cirp.2024.04.023.
[38] O. Červinek, M.R. Tucker, D. Koutný, M. Bambach, 2024. Computational and experimental investigation of thermally auxetic multi-metal lattice structures produced by laser powder bed fusion. Virtual and Physical Prototyping 19, e2396069. https://doi.org/10.1080/17452759.2024.2396069.

[39] I.B. Prestes, E. Buchmann, P. Höfer, E.A. Jägle, Prediction of the negative thermal expansion behavior of metallic metamaterials printed via bi-material laser-based powder bed fusion, Materials & Design 256 (2025) 114276. https://doi.org/10.1016/j.matdes.2025.114276.
[40] I.B. Prestes, E.A. Jägle, Influence of the laser strategy on bi-metallic interfaces printed via multi-material laser-based powder bed fusion, Additive Manufacturing Letters 13 (2025) 100274. https://doi.org/10.1016/j.addlet.2025.100274.
[41] E. Buchmann, I. Prestes, B. Musil, P. Höfer, Design and Investigation of a Thermoelastic Actuator with Tailored Unidirectional Thermal Expansion and Stiffness using Mechanical Metamaterials and Joule Heating Activation, in: J. Rieser, F. Endress, A. Horoschenkoff, P. Höfer, T. Dickhut, M. Zimmermann (Eds.), Proceedings of the Munich Symposium on Lightweight Design 2022, Springer International Publishing, Cham, 2023, pp. 1–14.
[42] E. Buchmann, I.B. Prestes, E.A. Jägle, P. Höfer, Athermalization of space instruments with mechanical metamaterials: structural instrument architectures and conceptual design of an in-orbit demonstration experiment, CEAS Space J (2025). https://doi.org/10.1007/s12567-025-00631-w.
[43] A. Kinzel, J. Bachmann, Jaiswal, Rishi,R., Karnal, M., Novo, E., Porcelli, F., Schmidt, A., Schwarz, R., Hofmann, C., Forstner, R Knopp, A. (Eds.), Seamless Radio Access Network for Internet of Space (SeRANIS): New Space Mission for Research, Development, and In-Orbit Demons, 2022.
[44] P. Langer, K. Sepahvand, C. Guist, J. Bär, A. Peplow, S. Marburg, Matching experimental and three dimensional numerical models for structural vibration problems with uncertainties, Journal of Sound and Vibration 417 (2018) 294–305. https://doi.org/10.1016/j.jsv.2017.11.042.
[45] SPACEMATDB - Space Materials Database, Product data of Inconel 718. https://www.spacematdb.com/spacemat/datasearch.php?name=Inconel%20718 (accessed May 22nd 2025).
[46] SPACEMATDB - Space Materials Database, Product data of Invar 36. https://www.spacematdb.com/spacemat/datasearch.php?name=Invar%2036 (accessed May 22nd 2025).
[47] E. Hosseini, V.A. Popovich, A review of mechanical properties of additively manufactured Inconel 718, Additive Manufacturing 30 (2019) 100877. https://doi.org/10.1016/j.addma.2019.100877.
[48] J. Schneider, B. Lund, M. Fullen, Effect of heat treatment variations on the mechanical properties of Inconel 718 selective laser melted specimens, Additive Manufacturing 21 (2018) 248–254. https://doi.org/10.1016/j.addma.2018.03.005.
[49] K. Wei, Q. Yang, B. Ling, X. Yang, H. Xie, Z. Qu, D. Fang, Mechanical properties of Invar 36 alloy additively manufactured by selective laser melting, Materials Science and Engineering: A 772 (2020) 138799. https://doi.org/10.1016/j.msea.2019.138799.
[50] M. Yakout, M.A. Elbestawi, S.C. Veldhuis, Density and mechanical properties in selective laser melting of Invar 36 and stainless steel 316L, Journal of Materials Processing Technology 266 (2019) 397–420. https://doi.org/10.1016/j.jmatprotec.2018.11.006.
[51] G. Huang, G. He, X. Gong, Y. He, Y. Liu, K. Huang, Additive manufacturing of Invar 36 alloy, Journal of Materials Research and Technology 30 (2024) 1241–1268. https://doi.org/10.1016/j.jmrt.2024.02.221.
[52] C. Qiu, N.J. Adkins, M.M. Attallah, Selective laser melting of Invar 36: Microstructure and properties, Acta Materialia 103 (2016) 382–395. https://doi.org/10.1016/j.actamat.2015.10.020.
[53] Y. Wen, Y. Gao, R.L. Narayan, W. Cai, P. Wang, X. Wei, B. Zhang, U. Ramamurty, X. Qu, Tensile behavior of additively manufactured Inconel 718 and stainless steel 316L with

compositionally graded joints, International Journal of Plasticity 189 (2025) 104342. https://doi.org/10.1016/j.ijplas.2025.104342.